



Max-Planck Institut für Kolloid und Grenzflächenforschung



**Functional Nanostructured Hydrothermal Carbons for  
Sustainable Technologies:  
Heteroatom Doping and Superheated Vapor**

**Dissertation**

zur Erlangung des akademischen Grades

"doctor rerum naturalium"

(Dr. rer. nat.)

in der Wissenschaftsdisziplin "Kolloidchemie"

eingereicht an der

**Mathematisch-Naturwissenschaftlichen Fakultät  
der Universität Potsdam**

von

**Stephanie-Angelika Wohlgemuth**

Geboren am 05.08.1986 in Jeddah, Saudi-Arabien

Potsdam, den 14. März 2012

Published online at the  
Institutional Repository of the University of Potsdam:  
URL <http://opus.kobv.de/ubp/volltexte/2012/6012/>  
URN <urn:nbn:de:kobv:517-opus-60120>  
<http://nbn-resolving.de/urn:nbn:de:kobv:517-opus-60120>

**Dedicated to my parents**

**„We are all faced with a series of great opportunities  
brilliantly disguised as unsolvable problems.“**

John W. Gardner

# Declaration/Eidesstattliche Erklärung

---

“I herewith declare to have written this dissertation independently. All parts of this thesis which are cited literally or in a rough summary from publications or other secondary material are recognizable, and I have clearly defined them with their respective references.”

„Hiermit erkläre ich des Eides statt, dass ich vorliegende Dissertation selbstständig verfasst und keine anderen als die angegebenen Quellen und Hilfsmittel benutzt habe und alle Ausführungen, die anderen Schriften wörtlich oder sinngemäß entnommen wurden, kenntlich gemacht sind.“

Stephanie-Angelika Wohlgemuth

Potsdam, 14.03.2012



# Acknowledgments

---

First of all, I would like to thank **Prof. Dr. Markus Antonietti** for giving me the opportunity to carry out the work for this thesis under his supervision at the MPIKG. His valuable input, support, guidance and especially his never ending enthusiasm throughout the process has made it a truly unforgettable experience. I thank **Dr. Maria-Magdalena Titirici** for her supervision and integration into the wonderful world of HTC. Doing science and running marathons with you was great! **Dr. John Texter, Dr. Shu-Hong Yu and Prof. Dr. Arne Thomas** are thanked for agreeing to act as examiners for this thesis. I thank **Dr. Klaus Tauer, Dr. Robin J. White, Dr. Filipe Vilela, Dr. Marek Grzelczak and Kathleen Krüger** for their collaboration and time taken for scientific (and in fact sometimes also very non-scientific) discussions, as well as for their professional and personal support and encouragement. My deepest gratitude goes to **Dr. Hiromitsu Urakami**, who has given me confidence, honest criticism, and support wherever possible. Thank you for being my colleague, friend, and teacher. **Dr. Tim Fellingner and Nina Fechler**, it was and is an honor to share the office, the lab and numerous interesting discussions about work and life with you. I thank **Regina Rothe** for taking such good care of our group, and **Dr. Michael Bojdys** for always taking good care of me. Many things would not have been possible without the expertise and never-ending will to help of **Stefan Glatzel** and his constant efforts to bring comedy into our lives. Thanks to **Philipp Jäker** for doing his internship with me and a big thank you to all those past and present colleagues who have contributed to such a warm and entertaining working environment, Camillo, Betty, Nico, Jelena, Linghui, Giani, Irene, Jerome, Li, Kai, Lina, Antje, Katja, Miriam, Davide, Tristan, Debora, Josh, Pablo, and many more. Sylvia Pirok, Heike Runge, Rona Pitschke, Jürgen Hartmann, Sören Selve (TU Berlin), Carmen Serra (University of Vigo), Nikki Baccile (Universite Pierre et Marie-Curie), Marc Willinger (FHI) are acknowledged for their assistance with measurements. Diana Enge and Marco Ehlert are thanked for their IT services. I thank my family and friends for their emotional support – you have made the fun times memorable and the rough times bearable! **Mama and Papa and Koko**, thank you for everything and I hope I have made you proud. **An meine Oma:** Vielen Dank dafür, dass du immer stolz auf mich bist, egal was ich tue. Finally, to **Stephan Stenglin**, for your love and support I will be forever grateful. I look forward to our next adventure together.

# Table of Contents

---

<i>Declaration/Eidesstattliche Erklärung</i> -----	<i>i</i>
<i>Acknowledgments</i> -----	<i>iii</i>
<i>Table of Contents</i> -----	<i>iv</i>
<i>1 Introduction Science, Climate, Energy, and Carbon</i> -----	<i>1</i>
<i>2 Fundamentals</i> -----	<i>6</i>
2.1 Hydrothermal Carbonization (HTC)-----	<i>6</i>
2.2 The oxygen reduction reaction and electrochemical characterization -----	<i>18</i>
<i>3 Chemical modifications I Heteroatom doped carbon microspheres with tunable sulfur binding states</i> -----	<i>23</i>
3.1 Introduction -----	<i>23</i>
3.2 Mechanistic considerations -----	<i>25</i>
3.3 Sulfur and nitrogen dual doped carbon microspheres-----	<i>26</i>
3.4 Sulfur doped carbon microspheres-----	<i>37</i>
3.5 Implications of the heteroatom binding state-----	<i>39</i>
3.6 Summary of chapter 3 -----	<i>40</i>
<i>4 Chemical modifications II Templated nano-architectures - Heteroatom doped carbon hollow spheres</i> -----	<i>41</i>
4.1 Introduction -----	<i>41</i>
4.2 Heteroatom doped carbon hollow spheres -----	<i>43</i>
4.3 Summary of chapter 4 -----	<i>51</i>
<i>5 Chemical Modifications III Template-free nano-architectures - Heteroatom doped organic and carbon aerogels</i> -----	<i>52</i>
5.1 Introduction -----	<i>52</i>
5.2 Sulfur and nitrogen doped organic/carbon aerogels <i>via</i> the albumin-directed HTC of glucose -----	<i>54</i>



5.3	Heteroatom doped organic/carbon aerogels <i>via</i> the borax-mediated HTC of glucose -----	70
5.4	Summary of the “chemical modification” chapters -----	85
6	<i>High temperature hydrothermal carbonization I Carbon microspheres from different carbohydrates</i> -----	86
6.1	Introduction-----	86
6.2	Experimental considerations -----	88
6.3	Carbon microspheres derived <i>via ht</i> HTC of xylose, glucose and starch -----	90
6.4	Summary of chapter 6 -----	95
7	<i>High temperature hydrothermal carbonization II A one pot synthesis of carbon hollow spheres</i> -----	97
7.1	Introduction-----	97
7.2	Experimental considerations -----	98
7.3	A one pot <i>ht</i> HTC synthesis of carbon hollow spheres -----	99
7.4	Summary of chapter 7 -----	101
8	<i>Summary, Conclusions, Outlook</i> -----	102
9	<i>Appendix</i> -----	107
9.1	Experimental Methods-----	107
9.2	Supplementary information -----	114
9.3	List of abbreviations -----	124
10	<i>References</i> -----	126



# 1 Introduction

## Science, Climate, Energy, and Carbon

---

**Science.** With the current change in public consensus of western countries concerning more sustainable lifestyles and economic efficiency, scientists who carry out fundamental research often find themselves faced with criticism. Expectations are increasing to justify the funding of research that cannot guarantee, nor has the specific intention to lead in a linear way to technological innovations or economic growth. As a consequence, much of fundamental science research has been increasingly use-inspired, *i.e.* with the choice of problems and the conduct of research often inspired by societal needs.<sup>1</sup> It has been argued that science in the 21<sup>st</sup> century has the highest chances for success, both in terms of public acceptance and financial support, if the synergistic potential between basic science institutions and science based industry can be activated.<sup>2</sup> The underlying topic of this thesis is **hydrothermal carbonization** (HTC). HTC is not a new concept, but was first introduced by Bergius in 1913 who described the transformation of cellulose into coal-like materials.<sup>3</sup> However, while the Bergius process was based on the liquefaction of coal for the production of biofuels, the focus has recently shifted towards carbonization of biomass for the production of functional carbonaceous materials.<sup>4,7</sup> HTC is a fascinating field of research, with much about it known but far more to be discovered. In simple terms, it is a mimic of natural coalification on a timescale of hours rather than millions of years.<sup>4,6,8</sup> The deconvolution of the complex reaction mechanism, and as a result the ability to control the reaction to engineer functional carbon materials with specific properties, is a topic of great academic, but also industrial interest. The term “functional carbon” inherently implies some sort of function, *i.e.* applicability of the material. Scientific curiosity aside, HTC does indeed carry great potential for future greener technologies, especially in the context of climate change mitigation.<sup>6</sup>

**Climate.** Since the industrial revolution over 200 years ago, mankind has depended on fossil fuels. Not only are they at the heart of energy generation, but they are also the feedstock for the petrochemical industry. Until recently, oil has been cheap and hence the pressure to innovate has been minimal. Fossil fuels are non-renewable because they require millions of years to form and are depleted at a much faster rate than they can be replenished. This unbalance in the carbon

cycle causes large amounts of carbon in the form of greenhouse gases (GHG) such as CO<sub>2</sub> and methane to accumulate in the earth's atmosphere. While “*global warming*” caused by anthropogenic emissions may be controversially discussed, one cannot argue against the fact that humanity cannot carry on relying on fossil resources indefinitely.<sup>9</sup> On one hand, they are limited resources and alternatives need to be found to supply entire industries that currently rely on fossil fuels in order to maintain our way of life. On the other hand, climate change and the associated risks are becoming more urgent issues that need to be addressed.<sup>10-12</sup>

**Energy.** According to the 4<sup>th</sup> assessment report by the intergovernmental panel on climate change (ipcc), the largest contribution of anthropogenic CO<sub>2</sub> emissions comes from fossil fuels.<sup>13</sup> The energy supply contributed 25.9 % to the total anthropogenic GHG emissions in 2004, which was even higher than the contributions from industry (19.4 %). With the current global energy system being dominated by fossil fuels, energy is therefore one of the major issues that need to be addressed. The increasing population and simultaneous social and economic development implies that the demand for energy and associated products cannot be expected to come to a halt in the future, but will become an increasingly large problem. Simply “using less energy” is therefore an unrealistic option to mitigate climate change, and one of the great challenges of the 21<sup>st</sup> century will be the development of non-fossil fuel alternatives.<sup>9,14</sup>

**Carbon.** Carbon, in the form of CO<sub>2</sub>-releasing fossil fuels, is therefore one of the main “culprits” in the context of climate change. Terms such as “*carbon footprint*”, “*carbon cycle*” and “*greenhouse effect*” have been coined and are generally associated with negative aspects of carbon. However, carbon-based materials in fact have immense potential when it comes to finding alternative, greener technologies in the present and future. Their wide availability as well as diversity of physicochemical properties, such as chemical and thermal stability, electrical conductivity, and the ability to adopt a wide range of morphologies makes them attractive candidates for high end applications. Non-fossil-fuel carbon feedstocks such as biomass present promising renewable energy sources and building blocks for more advanced applications than simple heat and energy generation *via* combustion. Carbon-based materials find use in almost all aspects of life, ranging from basic applications such as water purification<sup>15</sup> and fertilizers<sup>16</sup> through to sorption,<sup>17, 18</sup> pigments,<sup>19</sup> chromatography,<sup>20-22</sup> energy storage and conversion,<sup>23, 24</sup> as well as catalysis.<sup>25-27</sup>

For the engineering of nanostructured materials for high end applications, some of the most important factors concerning material properties are:

- **Conductivity** (*e.g.* electronic applications)
- **Surface functionality** (*e.g.* adsorption, acid/base catalysis)
- **Chemical inertness** (*e.g.* supports)
- **Surface area** (almost all applications)

Pure carbon materials can fulfill these criteria to a certain extent, but to broaden the range of possible applications, heteroatom modification (*i.e.* “doping”) is a useful tool to tune material properties. The introduction of, *e.g.* sulfur or nitrogen into a carbon material can result in improved electrical conductivity, material stability and catalytic performance due to an increased number of active sites.<sup>28-31</sup> Remarkable progress has been made in recent years regarding the use of such carbon-based materials, and it can be expected that this trend will continue in the future.<sup>32-34</sup> Current synthetic procedures for carbon materials most commonly involve high temperature heat treatment under inert conditions (pyrolysis),<sup>35, 36</sup> chemical vapor deposition<sup>34, 37</sup> or arc discharge techniques.<sup>38, 39</sup> Besides being very energy consuming, these techniques also often require the use of harmful precursors which are in turn produced from fossil fuels. It is therefore a point of great interest to not only focus on the sustainability of the final application (*e.g.* electric vehicles, hydrogen fuel cells, solar cells, *etc.*) but equally on the sustainability of the entire process, *i.e.* from choosing the precursor, the synthesis conditions through to the final application. In 1998, the **12 principles of green chemistry** were formulated by Anastas *et al.*<sup>40</sup>

1. **Prevention** (of waste)
2. **Atom Economy** (maximize the incorporation of all materials used)
3. **Less Hazardous Chemical Syntheses**
4. **Designing Safer Chemicals**
5. **Safer Solvents and Auxiliaries**
6. **Design for Energy Efficiency**
7. **Use of Renewable Feedstocks** (ideally biowaste)
8. **Reduce Derivatives** (*e.g.* blocking groups, protection/ deprotection)
9. **Catalysis** (as opposed to use of stoichiometric reagents)
10. **Design for Degradation**
11. **Real-time analysis for Pollution Prevention**
12. **Inherently Safer Chemistry for Accident Prevention**

Returning to the concept of HTC, it is clear that this technique can offer the basis for technologies which conform in many ways to the 12 principles of green chemistry. The advantages of HTC are the possibility of using cheap, readily available starting materials in a simple, low cost synthesis which requires only water as solvent.<sup>5, 41</sup> Importantly, it allows for the removal of carbon from the carbon cycle because biomass (which sequesters CO<sub>2</sub> *via* photosynthesis, but would simply be decomposed by microorganism to release CO<sub>2</sub>) can be used as precursor in the formation of useful carbon materials. HTC is therefore a so-called “CO<sub>2</sub>-negative” technique with highly efficient atom economy.<sup>6</sup> A crucial point here is that the notion of using fast growing crops which compete with food production (either directly or indirectly by the occupation of useful farming lands) is not sustainable – instead, the use of biological feedstocks should be based on biowaste which would simultaneously help with disposal issues.

So how realistic is it that HTC will play a big part not only in the academic, but also the industrial world? HTC derived materials have already shown good potential in applications such as heavy-metal absorption, catalysis, anode materials and conductive coating of metals.<sup>42, 43</sup> Nitrogen doping has been achieved by various routes to further improve material performance for some of these applications.<sup>44-46</sup> While the HTC derived materials may not yet be competitive with other carbon based materials such as carbon nanotubes, graphene or fullerenes, it is to be emphasized that HTC is scalable due to the simple one pot reaction and readily available precursors – something which highly purified CNT or graphene-based materials have yet to achieve. Also, the abundance of heteroatoms in natural molecules such as amino acids and proteins allows for the synthesis of doped carbon materials in one step directly from biowaste, *e.g.* HTC of prawn shells.<sup>44</sup> In terms of scaling up, first prototypes of HTC plants have been built, though the current focus lies in the production of, *e.g.* charcoal, rather than materials for high end electronic applications. The most promising aspect and future challenge of HTC is the possibility of using waste biomass for the large scale synthesis of useful carbon-based materials in applications that are relevant to all aspects of life.

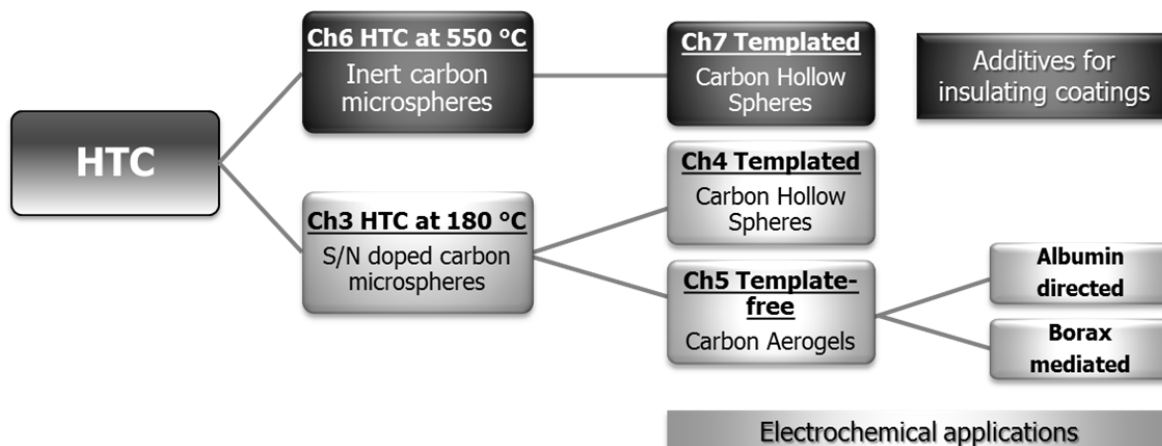


**Fig. 1.1 Schematic overview of this thesis**

The aims of this thesis are to extend the current knowledge of HTC to allow for the controlled synthesis of a “palette” of functional carbon-based materials that can be tailored for use in various applications. Two main strategies are used:

- 1) A **“chemical approach”**, whereby the HTC mechanism is exploited to allow for the incorporation of heteroatoms into the material. Complementing nitrogen, sulfur is introduced for the first time as a dopant for hydrothermal carbon. In addition to gaining valuable insights into the possible manipulations of the HTC mechanism, these materials present high potential candidates for electronic applications.
- 2) A **“physical approach”**, whereby HTC is carried out at elevated temperatures (550 °C as opposed to *ca.* 200 °C). The drastically different reaction conditions give rise to an entirely different class of hydrothermal carbon, which consequently are considered for different applications, such as filler materials.

For both approaches, the basic concept will first be shown *via* the synthesis of carbon microspheres, before moving on to more sophisticated nano-architectures (hollow spheres and aerogels). Preliminary testing of the nano-architected materials for various applications (electrocatalysts in the oxygen reduction reaction and additives for insulating coatings) will be presented to exemplify their potential. A schematic overview is shown in **Fig. 1.1**. Prior to presentation and discussion of results in chapters 3 to 7, chapter 2 will cover some fundamental background topics. HTC is introduced in more detail with focus on mechanistic theories and a brief introduction to the oxygen reduction reaction in the context of fuel cells is given.

# 2 Fundamentals

---

## 2.1 Hydrothermal Carbonization (HTC)

### 2.1.1 Introduction

The concept of hydrothermal carbonization (**HTC**) was initially introduced by Friedrich Bergius in 1913.<sup>3</sup> He described the hydrothermal transformation of cellulose into coal like materials and developed the Bergius process in which coal is liquefied to yield biofuels. He was awarded the Nobel Prize in chemistry in 1931 together with Carl Bosch, in recognition of their contributions to the invention and development of chemical high-pressure methods. Nowadays the focus of HTC has shifted somewhat from the production of biofuels to the carbonization of biomass to yield functional carbonaceous and carbon materials.<sup>6, 47, 48</sup> The term carbonaceous is used here to describe a material with high carbon content (*ca.* 60 wt %) but additionally contains other elements, usually hydrogen and oxygen, whereas the term carbon is used to describe materials that consist mainly of carbon (> 90 wt %).

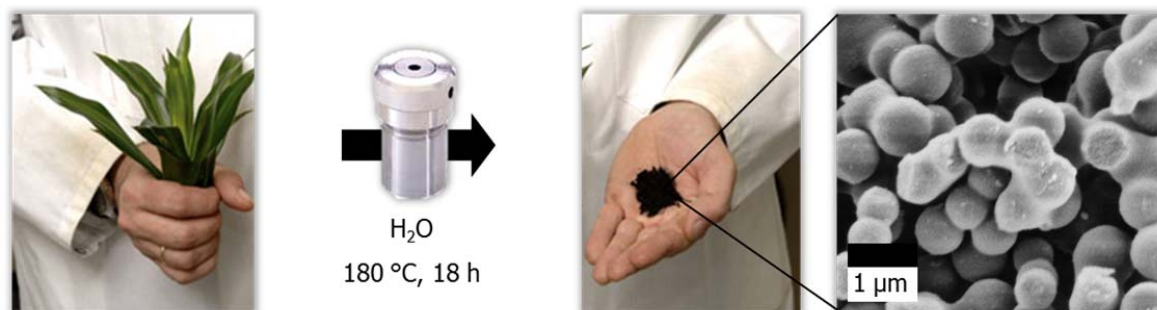


**Fig. 2.1** A schematic representation of the HTC process of biomass.

In simple terms, HTC is a mimic of natural coalification on a timescale of hours and days, rather than millions of years. The process has the advantage of being very simple to carry out and also being rather insensitive to small deviations in concentration, temperature or reaction time. A carbon precursor is placed in a sealed container, the so-called autoclave, using water as an environmentally benign solvent. This also eliminates the need for energy-consuming drying of the precursor which is a great disadvantage for processes such as pyrolysis of biomass. The autoclave can then be heated to the desired temperature (above 100 °C, generally



180 °C-200 °C) where pressure due to evaporation of liquid water is built up. This pressure is self-generated and not externally applied. From a thermodynamic point of view, HTC is an exothermic process and once enough energy has been applied to initiate the process, the reaction may in principle proceed autogenously.<sup>41</sup> After *ca.* 16 – 18 h of reaction time the HTC process yields a carbonaceous solid which upon electron microscopic analysis is found to comprise nano- to micrometer sized spherical particles (**Fig. 2.1**).

The majority of reports use glucose as a model precursor for biomass, since it is the most abundant biomass derived sugar. Glucose will also be employed throughout this thesis. HTC of crude biomass has been less studied due to the higher complexity of the system. Some reports include HTC of prawn shells,<sup>44</sup> rice grains,<sup>49</sup> oak leaves and orange peels.<sup>50</sup> Interestingly, Titirici *et al.* were able to show that the final product morphology and composition of hexoses is not substantially different from that of polysaccharides (starch, amylopectin) which gives the study of model compounds a broader validity concerning crude biomass.<sup>51</sup>

## 2.1.2 The HTC mechanism of pure carbohydrate precursors

In one of the first reports on hydrothermal carbon obtained from glucose, Sun *et al.* proposed a mechanism comprising the polymerization of glucose followed by further carbonization to yield solid spheres with a carbonized core and a hydrophilic surface.<sup>53</sup> Later, the efforts of Antonietti, Titirici and Baccile *et al.* brought further insight into the HTC mechanism.<sup>51, 52, 54, 55</sup> They were able to show that the hydrothermal treatment of glucose essentially involves three main steps:

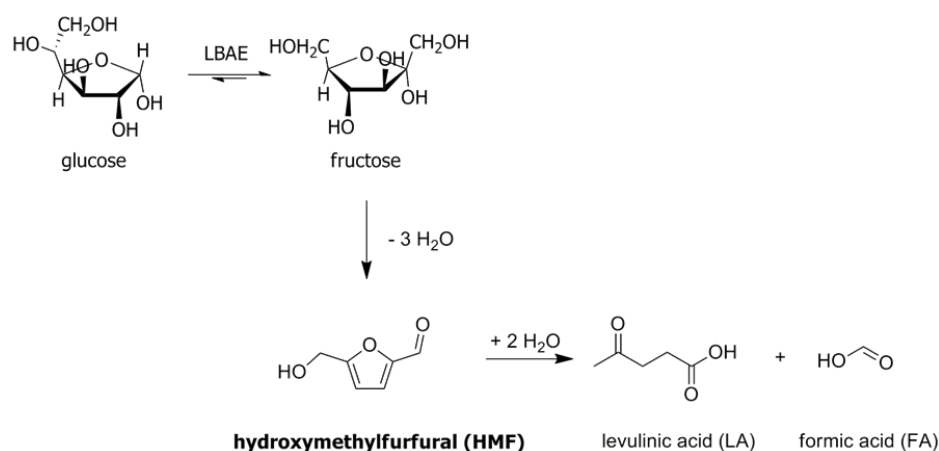


**Fig. 2.2** schematic of the isomerization of glucose to fructose and subsequent dehydration to HMF/ formation of LA and FA. Adopted from reference <sup>52</sup>

dehydration, polymerization and finally carbonization/aromatization. More specifically, the so-called Lobry de Bruyn – Alberda van Ekenstein transformation (**LBAE**) initially results in the isomerization of glucose to fructose. Under hydrothermal conditions, the equilibrium lies on the side of fructose.<sup>56, 57</sup> Subsequently fructose is dehydrated to hydroxymethylfurfural (**HMF**) which is regarded as the main reactive intermediate in HTC (**Fig. 2.2**). Other products such as organic acids and aldehydes (levulinic acid, formic acid, glyceraldehyde, *etc.*) and phenols may also be formed (*e.g. via* retro aldol reactions). They presumably feed into the HTC process by being physisorbed onto or incorporated into the carbon framework *via* aldol reactions, but also by lowering the overall pH which in turn enhances the autocatalytic effect during HTC.<sup>8, 58</sup> For simplicity, the reactivity of HMF will be discussed as a representative of hydrothermal carbon forming intermediates. HMF is a highly reactive intermediate and may be involved in a variety of possible reactions taking place at the HMF ring substituents or the ring itself. A detailed discussion of furan chemistry and HMF reactivity has been recently provided in the dissertation of Tim Feller from the Antonietti group and will hence only be briefly summarized here.<sup>52</sup> Instead, the focus in this thesis is placed on Maillard chemistry and chemistry allowing the incorporation of nitrogen and sulfur species into hydrothermal carbon (**chapters 3 to 4**).

### 2.1.2.1 Reactions involving the HMF furanic ring substituents

The **aldehyde** of HMF can react with  $\alpha$ -ketones or aldehydes *via* aldol addition or condensation (**Fig. 2.3 I**). Alternatively, acetalization can take place in the presence of alcohols (forming hemiacetals) or vicinal diols, *e.g.* from glucose moieties (**Fig. 2.3 II**). Acetalization results in a reversal

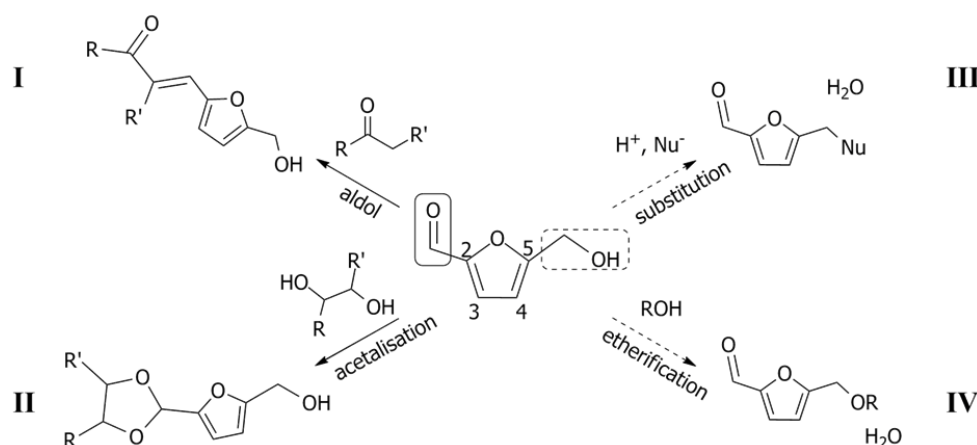


**Fig. 2.3** possible reaction pathways of substituents on the HMF furanic ring. Adopted from reference<sup>52</sup>

of the electron withdrawing effect of the aldehyde on the furan ring, *i.e.* it acts as an electron donating group (**EDG**), activating the ring for reactions such as electrophilic aromatic substitution (**EAS**).

The **hydroxyl substituent** can undergo simple nucleophilic substitution *via* an  $S_N1$  or  $S_N2$  mechanism (**Fig. 2.3 III**). HTC conditions are mildly acidic so the protonated hydroxyl should be a good leaving group. Also, if the furan ring is rendered electron rich (*via* acetalization of the aldehyde), the primary carbocation resulting from loss of the hydroxyl group can be stabilized. A special type of nucleophilic substitution is etherification where the nucleophile is an alcohol (**Fig. 2.3 IV**).

### 2.1.2.2 Reactions involving the HMF furanic ring

Furans are known to participate in electrophilic aromatic substitution (preferentially at the 2 and 5 positions), cycloaddition and electrophilic addition. The high electronegativity of oxygen decreases the aromaticity of the ring compared to benzene, thiophene or pyrrol (see later).<sup>59</sup> Generally, electron withdrawing groups (**EWG**) as substituents will deactivate the ring with respect to electrophilic aromatic substitution whereas EDGs will activate it.

In the case of HMF the aldehyde acts as EWG so EAS is unlikely, also because the preferential 2 and 5 positions on the furan ring are blocked. Instead, nucleophilic addition can occur (**Fig. 2.4 I**). The addition of water and subsequent ring opening leads to the formation of levulinic

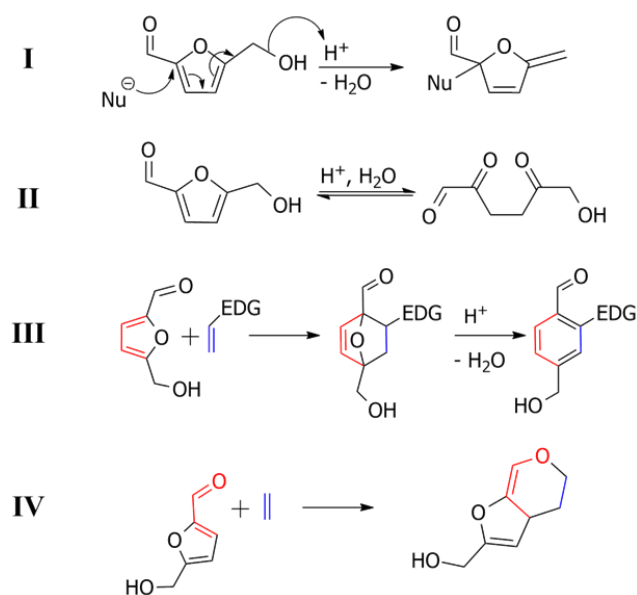
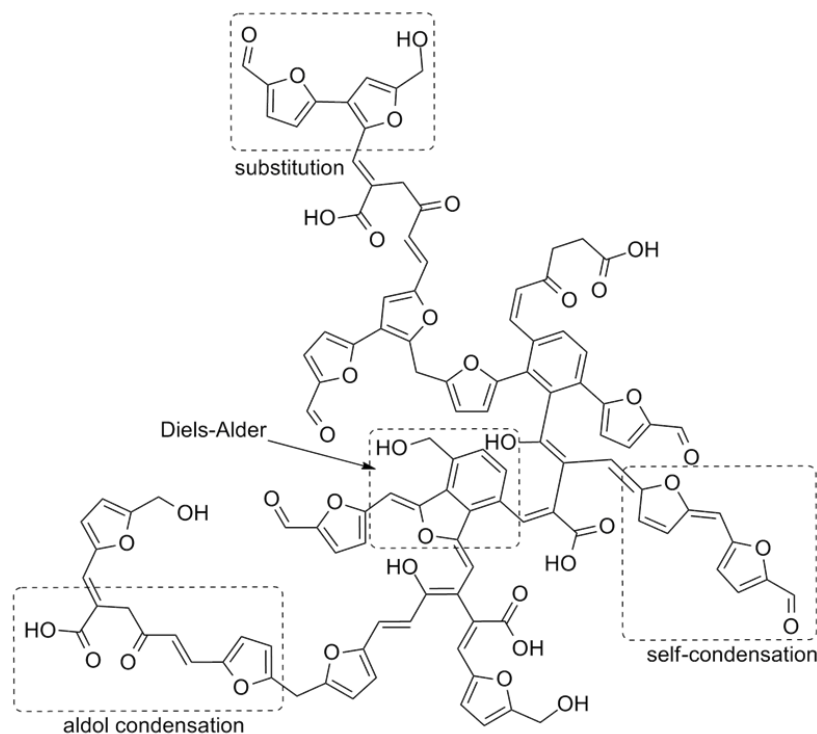


Fig. 2.4 possible reaction pathways of the HMF furanic ring. Adopted from reference <sup>52</sup>

acid and formic acid in hydrothermolysis, forming reactive diketones (**Fig. 2.4 II**). These diketones can in turn undergo aldol and other reactions. HMF can also participate in Diels Alder reactions, whereby the diene can originate completely from within the ring (**Fig. 2.4 III**) or in combination with the aldehyde substituent, provided it rotates into a *syn* configuration with the ring double bond (**Fig. 2.4 IV**).

### 2.1.2.3 A furan-based structure for hydrothermal carbon

Overall it is clear that a single definite answer to the “HTC mechanism” cannot be provided. In addition to the manifold of possible reactions that even a single precursor such as glucose can give rise to, factors such as concentration, pH, temperature and reaction time will influence the overall system. Titirici *et al.* were able to show that irrespective of the type of precursor used (hexose monosaccharides or polysaccharides), the final hydrothermal carbon exhibited similar spherical morphologies and chemical structures in terms of atom percentages and functionalities. They also showed that pentose sugars (*e.g.* xylose) exhibit slightly different chemical structures than hexoses, like higher aromaticity.<sup>51</sup> Because glucose, a hexose, is used throughout this thesis,



**Fig. 2.5** A possible structure of hydrothermal carbon as a result of dehydration, polymerization and aromatization reactions. Adopted from reference <sup>52</sup>

pentoses will not be further discussed. Solid state  $^{13}\text{C}$  nuclear magnetic resonance ( $^{13}\text{C}$  ssNMR) and Fourier-transform infrared spectroscopy (FT-IR) studies indicate that hydrothermal carbon comprises a large fraction of furanic units in addition to abundant carbonyl functionalities such as carboxylic acids and ketones. It has been pointed out that even though the range of possible reactions is diverse, it is very likely that all saccharides pass through a HMF (for hexoses) or furfural (for pentoses) forming stage prior to carbonization.<sup>51</sup> Resinification schemes as have been reported for furfural and furfuryl alcohol are also likely to play a role in hydrothermal carbon formation. Gandini *et al.* have attributed the color formation of branched furfuryl alcohol polymers to the formation of extensive conjugated domains. The proposed mechanism involves hydride abstraction at the methylene bridges of oligo(furfuryl alcohol) units, leading to conjugated linear polymer chains. They also pointed out that branching only occurs after some degree of conjugation has been reached in the linear species which then react *via* Diels Alder reactions to form branched polymers.<sup>60</sup> A possible structure for hydrothermal carbon is shown in **Fig. 2.5**.

In summary, a set of dehydration, polymerization (*i.e.* condensation and addition) as well as aromatization reactions are responsible for hydrothermal carbon formation. Which reactions are dominant depends on the reaction conditions and precursors used and may affect yield, morphology and chemical composition of the final product. In some cases, the product morphology and composition is insensitive to the precursor used but in others, manipulation of the HTC mechanism can lead to drastically different results.

### **2.1.3 The HTC mechanism in the presence of heteroatom-containing additives**

In this thesis, doping of glucose-derived hydrothermal carbon is carried out by the addition of heteroatom containing molecules such as amino acids and proteins. The reactions between reducing sugars like glucose and amino acids/proteins are a matter of thorough investigation in food chemistry because they are a cause of non-enzymatic browning during cooking.<sup>61, 62</sup> These so-called Maillard reactions give rise to the formation of many flavor compounds and also play a major role in the incorporation of heteroatoms during HTC.<sup>44, 63-65</sup>

### 2.1.3.1 Maillard chemistry

The Maillard reaction is not one specific reaction but rather refers to a group of reactions occurring between reducing sugars and amino acids. In the process, hundreds of different (flavor) compounds can be created which can then break down to form more compounds *etc.* It is therefore impossible to provide a definite mechanistic pathway.<sup>61</sup> Here, some of the relevant steps in the Maillard reaction cascades are presented in order to demonstrate some of the ways in which heteroatoms can be incorporated into hydrothermal carbon from glucose or other reducing sugars.

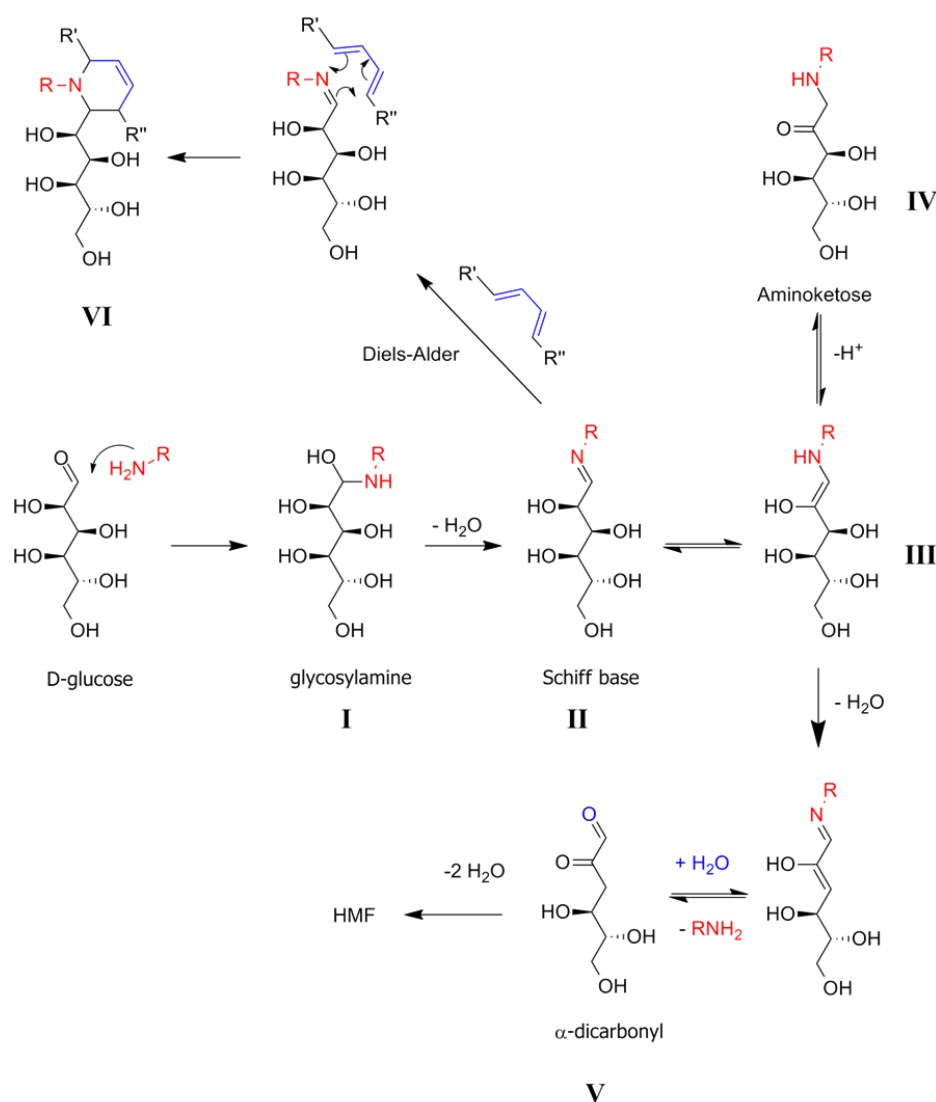
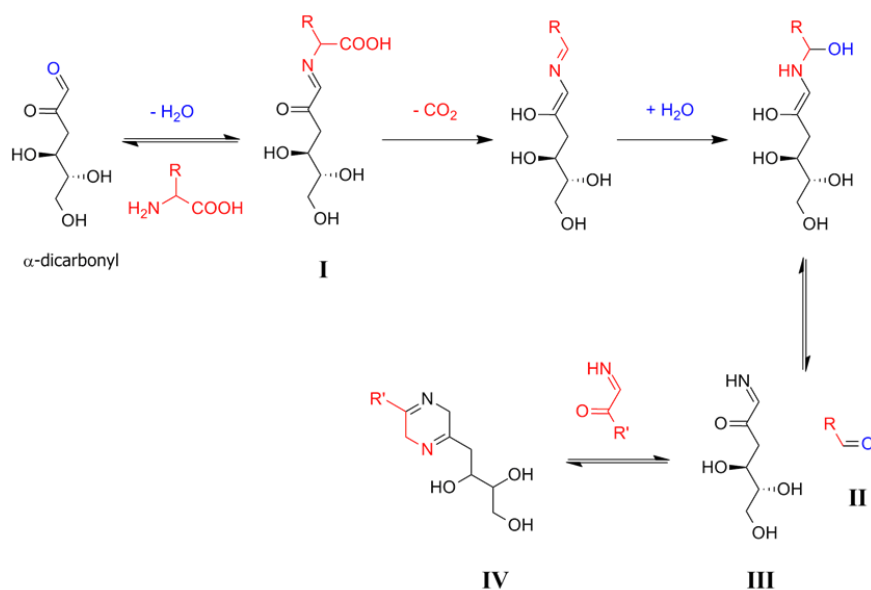


Fig. 2.6 Some examples in the Maillard reaction

The process starts with nucleophilic attack of the amine in amino acids on the aldehyde of the sugar, producing glycosylamines (**Fig. 2.6 I**) which subsequently lose a water molecule to give a Schiff base (an imine, **Fig. 2.6 II**). The  $\alpha$ -hydroxy aldehyde motif allows for the rearrangement of the Schiff bases to aminoketoses or so-called Amadori compounds (**Fig. 2.6 III and IV**).<sup>66</sup> Compound **III** can form  $\alpha$ -dicarbonyl species (**Fig. 2.6 V**) which in turn may lose two water molecules to form **HMF** but also undergo Strecker degradation (see later).<sup>67, 68</sup> Note that throughout the Maillard reactions, imino- Diels Alder reactions could occur because Schiff bases are well-known dienophiles in the formation of nitrogen-containing heterocycles (**Fig. 2.6 VI**).<sup>69</sup> Without going into further detail it should be clear that the above reactions can explain the incorporation of nitrogen which is bound aliphatically or in non-aromatic heterocycles. It has however been shown that nitrogen doped hydrothermal carbon is more aromatic than hydrothermal carbon obtained from pure glucose,<sup>46</sup> and that in addition to aliphatic nitrogen groups, aromatic heterocycles such as pyrazines, pyrroles and pyridine are present.<sup>65</sup> Baccile *et al.* used <sup>13</sup>C and <sup>15</sup>N solid state NMR studies of hydrothermal carbon obtained from glucose and glycine to show that the free amine groups in glycine are mostly converted into aromatic binding motifs. They pointed out that these aromatic structures are most likely formed as a consequence of degradation reactions.<sup>65</sup>

As mentioned before aminoketoses can be transformed into  $\alpha$ -dicarbonyls.<sup>62, 67</sup> Upon reaction with an amino acid a Schiff base is formed (**Fig. 2.7 I**). In this configuration Strecker



**Fig. 2.7** An example of the Strecker degradation

degradation may occur which results in splitting of the imine to give the so-called Strecker-aldehyde (**Fig. 2.7 II**) and an  $\alpha$ -aminoketone (**Fig. 2.7 III**).<sup>62</sup> Note that the Strecker degradation (like Maillard reactions) is more prominent in basic conditions, but can nonetheless occur under acidic conditions as is the case in HTC.<sup>70</sup>  $\alpha$ -Aminoketones can combine to give **pyrazines** (**Fig. 2.7 IV**) which have been identified to be present in nitrogen doped hydrothermal carbon.<sup>65</sup> Alternatively the  $\alpha$ -aminoketone can react with water and form ammonia which is known to react with furans, converting them to **pyrroles**.<sup>62, 66</sup> **Pyridines** can be formed *via* the cyclization of amines and carbonyls.<sup>71</sup>

Primary amines are the most important species in Maillard reactions and will take precedence over secondary or tertiary amines. In vivo, lysine is the most important amine for the Maillard reaction. Glycoproteins may only participate in the Maillard reaction after cleavage of the glycosidic bond.<sup>62</sup> Sulfur containing amino acids such as cysteine are known to have a retarding effect on Maillard reaction because the resulting decomposition products (*e.g.* H<sub>2</sub>S, sulfites) react with the aldehyde group of the reducing sugars and thereby block the access for amino groups.<sup>62</sup> If H<sub>2</sub>S is formed it can react with Maillard intermediates to give a multitude of sulfur containing products such as thiazoles.<sup>62</sup> Thiols could also react with carbonyl to form thioacetals which act as “protecting” group, preventing Maillard reactions from occurring.

### 2.1.3.2 The reactions of HMF with heteroatom containing additives

The previous sections concerned the reaction of the sugar precursor with amino acids/proteins. It was shown that HMF can be formed during these processes. However, HMF is mainly formed *via* the LBAE rearrangement and subsequent dehydration of fructose, especially because glucose is present in excess in all experiments conducted throughout this thesis. HMF can interact with amino acids/proteins and with Maillard reaction intermediates in a similar fashion as was explained in the sections concerning HMF reactivity. There are countless possible combinations of reactants and reaction cascades which of course increase with higher reactivity of the additive (*i.e.* in how many different ways can it react). For example, amines can react with the aldehyde on HMF to form imines. The difference between HMF and pure glucose here is that HMF does not contain the  $\alpha$ -hydroxyl aldehyde motif so Amadori rearrangements cannot occur. However, the imine is still a reactive dienophile and can undergo imino Diels Alder reactions to give nitrogen containing heterocycles. HMF also contains an  $\alpha,\beta$ -unsaturated aldehyde motif, allowing Michael addition to take place.<sup>72</sup> In accordance with “hard and soft



acids and bases”, or **HSAB** theory, Michael addition is more favorable for sulfur nucleophiles (“soft” due to highly polarizable orbitals) than for nitrogen nucleophiles (“hard” due to high electronegativity).<sup>72, 73</sup> In this way, thio-ethers can be formed (**Fig. 2.8 I**). Another important point for thiols is that despite their similarity to amines they cannot undergo Maillard reactions. They cannot form the thio-equivalent of Schiff bases, but instead react with aldehyde function on glucose or HMF to form a hemi-thioacetal (**Fig. 2.8 II**) which then acts as a “protecting group” on the aldehyde. Of course, amine and thiol nucleophiles can undergo nucleophilic substitution on the hydroxy function on HMF or the furanic ring, giving rise to secondary amines and thioethers, respectively.

So far, all reactions presented have assumed that the heteroatom containing additive contains free amine or thiol nucleophiles. As will be demonstrated in this thesis, thiophene and pyrrol heterocycles are also suitable additives to achieve heteroatom doping of hydrothermal carbon. This will be discussed by using two examples thiophene-carboxaldehyde (**TCA**, used in **chapters 3.4 and 5.2**) and pyrrol-carboxaldehyde (**PCA**, used in **chapter 5.3**). It helps to first compare the reactivity of furan, thiophene and pyrrol. All three rings are activated towards electrophilic aromatic substitution (EAS) compared to benzene. As for furan, the 2 and 5 positions are preferred. However, furan is the least aromatic due to the good orbital overlap with oxygen which pulls most of the electron density of the ring towards itself. The order of aromaticity, which is usually inversely correlated to the activity towards EAS, has therefore been determined to be furan < pyrrol < thiophene < benzene.<sup>59</sup> Furan in fact can also participate in nucleophilic aromatic substitution as well as add nucleophiles across the ring which disrupts aromaticity. These reactions are more difficult for the more aromatic thiophenes and pyrrols.

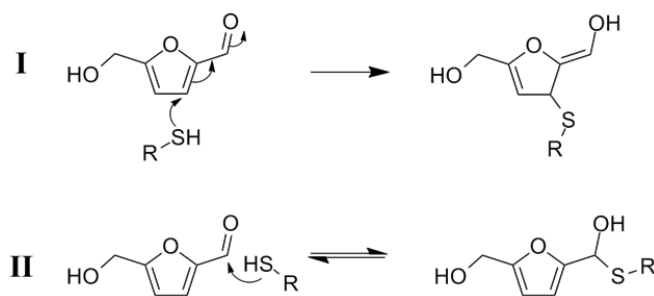


**Fig. 2.8** examples of reactions between thiols and HMF

Returning to TCA and PCA, it is clear that the aldehyde function acts as EWG and deactivates the rings towards EAS. Similarly to what has been previously mentioned for HMF, this effect can be reversed if the aldehyde is converted into, *e.g.* an acetal group (**Fig. 2.9 I**). The aldehyde can also act as a “tether” which allows attachment of the heteroatom source to a forming hydrothermal carbon framework and bring the thienyl or pyrrol ring into close proximity with potential reaction partners. It is therefore assumed that TCA and PCA most likely participate in EAS during HTC, reacting with various electrophiles that are produced during the HTC process. To verify this, various heterocyclic compounds were tested as additives in the HTC of glucose (**Fig. 2.10**). It was found that:

- If 2,5 - disubstituted thiophenes (*e.g.* 2,5-dimethyl-thiophene, **DMT** or 2,5-thiophene-dicarboxaldehyde, **TDCA**) are used as additive, the yield of sulfur incorporation is very low (< 1 wt %) in the final hydrothermal carbon. This is presumably because the preferential 2 and 5 sites for EAS are blocked. If mono-substituted 2-methylthiophene (**MTP**) is used, sulfur doping is successful because the thienyl ring is activated due to the  $\sigma$ -donating effect of the methyl group, and the 5 position is free for EAS.
- If 2-thiophene-carboxylic acid (**TCAcid**) is used, the yield of sulfur incorporation is similarly low. This is because the carboxylic acid groups deactivated the ring for EAS, but cannot be converted into an EDG like the aldehyde in TCA.

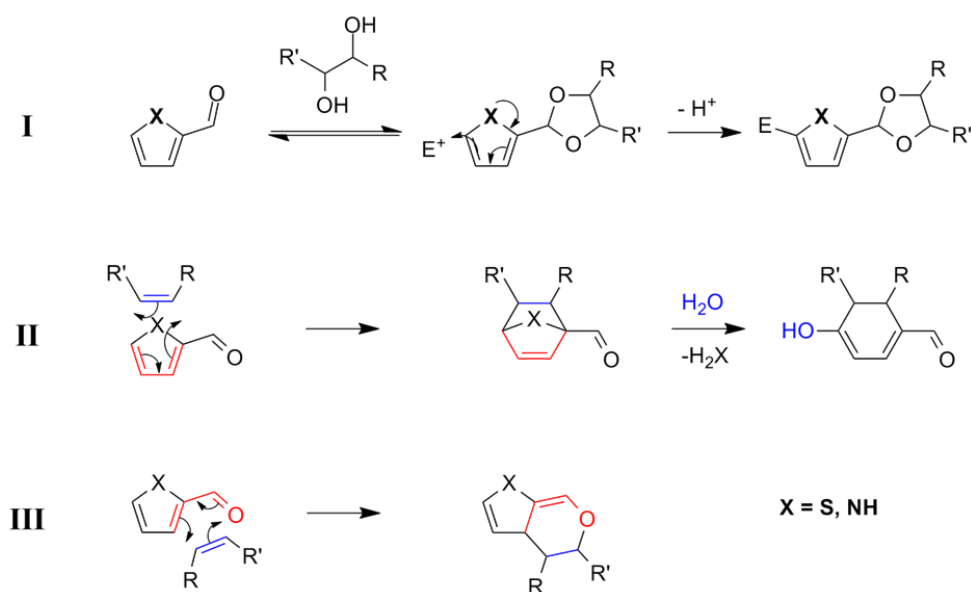


**Fig. 2.9** Possible reactions of PCA or TCA additives used as N/S sources

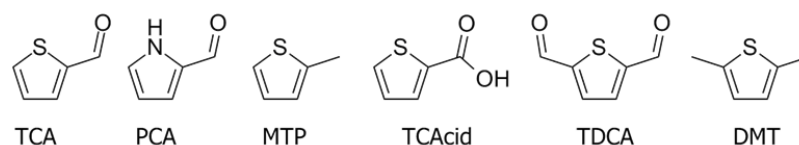


**Fig. 2.10 Structures of heterocycles used as potential heteroatom sources**

Importantly, the EAS mechanism keeps the thienyl and pyrrol rings intact and therefore allows for the incorporation of aromatically bound nitrogen or sulfur. TCA and PCA can also undergo cycloaddition. However, due to the high aromaticity of thienyl and pyrrol rings it is unlikely that the diene will originate from within the ring (as is possible for furan, refer back to **Fig. 2.4 III**). Also, in this case the heteroatom would be lost after successive eliminations (**Fig. 2.9 II**). On the other hand, if the diene is formed in combination with the aldehyde, the heteroatom is retained in the final structure (**Fig. 2.9 III**).

In summary, there are various reaction pathways that can take place when heteroatom containing molecules are added to a HTC mixture of pure glucose. The additives may react directly with the sugar but also with HTC decomposition products, of which HMF is expected to be the most abundant. For amino acids and proteins, Maillard reactions are possible with nucleophilic amines which in turn give rise to many more intermediates that can react further. The reactivity of the heteroatom source is important concerning the ways in which the heteroatoms can be incorporated into the final structure. Heterocycles can react *via* electrophilic aromatic substitution but in principle also *via* cycloaddition, whereby the heteroatom is only retained if the diene is formed in combination with a ring substituent rather than originating completely from within the ring.

## 2.2 The oxygen reduction reaction and electrochemical characterization

### 2.2.1 The Oxygen Reduction Reaction (ORR)

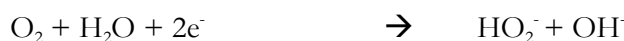
The oxygen reduction reaction is one of the most important chemical processes in life. On the most fundamental level, it is involved in biological respiration. In the context of technology, ORR plays an important role in the corrosion of metals, the production of hydrogen peroxide and it is one of the current hot topics in fuel cell research.

ORR in aqueous solutions occurs mainly by two pathways, namely *via* a two electron process, forming  $\text{H}_2\text{O}_2$  as an intermediate, or *via* a four electron process. A one electron process is also possible in aprotic or alkaline solvents. The elementary reactions involved are:<sup>74</sup>

a) Under acidic conditions:



b) Under alkaline conditions:



Fuel cells are devices that convert the chemical energy from a reaction into electrical and thermal energy. A typical polymer electrolyte membrane fuel cell (PEMFC) is shown in **Fig. 2.11**. The reactions involved are the hydrogen (the fuel) oxidation at the anode, and oxygen reduction at the cathode. The two electrodes are separated by a proton exchange membrane, which is impermeable to electrons. The electrons are therefore forced to travel *via* an external circuit, giving rise to usable electricity. Hydrogen fuel cell technology is a promising candidate for future automotive mobility. Not only is the sole combustion product environmentally benign water, but the direct conversion of chemical energy into electricity eliminates the need for heat or mechanical processes. Traditional heat engines such as steam turbines or internal combustion engines rely on a **chemical energy  $\rightarrow$  heat  $\rightarrow$  mechanical motion  $\rightarrow$  electricity** conversion

route, whereas fuel cells operate directly *via* the route **chemical energy** → **electrochemical reaction** → **electricity**.

Most fuel cell developers focus on the anode since it is involved in combustion of the fuel (hydrogen) and therefore directly involved in the cell performance. However, the ORR reaction at the cathode is of equal importance, both in terms of fuel cell performance and technology cost factor:

- The reaction kinetics are sluggish at the low temperatures which fuel cells normally operate in (80 °C to 100 °C), resulting in high overpotentials, so catalysts are required.<sup>75</sup>
- The most used catalyst is currently platinum, which is scarce (37 ppb in the earth's crust) and expensive (45 USD g<sup>-1</sup>). Pt is also used at the anode, but in much smaller amounts, so substitution at the cathode is more likely to result in a greater total decrease of Pt required for fuel cells.<sup>75</sup>
- Current fuel cells suffer from insufficient performance and durability due to catalyst oxidation, agglomeration and dissolution, loss of electrode surface area and corrosion of the carbon support.<sup>75, 76</sup>

One of the approaches to counteract these issues is the development of Pt-free electrocatalysts for the ORR. However, there is currently no commercially viable substitute for large-scale deployment.<sup>76</sup> Since Gong *et al.* reported a highly efficient, metal-free catalyst based on nitrogen doped carbon nanotubes,<sup>29</sup> the concept of using doped carbon materials has received much attention in the scientific community. So far, nitrogen has been the dominant dopant, but boron and iodine doped carbons have also been reported.<sup>77-79</sup> Very recently, sulfur doped graphenes

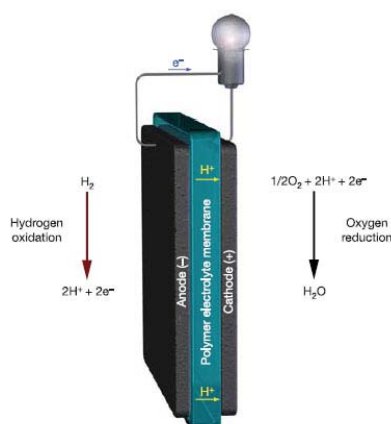


Fig. 2.11 A typical polymer electrolyte H<sub>2</sub>-O<sub>2</sub> fuel cell. Taken from<sup>75</sup>

have been shown to exhibit superior electrocatalytic properties in the ORR.<sup>80</sup> The materials in this thesis are doped either with nitrogen, sulfur or both.

## 2.2.2 Electrochemical Characterization

The most common techniques for the characterization of electrocatalysts are potential sweep techniques, including linear sweep voltammetry (LSV) and cyclic voltammetry (CV), hydrodynamic measurements using a rotating disk electrode (RDE) and chronoamperometry (CA).<sup>74</sup>

In LSV, the current at the working electrode is measured while the potential between the working electrode and the reference electrode is swept linearly in time (this is called the **scan rate**) between two set values (**Fig. 2.12a**). Oxidation or reduction reactions result in peaks or drops in the current signal. CV is basically an extension of LSV - instead of stopping the sweep at the set potential, the potential ramp is reversed, so sweeping is performed in cycles (**Fig. 2.12b**). For reversible reactions, oxidation peaks will appear when the potential is swept in one direction, and the corresponding reduction peaks appear when the sweep is reversed. For irreversible reactions, these features will only be obtained partially. Note that the currents seen in these measurements can be faradaic or capacitive, arising from redox reactions or physical phenomena such as adsorption or double layer charging. For example, supercapacitors are based on reversible double-layer charging, pseudo-capacitors benefit from fast reversible reactions occurring on the surface of the electrode. Rechargeable batteries also rely on reversible reactions whereas fuel cells gain energy from the irreversible reduction of oxygen at the cathode. It is always possible to have a mixture of processes occurring at the same time, so it is important to

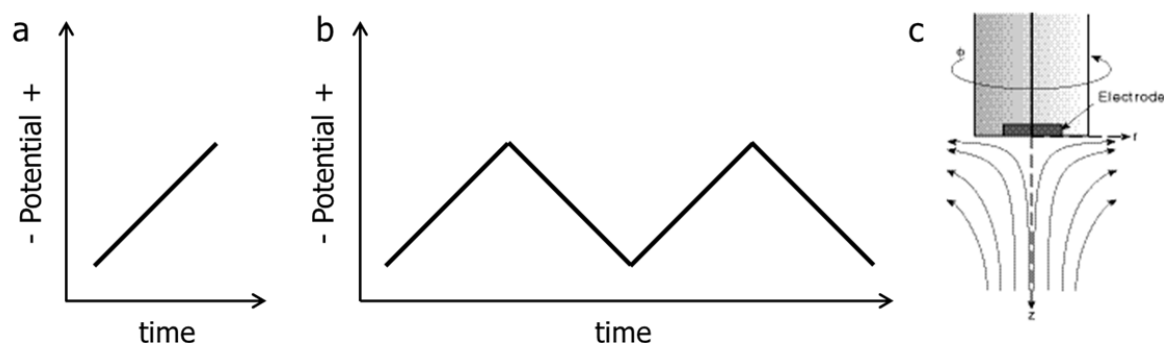


Fig. 2.12 Potential wave forms of a) linear sweep voltammetry and b) cyclic voltammetry. c) a rotating disk electrode.

distinguish between faradaic and capacitive currents to obtain trustworthy results. Since capacitive currents are independent of chemical reactions, they may be measured in an  $N_2$ -saturated solution (where no ORR can take place). The current obtained by LSV is then subtracted from the current obtained by LSV in the  $O_2$ -saturated solution to give the faradaic current value.

Mass transport of the reactant (oxygen) to a static electrode in a non-stirred solution is limited by **diffusion**. Transport can be increased by using an RDE, an electrode attached to an electric motor that has very fine control over the electrode's rotation rate. As the disk turns, some of the electrolyte solution (the **hydrodynamic boundary layer**) is dragged by the disk surface and pushed away from the electrode center by centrifugal forces. The solution is replenished by a laminar flow from the bulk, normal to the disk surface (**Fig. 2.12c**). The rate of flow can be controlled by varying the rotation angular velocity of the RDE. The steady state current is now controlled by the laminar flow of the solution, *i.e.* **convection**, in addition to **diffusion**. The diffusion term remains because there is stagnant layer at the electrode surface (that rotates with the disk) in which mass transfer is diffusion limited. The higher the rotation speed of the disk, the thinner this layer and therefore the higher the diffusion rate. Once the equilibrium at the electrode surface is driven to the product side, a steady state is reached and a **plateau current is observed**. The concentration of the reactant (oxygen) at the disc surface is then zero. By measuring LSV curves at different RDE rotation rates, various electrochemical phenomena can be investigated. One that is particularly interesting to ORR, is the number of electrons transferred, allowing the identification of a 2 electron process *versus* a 4 electron process.

Levich showed the following relationship between the diffusion controlled current, or Levich current  $I_{lev}$  and the disk rotation rate  $\omega$ :

$$I_{lev} = 0.62nFAD^{\frac{2}{3}}\omega^{\frac{1}{2}}\nu^{-\frac{1}{6}}C$$

- n number of electrons transferred in the half reaction
- F Faraday constant
- A electrode area
- D diffusion coefficient of the reactant in the electrolyte
- $\omega$  angular rotation rate of the electrode
- $\nu$  kinematic viscosity of the electrolyte
- C analyte concentration

A linear plot of  $I_{lev}$  versus  $\omega^{1/2}$  (**the Levich plot**) implies that the electrocatalytic reaction is faster than the rate of substrate delivery to the electrode, so the current is limited only by mass transport to the catalyst surface.

For a reaction mediated by an electrode surface bound cofactor (*i.e.* the catalyst), a kinetic term must be taken into account. The kinetic current,  $I_k$  is given by:

$$I_k = nFAkC\Gamma_{cat}$$

- n number of electrons transferred in the half reaction
- F Faraday constant
- A electrode area
- k pseudo second order rate constant
- C analyte concentration
- $\Gamma_{cat}$  catalyst loading

Combining the above equations leads to the Koutecky-Levich expression, which describes the overall RDE limiting current  $I_{lim}$  for the electrocatalytic reaction over the entire potential range:

$$\frac{1}{I_{lim}} = \frac{1}{I_k} + \frac{1}{I_{lev}}$$

A plot of  $\frac{1}{I_{lim}}$  against  $\frac{1}{\omega^{1/2}}$  should yield a straight line whose slope is related to the number of electrons transferred in the reaction, and whose intercept is related to the kinetic current.



# 3 Chemical modifications I

## Heteroatom doped carbon microspheres with tunable sulfur binding states

---

### 3.1 Introduction

In terms of broadening the range of possible applications of carbon-based materials, strategies for the fine-tuning of material properties are required. The introduction of heteroatoms into carbon materials, also known as “doping”, is a useful method of altering their physical, electronic and chemical properties. Successful work so far includes the superior performance of doped carbons in applications such as electrode materials for catalysis<sup>29, 81-83</sup> or energy storage,<sup>84-89</sup> stationary phases,<sup>90, 91</sup> chemoselective adsorption,<sup>17, 18</sup> and many others. The majority of research in this field has focused on nitrogen doping, which is known to induce favorable changes in the carbon material, *e.g.* increased conductivity<sup>92, 93</sup> and high activity in the Oxygen Reduction Reaction (**ORR**) in fuel cells.<sup>29, 81-83</sup> The synthesis of nitrogen doped carbons has been achieved *via* a variety of pathways, such as post treatment of carbon with ammonia,<sup>94</sup> amines or urea<sup>95</sup> and also more direct approaches using acetonitrile,<sup>96</sup> pyrrol,<sup>97</sup> polyacetonitrile<sup>84, 92</sup> or polyaniline<sup>98</sup> as starting compounds. Complementing nitrogen as a dopant, sulfur is receiving increasing attention in current carbon materials research. In contrast to nitrogen which is often used to alter electronic properties of the carbon material, sulfur has been used more for the alteration of physical properties (*i.e.* to induce structural defects or increase interlayer spacing of graphitic lattices) and for applications where its easily polarizable lone pairs (and thus chemical reactivity) are of importance. Sulfur doped carbon materials have, for example, shown beneficial effects on the selective adsorption of waste metals<sup>17</sup> and the desulfurylation of crude oil.<sup>18</sup> The synthesis of these sulfur doped materials generally involves the pyrolysis of sulfur containing, polymer based carbons,<sup>17, 18, 99</sup> but also arc vaporization in the presence of sulfur containing compounds such as thiophenes.<sup>38</sup> Very recently, Yang *et al.* reported on the synthesis of sulfur doped graphene with enhanced electrocatalytic properties in the ORR, prepared by annealing graphene oxide and benzyl disulfide under argon at high temperatures (600 to 1050 °C).<sup>80</sup>

Concerning the combined incorporation of sulfur and nitrogen within the same material, only few reports currently exist. Sulfur-assisted growth of carbon nanotubes by chemical vapor deposition of acetonitrile was shown to increase the nitrogen doping levels as well as the magnetic properties of the nanotubes.<sup>100</sup> Choi *et al.* synthesized heteroatom doped carbon materials by the pyrolysis of amino acid/metal chloride composites. They were able to show that materials containing both nitrogen and sulfur increased the material's ORR activity in acidic media, relative to undoped or purely nitrogen doped carbons.<sup>35</sup> Tsubota *et al.* prepared sulfur and nitrogen dual doped carbons *via* the pyrolysis of thiourea and formaldehyde.<sup>36</sup> Their material exhibited superior performance as supercapacitor electrodes than commercial activated carbons. These examples hence indicate that materials doped simultaneously with sulfur and nitrogen are promising candidates for applications related to energy storage and conversion. In terms of sustainability, most of the aforementioned synthesis methods for heteroatom doped carbon materials show drawbacks in the often harsh reaction conditions used. Hydrothermal carbonization (HTC) is therefore an attractive alternative for the synthesis of doped carbon materials. In the context of HTC, the only dopant that has been discussed in literature is nitrogen. For example, nitrogen doped carbon microspheres were obtained by hydrothermally treating naturally occurring, nitrogen containing compounds, such as glycine, N-acetyl glucosamine or chitosan.<sup>44, 46, 65, 101</sup> Albumin, a glycoprotein, was used as structure directing additive in the HTC of glucose to produce nitrogen doped carbon aerogels.<sup>63</sup> The incorporation of nitrogen is assumed to rely on Maillard reactions which are known to take place between sugars and amino acids (refer to **chapter 2.1**). In order to extend the possibilities of HTC-derived products, it is of interest to investigate the incorporation of other heteroatoms such as sulfur.

This chapter concerns the initial synthesis and characterization of sulfur (and nitrogen) doped hydrothermal carbon microspheres before moving on to more sophisticated nano-architectures in the following chapters (**Fig. 3.1**). Glucose was used as a model starting material for sustainable feedstocks and was treated hydrothermally at 180 °C in the presence of sulfur (and nitrogen) containing additives. As an additive for carbon heteroatom doping, naturally occurring amino acid L-cysteine (**Cys**) was chosen due to its availability, low cost, and environmentally benign nature. A cysteine derivative, S-(2 thienyl)-L-cysteine (**TCys**) was also used in order to investigate the effect of the type of sulfur species (aliphatic thiol in Cys, aromatic thienyl in TCys) on the sulfur binding state in the final product. To obtain solely sulfur doped carbon

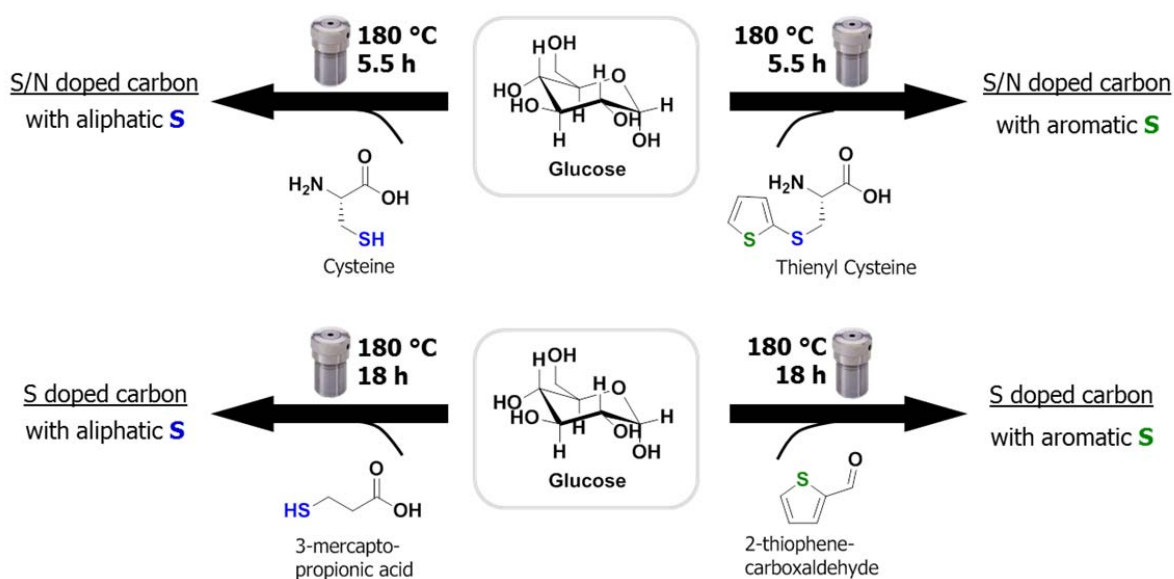


Fig. 3.1 graphical abstract of chapter 3

microspheres, 3-mercapto-propionic acid (MPA) and 2-thienyl-carboxaldehyde (TCA) were also used as additives. As with the amino acid doped carbons, the effect of aliphatic *versus* aromatic sulfur in the precursor on the sulfur binding state in the resulting sulfur doped carbon was investigated. In both cases, pyrolysis of the HTC products was carried out for additional control over material stability, functionality and electrical conductivity.

## 3.2 Mechanistic considerations

In accordance with the possible HTC mechanism presented in **chapter 2.1**, the underlying assumption for the work presented here was the following:

- aliphatically bound heteroatoms (*e.g.* thiol, amine) in the precursor would preferentially be incorporated into the hydrothermal carbon *via* nucleophilic addition or substitution reactions with HTC intermediates, *e.g.* hydroxymethylfurfural (HMF).
- aromatically bound heteroatoms (*e.g.* thiophene, pyrrol) would preferentially be incorporated *via* cycloaddition or electrophilic aromatic substitution (EAS) with HTC intermediates.

The incorporation mechanisms are expected to result in different heteroatom binding states in the resulting doped hydrothermal carbon, which in turn is expected to lead to distinct material

properties. To test this hypothesis, the following combinations of heteroatom sources were chosen:

- For the synthesis of sulfur and nitrogen doped carbon microspheres: L-Cysteine (**Cys**) and its derivative S-(2 thienyl)-L-cysteine (**TCys**), containing thiol and thienyl functionalities, respectively. The nitrogen is bound as amine in both cases.
- For the synthesis of sulfur doped carbon microspheres: 3-mercapto-propionic acid (**MPA**) and 2-thienyl-carboxaldehyde (**TCA**), containing thiol and thienyl functionalities, respectively. Furthermore, the synthesis of solely sulfur doped spheres allows for the investigation of heteroatom incorporation into hydrothermal carbon in the absence of amines, *i.e.* Maillard reactions.

### 3.3 Sulfur and nitrogen dual doped carbon microspheres

#### 3.3.1 Morphology and surface area

To study the effect of additive concentration on the HTC process of glucose, different amounts of Cys and TCys (0.1 g to 0.4 g) were added to a 10 wt % glucose solution (1.5 g glucose in 13.5 g water). The mixtures were placed into a glass liner and sealed into a Teflon line autoclave of 45 ml volume. HTC was carried out at 180 °C for 5.5 h. The resulting products were labeled **AAX**, where AA=Cys for L-cysteine, and AA=TCys for S-(2 thienyl)-L-cysteine. X denotes the mass (in g) of Cys or TCys added to the glucose solution. For pyrolyzed samples, the suffix **\_550** or **\_900** was added to the sample label for a pyrolysis temperature of **550 °C** and **900 °C**, respectively. Elemental analysis and SEM characterization was carried out for the entire series, but for further characterization and pyrolysis, samples **Cys0.2** and **TCys0.2** were chosen as representatives.

The hydrothermal carbonization of glucose at 180 °C normally results in interconnected carbonaceous spheres with  $D \sim 200$  nm. The scanning electron microscopy (**SEM**) images in **Fig. 3.2** show that with the addition of amino acids, a spherical morphology is also obtained. However, the amino acid addition results in discrete, rather than interconnected, microspheres which are considerably larger than for pure glucose and exhibit a broader size distribution (1  $\mu\text{m}$  up to 15  $\mu\text{m}$ ). With increasing concentration of Cys or TCys, there is a general increase in size up to about 20  $\mu\text{m}$  and also in the overall size distribution (data not shown).

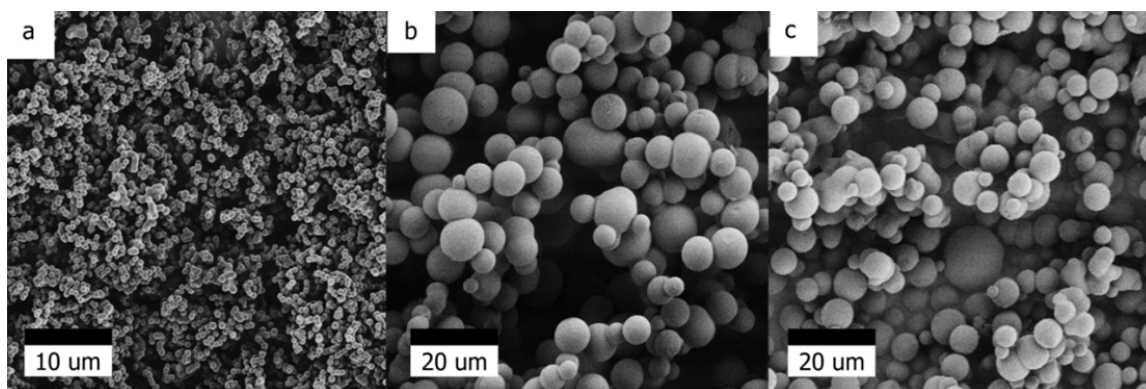


**Fig. 3.2** SEM images of solid product after HTC of a) pure glucose, b) glucose with cysteine (Cys0.2) and c) glucose with thienyl-cysteine (TCys0.2).

This change in particle size can be understood by considering how nucleation takes place in HTC and how the presence of additional reactants can affect the nucleation process. The LaMer model is widely cited in colloid chemistry to explain the formation of monodisperse particles from supersaturated solutions.<sup>102</sup> Briefly, it involves the increase in concentration of a dissolved species until a critical point is reached; at which rapid nucleation (“burst nucleation”) occurs. A growth phase follows, during which the remaining monomer in solution diffuses to the nuclei formed in the seeding stage. The first nucleation stage can be described as homogeneous nucleation whereas the growth phase is basically heterogeneous nucleation, because monomers add onto pre-existing nuclei.<sup>103</sup> Once the first species has formed nuclei *via* homogeneous nucleation, the next species may preferentially nucleate heterogeneously and therefore determine the final number of particles and their size. The difference in solubility of formed intermediates in water and the changing solvent properties of water itself as it is heated to 180 °C results in variations in the critical concentrations needed to drive nucleation. The more complex the reaction mixture, the more different products are formed at different points in time.<sup>104, 105</sup> A higher amount of amino acid (which reacts with glucose *via* Maillard reactions) is therefore expected to result in an increased particle size and overall size distribution. Maillard reactions occur rapidly compared with HTC of pure glucose, so the presence of amino acids accelerates particle formation. This is reflected in the significantly lower reaction times required for the amino acid containing samples (5.5 h to obtain a solid yield of *ca.* 30 wt % with respect to total mass of starting material) compared to pure glucose (16 h are required to obtain similar yields.). In terms of surface area, the materials show no detectable porosity after HTC at 180 °C, but exhibit some microporosity after pyrolysis due to the loss of strongly micropore-bound

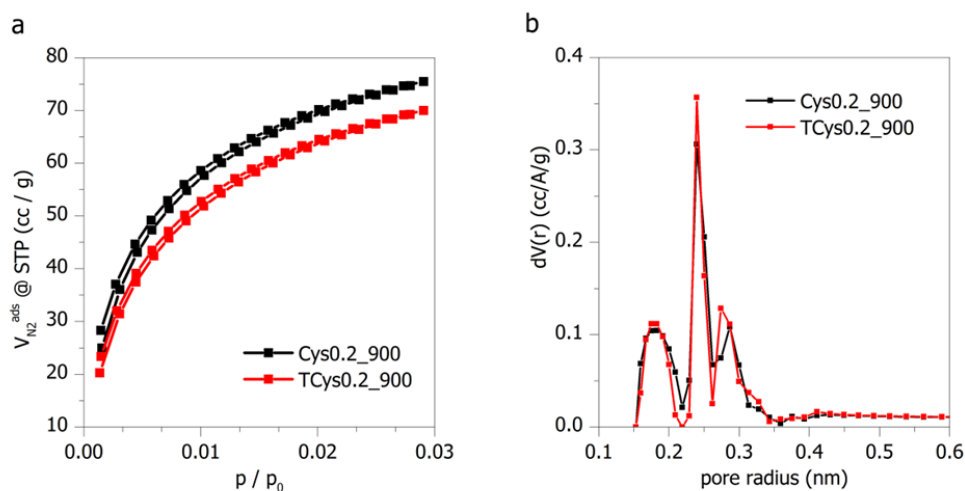


**Fig. 3.3** a) CO<sub>2</sub> sorption isotherms for Cys0.2\_900 (black) and TCys0.2\_900 (red). b) the corresponding pore size distributions.

decomposition products during the heat treatment.<sup>45, 106</sup> Additionally, the reversibility of Diels-Alder reactions may facilitate the loss of larger material fractions. At a pyrolysis temperature ( $T_p$ ) of 550 °C, nitrogen adsorption isotherms yield BET surface areas of 440 m<sup>2</sup> g<sup>-1</sup> and 281 m<sup>2</sup> g<sup>-1</sup> for Cys0.2\_550 and TCys0.2\_550, respectively (isotherms not shown). Interestingly, the surface area obtained for TCys0.2\_550 is much lower than for Cys0.2\_550, indicating that there are inherently less unstable, volatile moieties present.

After pyrolysis at 900 °C, the nitrogen uptakes are negligible. A similar effect was already reported by White *et al.* who attributed this to micropore closure upon further carbon network condensation.<sup>63</sup> However, sorption isotherms obtained with CO<sub>2</sub> show that pore shrinkage, rather than complete closure, has occurred. Ultramicropores (*i.e.* smaller than 1 nm in diameter) giving rise to surface areas of around 630 m<sup>2</sup> g<sup>-1</sup> in the case of Cys0.2\_900, and around 730 m<sup>2</sup> g<sup>-1</sup> in the case of TCys0.2\_900 were observed (**Fig. 3.3**).

### 3.3.2 Elemental composition and the effect of the dopant source on the binding states of the heteroatoms in the hydrothermal carbon

The presence of sulfur and nitrogen was verified by elemental analysis. **Table 3.1** summarizes the elemental composition (in wt %, shown in black) of varying amounts of Cys and TCys added to a constant amount of glucose prior to hydrothermal treatment. The deviation of the S/N

ratio for the amino acid additives from the final carbonaceous products immediately confirms that the amino acids have reacted in an asymmetric fashion.

The variability of the S/N values of the different carbon samples and also from the additives implies a complex incorporation mechanism. Overall, the trend shows decreasing S/N values with increasing addition of amino acids, indicating the loss of nitrogen containing moieties. One of the major differences in the trend of sulfur content between Cys and TCys containing samples is that while significant increase in sulfur content is observed as a function of increasing Cys concentration (from 5.7 wt % to 11.9 wt %), TCys containing samples show no pronounced change in the sulfur content. Over the same concentration range there is a less than 2 wt % increase in sulfur content, while at the lowest concentration, the sulfur doping is already at 10.7 wt % and remains roughly constant throughout the series of experiments. This is a first indication that the incorporation mechanisms of the two amino acids are inherently different. Samples Cys0.2 and TCys0.2 were chosen as representatives of the Cys and TCys experiment series, respectively. They were pyrolyzed at both 550 °C and 900 °C, which was expected to result in higher conductivity and stability of the material due to thermally induced rearrangement

**Table 3.1 Elemental analysis data (wt %) for a) the glucose + Cys experiment series and b) the glucose + TCys experiment series. The surface elemental composition for Cys0.2, TCys0.2 and the corresponding pyrolyzed samples at 550 °C and 900 °C are shown in grey. The quantities were converted from at % to wt % in order for direct comparison with results from elemental analysis.**

a)	Elemental Analysis (wt %)					b)	Elemental Analysis (wt %)				
	XPS (wt %)						XPS (wt %)				
Sample	C	H	N	S	S/N	Sample	C	H	N	S	S/N
Cys0.1	62.4	4.8	3.3	5.7	1.7	TCys0.1	61.6	4.3	2.6	10.7	4.1
Cys0.2	62.9	4.8	3.7	9.7	2.6	TCys0.2	61.8	4.5	2.6	12.0	4.6
	69.28	-	2.64	6.05	2.29		70.66	-	2.35	3.42	1.46
Cys0.3	60.9	5.0	3.9	9.9	2.5	TCys0.3	61.7	4.5	3.5	11.4	3.2
Cys0.4	60.7	4.8	4.3	11.9	2.8	TCys0.4	61.1	4.5	3.6	12.6	3.5
Cys0.2_550	79.2	2.9	4.6	4.7	1.0	TCys0.2_550	76.9	2.8	3.7	11.2	3.1
	84.88	-	3.00	4.32	1.44		86.84	-	2.23	4.08	1.83
Cys0.2_900	89.0	0.5	4.5	3.0	0.7	TCys0.2_900	82.2	0.9	3.7	7.2	2.0
	90.48	-	2.14	3.61	1.69		88.18	-	6.60	3.42	3.31
L-Cysteine*	29.7	5.8	11.6	26.5	2.3	Thienyl-Cysteine*	41.3	4.4	6.9	31.6	4.6

\* calculated values

of the carbon framework into a more graphitic structure. Because the type of hydrothermal carbon (*i.e.* derived from different precursors) strongly influences the effects of pyrolysis, and the presented materials are a new class of hydrothermal carbon, it is important to study their physicochemical properties after pyrolysis at different temperatures. For both the Cys and TCys containing samples, the nitrogen content increases by about 1 wt % during pyrolysis (compared to Cys0.2 and TCys0.2). This is caused by the loss of other atoms such as oxygen, hydrogen and sulfur which increase the relative wt % of nitrogen without additional incorporation. An interesting difference between the two acids was observed regarding the sulfur content after pyrolysis. For Cys0.2 the sulfur content is already halved at  $T_p = 550\text{ }^\circ\text{C}$ , whereas the material containing TCys shows a sulfur loss of less than 1 wt %. At  $T_p = 900\text{ }^\circ\text{C}$  the sulfur content in Cys0.2\_900 is now merely a third of that before pyrolysis while for TCys0.2\_900 it is approximately half. The material obtained with TCys exhibits higher thermal stability with respect to sulfur loss than the one obtained with Cys, which is presumably caused by a difference in the sulfur binding state. Choi *et al.* also obtained sulfur and nitrogen dual doped carbon materials *via* the pyrolysis at  $900\text{ }^\circ\text{C}$  of cysteine in the presence of metal salts.<sup>35</sup> They obtained a sulfur content of 2.7 wt % which is similar to the value obtained for TCys0.2\_900 (3.0 wt %). Notably, the amounts of cysteine used by Choi *et al.* are much higher than for Cys0.2\_900 because in their work, cysteine was both sulfur and carbon source. This shows that by using cysteine as the sulfur source, where sulfur is bound aliphatically, there seems to be a limit as to how much sulfur can be retained after heat treatment and also that higher sulfur incorporation efficiencies are achieved by using HTC. For TCys0.2\_900 however, more than 7 wt % sulfur can be retained even after heat treatment at  $900\text{ }^\circ\text{C}$ . The retention of sulfur after pyrolysis of the carbon materials therefore seems to depend strongly on the type of sulfur source used and how the sulfur is bound within the material. In order to further investigate the atom binding states of the doped carbons, X-Ray photoelectron spectroscopy (**XPS**) was carried out on Cys0.2, TCys0.2 and the corresponding post-treated samples at  $550\text{ }^\circ\text{C}$  and  $900\text{ }^\circ\text{C}$ . The surface elemental composition (converted from at % to wt % for direct comparison with elemental analysis) is shown in grey in **Table 3.1**. In contrast to the results from elemental analysis, the values for the sulfur content are similar for Cys and TCys. Since XPS is a surface sensitive technique and elemental analysis applies to the bulk, this indicates that most of the sulfur atoms in TCys are bound within the particle core as structural sulfur.



**Table 3.2** summarizes the obtained XPS data. Images of the deconvoluted C1s, N1s and S2p scans may be found in the appendix (**Fig. A 1 to Fig. A 3**). The C1s scans show several peaks with varying contributions at different pyrolysis temperatures. In general, the binding energy value of 285 eV can be assigned to  $sp^2$  hybridized carbon in an aromatic environment (**C1**). The contribution of this peak increases with increasing temperatures. The second highest contribution comes from carbon atoms bound to sulfur, nitrogen or oxygen in the form of thiols, sulfonates, amines or alcohols (**C2**). There are minor contributions from carbonyl/amide groups (**C3**) and ester/carboxylic groups (**C4**).  $\pi-\pi^*$  shake up satellite peaks typical for conjugated aromatic systems are seen only for the samples treated under the highest pyrolysis temperature of 900 °C (**C5**). Overall, the C1s binding energies confirm that carbonization and aromatization increase after pyrolysis, and that a significant amount of surface carbon atoms are

**Table 3.2 Peak assignments for the C1(s), N 1(s) and S 2(p)3/2 photoelectron envelopes for Cys0.2 and TCys0.2 samples after HTC at 180 °C and subsequent pyrolysis at 550 °C and 900 °C**

Peak	Binding Energy (eV)						Assignment
	fraction of species (%)						
	Cys0.2	Cys0.2_550	Cys0.2_900	TCys0.2	TCys0.2_550	TCys0.2_900	
<b>C1s</b>	285	285	285	285	285	285	<b>C1</b> $sp^2$ C-C/C-H <sup>35, 46, 99</sup>
	64.1	72.3	73.3	44.4	84.8	74.5	
	286.38	286	286.2	286.1	286.3	286	<b>C2</b> C-O / C-N / C-S <sup>35</sup>
	25.2	23.3	15.0	47.1	12.8	15.8	
	287.84	288.18	287.54	288.1	288.35	287.3	<b>C3</b> C=O / C=N <sup>35, 106</sup>
	6.5	2.1	4.7	6.4	2.3	4.7	
	289.08	289.6	289.04	289	-	289.03	<b>C4</b> O=C-O <sup>106</sup>
4.2	2.3	3.8	2.1	-	3.6		
-	-	291.1	-	-	291	<b>C5</b> $\pi-\pi^*$ shake up satellite <sup>18, 46</sup>	
-	-	3.3	-	-	4.1		
<b>N1s</b>	-	398.57	398.54	-	398.85	398.86	<b>N1</b> pyridinic <sup>44, 46</sup>
	-	23.9	27.5	-	41.3	26.9	
	399.98	-	-	-	-	-	<b>N2</b> amine <sup>46</sup>
	79.8	-	-	-	-	-	
	-	400.69	-	400.10	400.96	-	<b>N3</b> pyrrolic <sup>44</sup>
-	62.0	-	77.4	58.7	-		
401.24	-	401.25	-	-	401.29	<b>N4</b> quaternary <sup>35, 44</sup>	
20.2	-	72.9	-	-	73.1		
-	404.10	-	402.29	-	-	<b>N5</b> pyridinic N-Oxide <sup>35</sup>	
-	14.1	-	22.6	-	-		
<b>S2p<sub>3/2</sub></b>	163.77	-	-	-	-	-	<b>S1</b> thiol, disulfide or thioether <sup>35, 99, 107</sup>
	81.2	-	-	-	-	-	
	-	164.26	164.27	164.22	164.35	164.26	<b>S2</b> Thiophenic (aromatic) <sup>99, 107</sup>
-	94.4	92.6	93.6	100.0	85.3		
-	165.95	166.65	167.44	-	165.30	<b>S3</b> oxidized sulfur <sup>99, 108</sup>	
-	18.8	7.4	6.3	-	14.4		

bound to either sulfur, nitrogen or oxygen. Only a small fraction of the heteroatoms bound to carbon are present in an oxidized state. In the case of nitrogen-containing functional groups, a trend of formation of increasingly stable binding states with increasing pyrolysis temperature can be seen, *i.e.* from amine (**N2**), pyridinic oxide (**N5**) and pyrrolic (**N3**) towards quaternary graphitic (**N4**) and pyridinic (**N1**). The samples treated at 900 °C contain only nitrogen bound within the carbon framework (quaternary) or at the edges of the framework (pyridinic). After HTC at 180 °C, Cys0.2 contains mainly surface amine groups (79.8 % of nitrogen species), whereas mainly pyrrolic functionalities (77.4 % of nitrogen species) were observed. After pyrolysis at both 550 °C and 900 °C, the nitrogen binding states are similar for both amino acids. In the case of sulfur-containing functional groups, the trend is not as straightforward. For Cys0.2, the majority of sulfur species are present as aliphatic thiols, disulfides or thioethers (**S1**), with the remainder being oxidized sulfur species (**S3**). No thiophenic sulfur (**S2**) could be found. This dramatically changes upon pyrolysis at 550 °C and 900 °C, where after all aliphatic sulfur species disappear and more than 90 % of sulfur is thiophenic. For TCys0.2, most of the surface sulfur is thiophenic already after HTC at 180 °C. After pyrolysis at 550 °C, 100 % of surface sulfur is bound in a thiophenic state. After pyrolysis at 900 °C, some oxidized species appear (14.4 % of sulfur species). This may be the result of the reaction of surface sulfur with adjacent oxygen molecules. Overall, XPS analysis suggests that using Cys as additive results in pending functional groups (amines, thiols), whereas the addition of TCys results in the incorporation of sulfur into the carbon framework already at early stages of the reaction process. For further insight into the chemical environment of the bulk, solid state  $^{13}\text{C}$  magic angle spinning solid state nuclear magnetic resonance ( $^{13}\text{C}$  MAS ssNMR) spectra were recorded (**Fig. 3.4**). A spectrum of pure glucose hydrothermally treated at 180 °C is shown for reference (**Glu\_180**, grey line). General regions of interest can be assigned as follows: carbonyl and carboxylic acid groups at 210 ppm to 175 ppm, furanic groups at 175 ppm to 100 ppm and finally aliphatic groups at < 75 ppm.<sup>42, 46, 51</sup>  $\text{Sp}^2$  hybridized carbon atoms in aromatic rings generally resonate at around 128 ppm – 130 ppm.<sup>51, 54, 55</sup> More specifically, in the Glu\_180 spectrum, the peaks at 150 ppm and 110 ppm – 118 ppm correspond to the carbon atoms of furan, labeled C1 and C2, respectively (**Fig. 3.4 II**).<sup>54</sup> While the carbonyl regions are similar for Glu\_180 and the doped samples (**Fig. 3.4 I**), a clear difference in spectra is found in the regions **II** to **VI**. The furanic peaks are still present in the doped samples, although the relative intensities are greatly shifted. The resonance at 110 ppm – 118 ppm, which is strong for Glu\_180, only appears as a weak shoulder in Cys0.2

and TCys0.2, which directly shows that the contribution of furanic sites has decreased significantly. The peak at 150 ppm, on the other hand, which in furans should have a similar intensity as the one at 110 ppm – 118 ppm, appears as a very strong, sharp signal in the doped samples (**Fig. 3.4 III**). The high intensity can be attributed to both the presence of mobile heteroatom substituents on aromatic rings.<sup>109-111</sup> This would give rise to the observed peak sharpness due to high mobility. Contributions from thiophene rings and pyrrolic or pyridinic units in the region of 142 ppm - 157 ppm are seen as weak shoulders.<sup>112-114</sup> An additional strong signal at approximately 130 ppm is found both for Cys0.2 and TCys0.2 which is entirely absent for Glu\_180 (**Fig. 3.4 IV**). This “all carbon-bound aromatic” peak is typical for pyrolyzed hydrothermal carbon, *i.e.* after decarboxylation and aromatization have taken place.<sup>46, 55</sup> However, for the doped materials, this peak is already present before post treatment, indicating that a significant amount of structural aromatization/pseudo graphitization takes place throughout hydrothermal treatment. This effect has previously been observed for nitrogen-doped hydrothermal carbon obtained from glycine and N-acetyl-glucosamine.<sup>46, 65</sup> Comparing Cys0.2 and TCys0.2 with each other, it can be seen that aromatization is more pronounced for TCys0.2. In the aliphatic region (**Fig. 3.4 V and VI**), a significant broadening, as well as an upfield shift of the peaks is observed for the Cys/TCys containing samples. The peak at around 25 ppm may refer to aliphatic thiol groups,<sup>115</sup> but a simple shift of the methyl/methylene peaks due to a

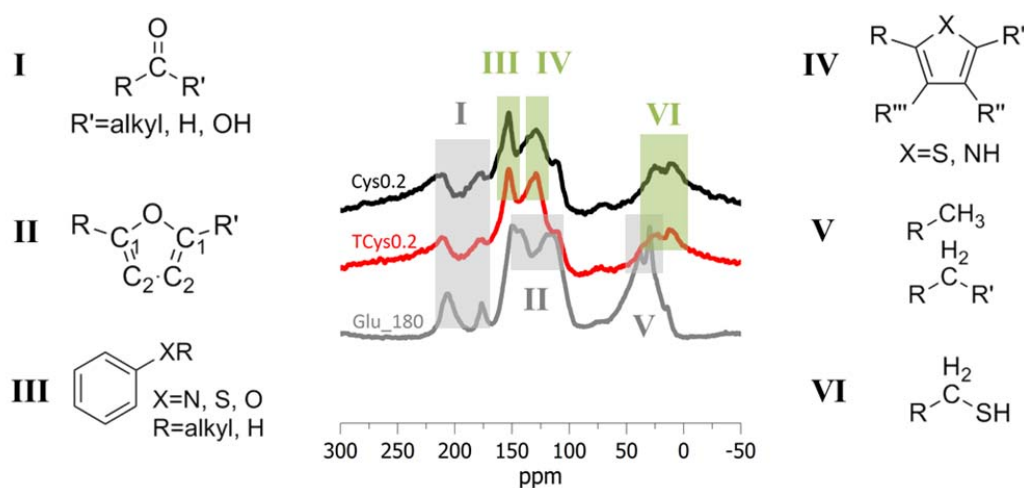


**Fig. 3.4**  $^{13}\text{C}$  MAS ssNMR spectra for Cys0.2 (black) and TCys0.2 (red) after hydrothermal treatment at 180 °C (black). A spectrum obtained from pure glucose hydrothermal carbon is shown for reference (grey).

different chemical environment within the doped framework cannot be excluded. The peak observed at 9 ppm seems low and an assignment cannot currently be provided. Qualitatively however, it can be said that the intensity of the aliphatic *versus* the aromatic region is smaller for the doped samples, implying an overall higher fraction of atoms being present in a condensed, aromatic structure, rather than bound in aliphatics.

Fourier-transform infrared spectroscopy (FT-IR) analysis (Fig. 3.5) similarly indicated a higher degree of aromatization for the sulfur/nitrogen doped carbon spheres relative to an FT-IR spectrum of pure glucose hydrothermal carbon (Glu\_180, grey line). The spectrum of Glu\_180 shows characteristic bands at  $\sim 3300\text{ cm}^{-1}$  (hydroxyl groups),  $\sim 2900\text{ cm}^{-1}$  (aliphatic methyl and methylene groups),  $\sim 1710\text{ cm}^{-1}$  (carbonyl functionalities),  $\sim 1620\text{ cm}^{-1}$  (aromatic C=C) and  $\sim 1020\text{ cm}^{-1}$  (furanic C=C-O).<sup>42, 106</sup> Various oxidized carbon functionalities that are expected to be found in hydrothermal carbon (ether, lactone, *etc.*) are represented by bands in the  $1500\text{ cm}^{-1}$  to  $1000\text{ cm}^{-1}$  region. The spectra of Cys0.2 and TCys0.2 are similar to each other, but show subtle differences to that of glucose, which are highlighted in grey. The -OH band at  $\sim 3300\text{ cm}^{-1}$  is broader for the doped samples with the peak at  $\sim 2900\text{ cm}^{-1}$  being slightly more pronounced. This is attributed to additional bands arising from amide N-H vibrations. The corresponding amide C=O bands are found at  $\sim 1660\text{ cm}^{-1}$ . These bands are entirely absent in Glu\_180, indicating that part of the aldehyde or carboxylic acid functionalities are replaced by amide groups in the doped samples, presumably *via* nucleophilic attack of the Cys or TCys free

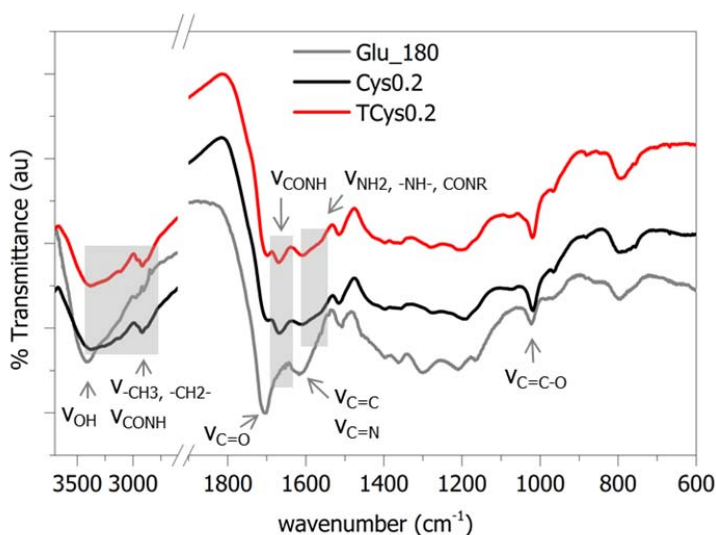


Fig. 3.5 FT-IR spectra of Cys0.2 and TCys0.2 after HTC at 180 °C for 5.5 h. An FT-IR spectrum of pure glucose hydrothermal carbon is shown for reference (Glu\_180, grey line).

amino groups on the carbonyls. In the doped samples, the carbonyl band at  $1710\text{ cm}^{-1}$  and the amide band have decreased intensities relative to the aromatic C=C band at  $1620\text{ cm}^{-1}$ , indicating a higher degree of aromatization than Glu\_180 (where the carbonyl band is more pronounced than the aromatic C=C band). Cyclic C=N vibrations present in pyrrolic and quaternary nitrogen functionalities would also contribute to the broad band at  $\sim 1620\text{ cm}^{-1}$ , in accordance with XPS data.

### 3.3.3 Physical properties – crystallinity and conductivity

The results obtained from X-ray diffraction (XRD) measurements are summarized in **Table 3.3** and **Fig. 3.6**. For the samples before post treatment, a broad peak at around  $19^\circ$  is found, indicative of amorphous materials. After pyrolysis at  $550^\circ\text{C}$ , two peaks at roughly  $22^\circ$  and  $41^\circ$  appear which shift to around  $23^\circ$  and  $44^\circ$  after pyrolysis at  $900^\circ\text{C}$ , respectively. While these values are in a similar range as the values for graphitically ordered carbons ( $26^\circ$  and  $43^\circ$ , corresponding to the 002 and 100 lattice spacing),<sup>116</sup> they also indicate that the interlayer spacing of the sulfur and nitrogen doped materials are much larger than in graphite. A similar increase in the interlayer spacing was observed for undoped hydrothermal carbons, showing that the material obtained contains many structural defects even after post carbonization. The point of interest here, however, is the considerable increase in the d-spacing of the TCys materials compared to the Cys materials. This effect is already known for nitrogen doped carbon.<sup>117</sup> In the case of sulfur doping, the interlayer distance is expected to increase even more due to the large size of the sulfur atom. Glenis *et al.* observed an interlayer expansion of 0.048 after S doping into graphite (from  $3.357\text{ \AA}$  to  $3.405\text{ \AA}$ ).<sup>38</sup> In their case, the sulfur atoms were located between the graphite layers, whereas in the herein presented material, sulfur is incorporated into the carbon framework. This is expected to cause buckling of the carbon layers and give rise to an even larger increase in the d-spacing, as is indeed observed. Also note the increased intensity at lower angles for the samples after pyrolysis at  $900^\circ\text{C}$ . This is indicative of the presence of pseudo-periodic ordered micropores which cause X-Ray diffraction in a similar manner as crystal lattices and has been observed for pyrolyzed hydrothermal carbon before.<sup>44, 46</sup> These findings are hence coherent with the sorption data shown earlier.

The specific conductivity values of the materials are given in **Table 3.3**. The conductivity is low up to calcination temperatures of  $550^\circ\text{C}$ , as the occurring rearrangements were insufficient to create a cohesive aromatic system (which is required for good electrical conductance).

This clearly points to the fact that the observed aromatization throughout HTC in the presence of amino acids is an isolated, tectonic process. Once pyrolyzed at 900 °C however, the conductivity of the doped materials is more than three times higher for Cys0.2\_900 than for Glu\_900. The slightly improved conductivity of Cys0.2\_900 over TCys0.2\_900 is attributed to the even increased sulfur content of TCys0.2\_900. It has been reported that sulfur can act as n-type dopant in graphite and diamond semiconductors and Kumari *et al.* showed that sulfur doping increases the conductivity of amorphous carbon films at optimum concentrations, but causes a decreased conductivity if present in excess.<sup>118, 119</sup> Similar effects have been reported for nitrogen doping. The conductivity dependence on the dopant concentration can be explained by a competition of two processes taking place. On the one hand, the incorporation of dopants results in a disordered graphitic lattice while, on the other hand, additional charge carriers are introduced into the system.<sup>120</sup> A maximum in conductivity is therefore observed when a compromise between the two effects is reached. Therefore it could be postulated that, while the nitrogen content in the doped carbon microspheres is in the correct range to increase conductivity, the sulfur content in the TCys0.2\_900 sample is too high, hence causing a slight decrease in charge carrier availability. However, the specific conductivity values are still superior compared to undoped carbon, making electronic or electrochemical applications feasible.

**Table 3.3 Summary of the d-spacing for Cys0.2 and TCys0.2 after HTC at 180 °C and post pyrolysis at 550 °C and 900 °C. The specific conductivity values of pyrolyzed samples are given on the right. Specific conductivity values of pure glucose pyrolyzed at 550 °C and at 900 °C are shown for reference.**

Sample	2 $\Theta$ (°)	d-spacing (Å) <sup>a</sup>	Specific conductivity (S m <sup>-1</sup> )
Cys0.2	19.9	4.46	-
Cys0.2_550	22.8	3.90	7 x 10 <sup>-4</sup>
Cys0.2_900	23.9	3.72	2657
TCys0.2	18.2	4.87	-
TCys0.2_550	21.8	4.08	2 x 10 <sup>-5</sup>
TCys0.2_900	22.8	3.90	2019
Glu_180_550	-	-	6
Glu_180_900	-	-	832

<sup>a</sup> The Bragg equation,  $n\lambda = 2d \sin\Theta$  was used for the calculation, where  $n$  is an integer,  $\lambda$  is the wavelength of the incident wave (Cu $\alpha$  radiation,  $\lambda = 1.542$  Å),  $d$  is the spacing between the planes in the atomic lattice, and  $\Theta$  is the angle between the incident ray and the scattering planes.

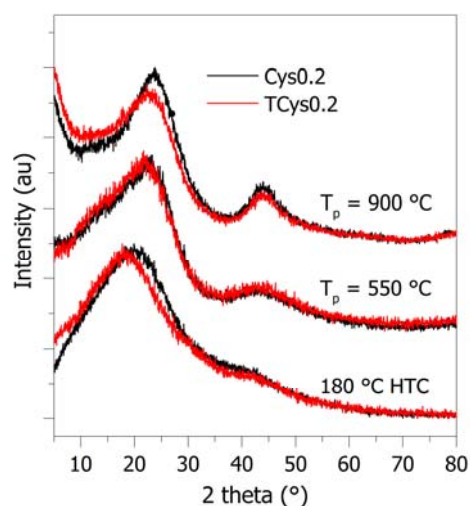


**Fig. 3.6 XRD diffractogram of Cys0.2 (black lines) and TCys0.2 (red lines) after HTC at 180 °C and after subsequent pyrolysis at 550 °C and 900 °C.**

### 3.4 Sulfur doped carbon microspheres

In order to investigate whether the incorporation of heteroatoms into hydrothermal carbon can only proceed *via* Maillard chemistry, the synthesis of solely sulfur doped carbon spheres was attempted. The additives used were 2-thienyl-carboxaldehyde (**TCA**) and 3-mercaptopropionic acid (**MPA**), again with the purpose of investigating the difference in aliphatic *versus* aromatic sulfur in the precursors on the final sulfur binding state. 0.2 g of the corresponding sulfur source was added to 1.5 g of glucose dissolved in 13.5 g of water. The samples were labeled **MPA0.2** and **TCA0.2**, containing MPA and TCA, respectively. Pyrolysis was carried out at 900 °C and the suffix **\_900** was added to the sample labels.

After HTC of the reaction mixture at 180 °C for 5.5 h, the yield obtained was negligible. It was concluded that amino functionalities were required to achieve enhanced reaction rates (due to Maillard reactions). As a rule of thumb, the rate of Maillard reactions at least doubles when the temperature is increased by 10 °C.<sup>62</sup> Even the thiol (a soft nucleophile) in MPA is expected to react rather slowly due the hard/soft mismatch with the carbonyl (hard electrophile) functionalities of HTC intermediates. Additionally, once nucleophilic attack of the thiol into a carbonyl group has taken place, the resulting thio-acetal is expected to be stable or the reverse of the reaction takes place to reform the carbonyl and thiol groups (amines on the other hand can form imines which can react further, *e.g. via* Diels Alder reactions). The reaction mixtures were therefore treated at 180 °C for 18 h to obtain maximum yields or around 30 wt %, a value which is typical for hydrothermal carbon.<sup>28</sup>

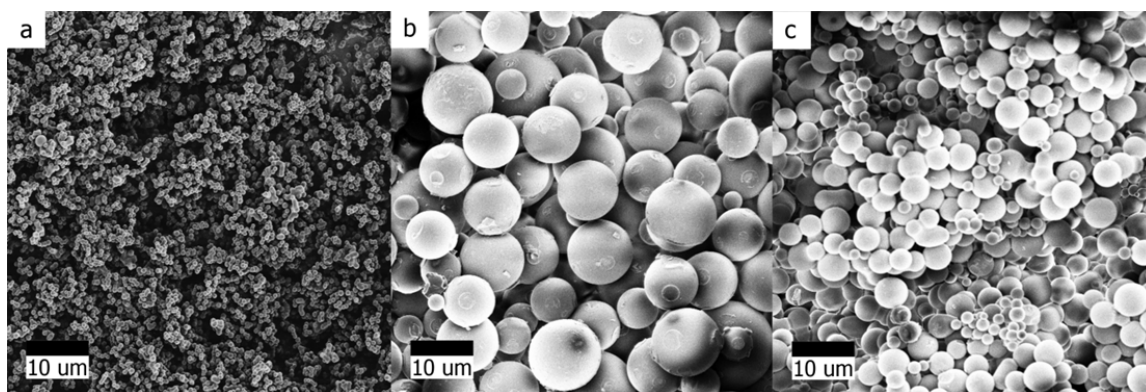


Fig. 3.7 SEM images of a) Glu\_180, b) MPA0.2 and c) TCA0.2 after HTC at 180 °C for 18 h.

SEM analysis reveals a spherical morphology for both sulfur-doped samples (**Fig. 3.7b and c**). An SEM image of pure glucose HTC is shown for reference (Glu\_180, **Fig. 3.7a**). MPA0.2 comprises discrete spheres with an average diameter of *ca.* 10  $\mu\text{m}$  whereas TCA0.2 consists of relatively smaller particles (average diameter *ca.* 4  $\mu\text{m}$ ). Both sample exhibit a wide size distribution, as is expected for HTC of glucose in the presence of additives which can give rise to more complex reaction schemes. It is interesting that MPA0.2 comprises significantly larger microspheres than TCA0.2. Presumably MPA reacts faster than TCA with glucose and HTC intermediates, forming nucleation seeds at earlier stages.

Successful sulfur incorporation was confirmed by elemental analysis. After HTC at 180  $^{\circ}\text{C}$ , MPA0.2 and TCA0.2 contained similar amounts of sulfur (**Table 3.4**). After pyrolysis at 900  $^{\circ}\text{C}$ , the sulfur content of MPA0.2 drops down to less than half whereas the sulfur content of TCA0.2\_900 is still at  $\sim 66\%$  of that in TCA0.2. TCA0.2\_900 also has a higher yield of solid recovered after pyrolysis (52.3 wt %) compared with MPA0.2\_900 (34.9 wt %). This indicates that the TCA containing sample is more thermally stable with respect to sulfur loss than the MPA containing sample. This is in agreement with results from the previous section, where the TCys (aromatic sulfur) containing sample showed higher sulfur retention than the Cys (aliphatic sulfur) containing sample. There, this observation was attributed to the difference in the sulfur binding state in the hydrothermal carbon after HTC at 180  $^{\circ}\text{C}$ , which was already more stable if TCys was used rather than Cys. It is inferred that the same situation applies to the sulfur doped carbons obtained *via* the addition of MPA or TCA. The dominant sulfur species in TCA0.2 is

**Table 3.4 Elemental analysis data (wt %) for sulfur doped carbon derived from MPA and TCA as additives in HTC of glucose after HTC at 180  $^{\circ}\text{C}$  and subsequent pyrolysis at 900  $^{\circ}\text{C}$ . [NB]: Values for the yield as well as the specific conductivity are given on the right.**

Sample	Elemental Analysis (wt %)			Yield (wt %)	Specific conductivity ( $\text{S m}^{-1}$ )
	C	H	S		
MPA0.2	63.9	4.8	5.8	31.8a	-
TCA0.2	65.6	4.2	5.7	32.6a	-
MPA0.2_900	95.0	0.9	2.5	34.9b	1390
TCA0.2_900	93.9	0.9	3.8	52.3b	1710

a = with respect to total mass of contributing reactants (*i.e.* glucose and MPA/TCA)

b = with respect to total mass of dried hydrothermal carbon placed in crucible prior to pyrolysis.



expected to be thiophene and the dominant sulfur species in MPA0.2 is expected to be aliphatic thiol (or thiol-ether) or oxidized sulfur species. The specific conductivity values of the pyrolyzed samples demonstrate that doping with sulfur (within the range from 2.5 to 3.8 wt %) increases the material conductivity (the specific conductivity of pure glucose hydrothermal carbon after pyrolysis at 900 °C was measured to be 832 S m<sup>-1</sup>).

### 3.5 Implications of the heteroatom binding state

The heteroatom binding motif is relevant with respect to chemical, mechanical and electrical properties arising from different heteroatom binding states. Pending surface thiol or amino groups could, for example, be useful for the adsorption of metal nanoparticles in a catalyst support material. These functionalities are expected to be dominant for the low temperature (*i.e.* after HTC at 180 °C) Cys or MPA containing carbons. On the other hand, structurally bound sulfur and nitrogen are known to alter electronic properties such as conductivity.<sup>38</sup> Bandosz *et al.* highlighted the importance of distinguishing between structural (C-S-C type) and pending (thiol or sulfonate) sulfur in the selective arsine adsorption capacities of sulfur containing carbons.<sup>17</sup> Pyrolysis at sufficiently high temperatures (here, above 550 °C) tends to result in the conversion of pending functionalities into more stable structural and aromatic functionalities *via* thermally induced rearrangements of the carbonaceous framework. However, the heteroatom binding state in the material prior to pyrolysis had a large influence on the amount of heteroatoms that can be retained during heat treatment. It was demonstrated that more sulfur could be retained upon heat treatment if it was already structurally bound in the as-synthesized carbon, whereas the majority of sulfur was lost if the sulfur was aliphatically bound. During the heat thermally induced rearrangements, heteroatoms are partially lost, resulting in lower doping levels of the pyrolyzed product. For example, Choi *et al.* obtained sulfur and nitrogen doped carbons *via* the direct pyrolysis of cysteine in the presence of metal salts.<sup>35</sup> Cysteine was the sole precursor and they obtained sulfur doping levels of *ca.* 3 wt %. If HTC is carried out in the presence of cysteine and the product is pyrolyzed at the same temperature (900 °C), similar sulfur doping levels are obtained but much less cysteine is required because the majority of carbon comes from glucose. Using HTC therefore allows for the synthesis of an “intermediate” carbonaceous material which allows much more efficient use of heteroatom sources compared to direct pyrolysis. If this

“intermediate” contains more stable heteroatom binding states, more heteroatoms, *i.e.* higher doping levels, can be retained during heat treatment.

### 3.6 Summary of chapter 3

This chapter demonstrated that the incorporation of sulfur atoms can be very easily achieved *via* HTC of glucose in the presence of sulfur containing additives. By using the amino acid cysteine and its derivative thienyl-cysteine, sulfur and nitrogen dual doped hydrothermal carbons could be synthesized. Earlier statements that amino groups and resulting Maillard reactions accelerate the HTC process were confirmed. Maillard reactions are however not necessary for the incorporation of heteroatoms, as was demonstrated with the synthesis of solely sulfur doped carbon microspheres *via* the addition of 3-mercapto-propionic acid (MPA) or 2-thienyl-carboxaldehyde (TCA) (which require longer reaction times of 18 h). The main advantage of the work presented here is that the binding state of sulfur could be tuned by varying the type of sulfur source as well as the pyrolysis temperature. If sulfur is bound aromatically in the precursor, it is most likely incorporated *via* cycloaddition or electrophilic aromatic substitution reactions which leave the aromatic ring intact in the product. In contrast, aliphatically bound sulfur (thiol) may be incorporated *via* nucleophilic substitution or Michael addition reactions and therefore more likely result in aliphatic binding motifs (thiol ether) in the HTC product. Post pyrolysis resulted in more stable, aromatic binding states as the temperature is increased from 550 °C to 900 °C due to thermal rearrangements of the carbonaceous framework. Importantly, the presence of aromatic binding states in the as-synthesized hydrothermal carbon allowed for higher heteroatom retention levels after pyrolysis and hence more efficient use of dopant sources. In this regard, HTC may be considered as an “intermediate” step in the formation of conductive heteroatom doped carbon for electronic applications. Both nitrogen and sulfur act to increase the conductivity of the doped carbon material. However, when more than *ca.* 7 wt % sulfur was present, the conductivity seems to decrease again. One can anticipate that the easily polarizable sulfur atoms may play a role in applications such as catalysis. Due to the low surface area of the doped microspheres presented in this chapter, it was difficult to test the doped materials for electrochemical applications. Therefore, different strategies were needed for the introduction of surface area, which are the topics of the next two chapters.

# 4 Chemical modifications II

## Templated nano-architectures - Heteroatom doped carbon hollow spheres

---

### 4.1 Introduction

**Hollow spheres** of nanometer to micrometer dimensions constitute an important class of materials, possessing high internal volumes, high surface areas, and low density. They are “processable voids” which find use in applications ranging from product delivery (drugs, cosmetics, dyes, and inks) through to light weight composite materials, acoustic insulation, photonic band gap crystals and catalysis.<sup>121-123</sup> Liposomes, for example, are self-assembled lipid bilayer vesicles found in cells and thus naturally occurring “hollow spheres” which allow water soluble molecules to be encapsulated within them. They are commonly used as drug delivery vehicles in cosmetic and medicinal applications.<sup>121</sup> For electronic applications such as electrocatalysis or anode materials for modern batteries, they are less suitable and issues such as material stability and conductivity must be addressed. Artificial hollow structures are therefore a matter of intense research. Hollow spheres and capsules have been synthesized from various materials such as polymers,<sup>124</sup> silica,<sup>125</sup> glass,<sup>126</sup> metals,<sup>127</sup> metal oxides,<sup>128</sup> zeolites<sup>129</sup> and hybrid composites.<sup>130</sup> Carbon hollow spheres (**CHS**) present an interesting addition to these materials owing to properties such as chemical inertness, electrical conductivity and tunable surface chemistry, which makes them especially interesting for catalysis. Various chemical and physicochemical methods are routinely used to synthesize hollow capsules and spheres. These include spray drying processes, self-assembly, emulsion/interfacial polymerization procedures, and sacrificial core (*i.e.* templating) techniques. Here, the template (*e.g.* silica, carbon, or polymeric materials) is coated by the desired material, either by controlled surface precipitation of an inorganic precursor from solution or by direct surface reactions. The core can subsequently be removed either by dissolution or by thermal decomposition.<sup>123</sup> Polystyrene (**PS**) latexes and their derivatives are often used as templating agents because they are mild and easier to handle compared to classical hard templates like silica, which require harsh conditions for removal. PS decomposes upon heat treatment above *ca.* 400 °C (the exact decomposition

temperature depends on the latex) and can thus easily be removed *via* thermolysis. Examples using PS latexes include the work of Caruso *et al.* who used layer-by-layer (**LbL**) assisted deposition of various materials (polymeric, inorganic and metallic) onto PS latex particles with a diameter of 640 nm.<sup>123</sup> Dai *et al.* used sulfonated polystyrene latexes as templates in combination with aniline as the coating material.<sup>124</sup> Niu *et al.* prepared core-shell particles *via* a so-called “inward growth method”, whereby inward sulfonation of PS latex particles allowed preferential adsorption of the aniline precursor that was subsequently polymerized.<sup>131</sup>

Heteroatom doping as a tool to moderate the properties of CHS has been achieved in the case of nitrogen, while sulfur has only really been used for surface modification of CHS in the form of sulfonation. Nitrogen doped CHS have been prepared *via* hard template/chemical vapor deposition approaches (*e.g.* pure silica and SBA-15) of acetonitrile.<sup>37, 132</sup> and *via* pyrolysis of self-assembled poly(aniline-co-pyrrol) hollow microspheres.<sup>133</sup>

In the context of HTC, Titirici *et al.* reported on the generalized synthesis of metal oxide hollow spheres *via* the HTC of glucose in the presence of metals salts.<sup>128</sup> Concerning carbon hollow nanospheres, White *et al.* have recently reported a simple combined HTC / polystyrene latex template approach for the synthesis of CHS, whereby selection of template size was used to control the resulting nanosphere size.<sup>122</sup>

This chapter extends the strategy taken by White *et al.* to produce nitrogen, sulfur as well as

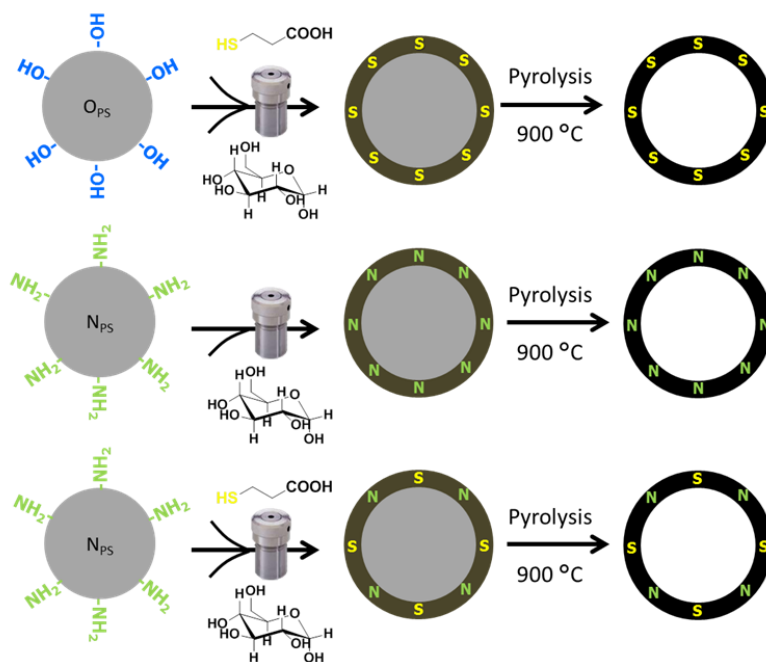


Fig. 4.1 graphical abstract of chapter 4

sulfur and nitrogen dual doped carbon hollow spheres. It is expected that doped carbon hollow spheres exhibit superior properties compared to the pure carbon hollow spheres, such as increased conductivity, stability and catalytic activity (**Fig. 4.1**). As a proof of principle, the doped carbon spheres are assessed in terms of their electrocatalytic activity in the oxygen reduction reaction.

## 4.2 Heteroatom doped carbon hollow spheres

### 4.2.1 Mechanistic considerations

When using latex particles as hard templates in HTC, a prerequisite is that carbonization takes place on the surface of the latex particles, rather than in the bulk solution. The approach taken by White *et al.* was to synthesize a polystyrene nanolatex with hydroxylated poly-ethylene glycol (PEG) terminal groups<sup>122</sup>. The hydroxyl groups on the surface of the particles form suitable hydrogen-bonding partners for the initial adsorption of glucose and various HTC intermediates (see **chapter 2.1**). Once adsorbed, HTC continues and results in a coating of the template by a carbonaceous nanolayer (< 20 nm thickness). After collection of the product by filtration, it is dried *in vacuo* and the template is finally removed by pyrolysis above the latex particle decomposition temperature (generally above 400 °C, depending on the latex). Pyrolysis additionally causes further condensation and graphitization of the hydrothermal carbon framework, so the polystyrene is decomposed (polystyrene cannot carbonize) while the hydrothermal carbon layer becomes more stable. Carbon hollow spheres (CHS) are the final result. In the work presented here, doped CHS were synthesized and used for electrochemical applications. Therefore, a high pyrolysis temperature of 900 °C was chosen in order to achieve template removal and at the same time a sufficiently carbonized material with high conductivity.

In order to achieve doping of the CHS, nitrogen and/or sulfur containing molecules were initially added to the original glucose/latex mixture. Several nitrogen and/or sulfur containing additives were tested (Cys, TCys, TCA and MPA, see **chapter 3**) and it was found that amino containing additives resulted in a destabilization of the latex or formation of non-templated, but still heteroatom doped bulk carbon materials (an example of the product morphology obtained from addition of Cys to a latex/glucose mixture is shown in **Fig. A 4** in the appendix). This indicated that the interaction between glucose and the heteroatom containing additive is undisturbed, but the interaction of the precursors with the latex is hindered. Completely

exchanging glucose with N-acetyl glucosamine, a nitrogen containing precursor used by Zhao *et al.* to obtain nitrogen doped carbons *via* HTC, was also not successful.<sup>46</sup> It was concluded that amino containing additives rapidly react with glucose *via* Maillard reactions and hinder the attachment of glucose to the latex particle surface.<sup>134</sup> Addition of nitrogen containing molecules to the original recipe was therefore not a simple option and an alternative route needed to be found.

### 4.2.2 Synthesis of nitrogen doped CHS *via* reactive templating

As an alternative to doping the hollow spheres by adding the dopant to the latex/glucose mixture, the latex was modified to act as the nitrogen source in a “reactive templating” approach. Styrene and 4-amino-styrene were co-polymerized (using a calorimeter) to give particles with amino-containing surface groups. The amino surface groups have the same function as the aforementioned hydroxyl terminated latex, namely to interact with the HTC precursor, glucose and essentially adsorb it to the particle surface (*i.e. via* Maillard reaction chemistry). The nitrogen is thereby covalently incorporated into the hydrothermal carbon during the carbonization process, allowing for nitrogen retained upon removal of the template. The nitrogen content can be adjusted by increasing the amount of 4-amino styrene in the polymerization process (data not shown). Only the sample that gave the best results during electrochemical testing will be discussed here, namely nitrogen doped CHS template by a latex made from copolymerization of 10 wt % of 4-amino styrene (with respect to styrene), stabilized with the anionic surfactant 4-dodecylbenzenesulfonic acid (**SDBS**). The latex is referred to as **N<sub>ps</sub>\_latex** from hereon. To obtain nitrogen doped CHS, HTC of 0.8 g glucose in a 5 wt % solution of the corresponding amino-functionalized latex (10 ml) was carried out at 180 °C for 18 h. After template removal *via* pyrolysis of the dried sample at 900 °C, the sample was labeled **N-CHS\_900**.

### 4.2.3 Synthesis of sulfur doped CHS *via* the addition of MPA

Successful results for sulfur doping could be obtained by addition of 3-mercapto-propanoic acid (**MPA**) to the original HTC/latex recipe used by White *et al.* (using hydroxyl-terminated polystyrene particles stabilized by SDS, denoted as **O<sub>ps</sub>\_latex**). Unlike for nitrogen-containing additives, thiol is assumed to react rather slowly with HTC intermediated due to a hard/soft

mismatch between electrophile (carbonyl functionalities in HTC intermediates) and nucleophile (thiol). Also, sulfur is less electronegative than oxygen, so the S-H bond is not as polarized as the O-H bond, making S-H a weaker hydrogen bonding donor. Adsorption of the HTC intermediates therefore presumably takes place before MPA is incorporated into the hydrothermal carbon layer. 0.1 g MPA and 0.8 g glucose were hydrothermally treated at 180 °C for 18 h in 10 ml of a 5 wt % latex solution. Template removal occurred *via* pyrolysis at 900 °C. A reference experiment without the addition of MPA was carried out for direct comparison of the sulfur doped CHS with non-doped CHS, labeled **S-CHS\_900** and **C-CHS\_900**, respectively.

#### 4.2.4 Synthesis of sulfur and nitrogen dual doped CHS

Sulfur and nitrogen dual doped hollow carbon spheres could be obtained by combining the two synthesis approaches, *i.e.* by adding MPA to an N<sub>ps</sub>\_latex /glucose mixture. After template removal at 900 °C, the sample was labeled **SN-CHS\_900**.

#### 4.2.5 Morphology, chemical composition and textural properties of the heteroatom doped CHS

Successful doping of the CHS was confirmed by elemental analysis (**Table 4.1**). The nitrogen doping levels range from 1.3 wt % in N-CHS\_900 to 1.6 wt % in SN-CHS\_900 and the sulfur doping levels range from 1.7 wt % in SN-CHS\_900 to 2.5 wt % in S-CHS\_900. As is expected for such high pyrolysis temperatures, the materials all have high carbon contents of > 90 wt % as well as low hydrogen contents due to dehydration, decarboxylation and aromatization during

**Table 4.1 Elemental composition of the bulk and surface of the heteroatom doped CHS after template removal at 900 °C, determined by elemental analysis. [NB: N<sub>2</sub> sorption-derived textural and electrical conductivity properties of the presented materials are shown on the right].**

Sample	Elemental composition (wt %)				Textural properties				
	C	H	N	S	S <sub>BET</sub> m <sup>2</sup> g <sup>-1</sup>	V <sub>total</sub> cm <sup>3</sup> g <sup>-1</sup>	D <sub>i</sub> nm	D <sub>s</sub> nm	σ Sm <sup>-1</sup>
C-CHS_900	96.1	1.1	-	-	435	0.37	105	14	668
N-CHS_900	91.2	1.4	1.3	-	357	0.41	66	14	600
S-CHS_900	94.4	1.0	-	2.5	378	0.30	165	16	637
SN-CHS_900	92.1	0.9	1.6	1.7	329	0.25	54	11	673

D<sub>i</sub> = average inner diameter of the CHS as determined from TEM images

D<sub>s</sub> = average shell thickness of the CHS as determined from TEM images

σ = specific conductivity as determined by impedance spectroscopy

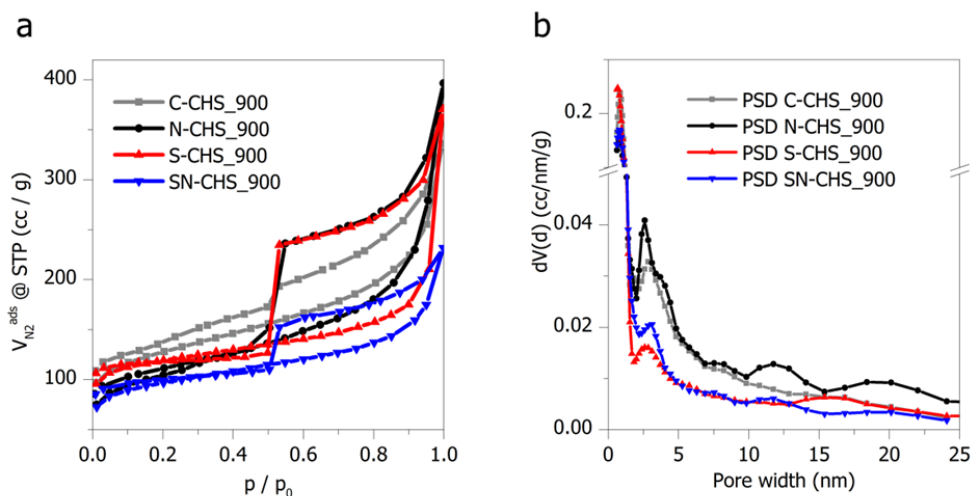


**Fig. 4.2 a)** Nitrogen sorption isotherms of nitrogen doped CHS after template removal at 900 °C. **b)** Corresponding pore size distributions determined by the QSDFT model (adsorption branch).

heat treatment. This also gives rise to high specific conductivity values which are shown in the last column of **Table 4.1**. Conductivity is a crucial property for electrochemical applications. Nitrogen sorption shows type IV H2 isotherms for all samples, indicative of “ink bottle” shaped pores, *i.e.* wide pore bodies with narrow necks (**Fig. 4.2**).<sup>135-137</sup> One interpretation could be the filling of large hollow sphere cavities through small micropores in the CHS shells. Before template removal, the BET surface areas of the materials were in the typical range observed for solid hydrothermal carbon spheres ( $\sim 20\text{--}40\text{ cm}^3\text{ g}^{-1}$ , data not shown.). The clear hysteresis is indicative of the presence of mesopores which are defined to be in the range of 2 nm to 50 nm.<sup>135</sup> As part of the hollow spheres have average inner diameters ( $D_i$ ) of greater than 50 nm, the sphere cavities are unlikely to be the sole cause for the hysteresis seen in nitrogen sorption. It is likely the interstitial voids that occur due to the aggregation of the spheres, as well as compression and deformation of the hollow spheres play a role in the formation of mesopores. The pore size distributions obtained from nitrogen sorption using a quenched solid density functional theory (QSDFT) model (the adsorption branch was used for analysis) do not indicate a large number of mesopores and were thus interpreted to not be a realistic representation of the studied system. Hence, values such as micro and mesopore volume derived from QSDFT modeling of the sorption data are not reported here.



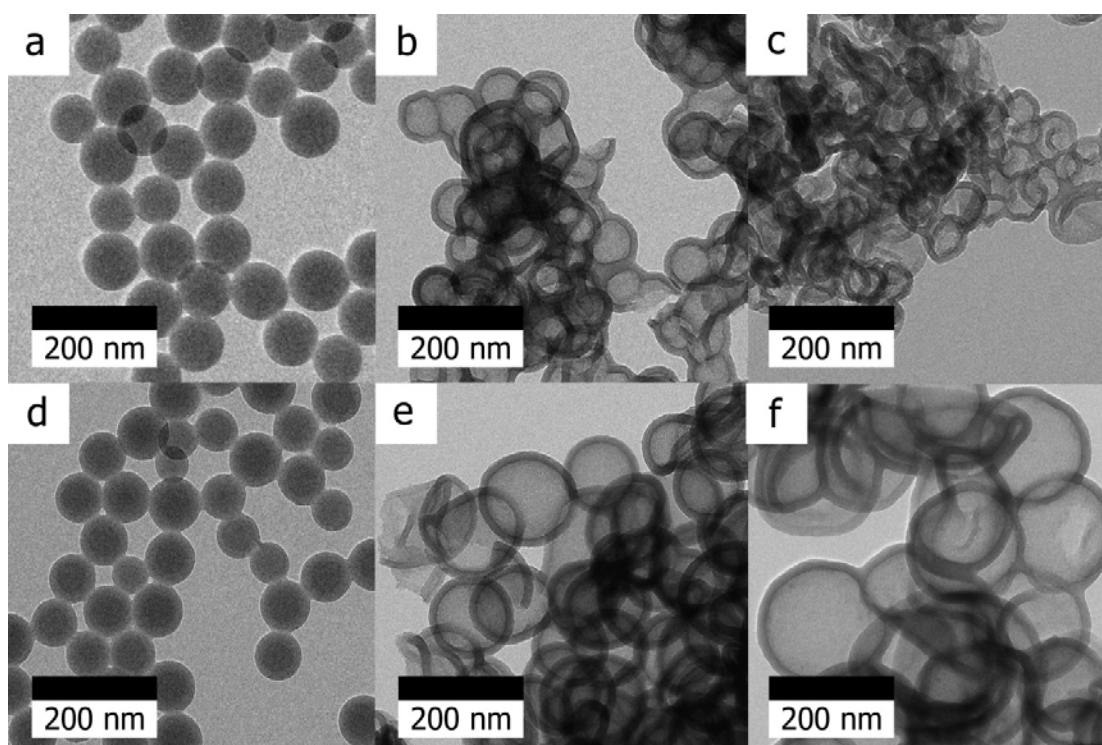


**Fig. 4.3** a)  $N_{ps\_latex}$ , b) N-CHS\_900, c) SN-CHS\_900 d)  $O_{ps\_latexC}$ , e) C-CHS\_900 and f) S-CHS\_900

The first row of **Fig. 4.3** shows transmission electron microscopy (**TEM**) images of a)  $N_{ps\_latex}$  and the resulting samples b) N-CHS\_900 and c) SN-CHS\_900. The second row shows TEM images of d)  $O_{ps\_latexC}$  and the resulting samples e) C-CHS\_900 and f) S-CHS\_900. The average diameters of the latex particle templates are similar, namely 79 nm and 77 nm for  $N_{ps\_latex}$  and  $O_{ps\_latexC}$ , respectively. N-CHS\_900 and SN-CHS\_900 exhibit inner diameters which correlate well with the corresponding latex template. The decreased  $D_i$  of the CHS are most likely due to contraction of the carbon shell during the carbonization process (**Table 4.1**). On the other hand, the samples obtained from using  $O_{ps\_latexC}$  as a template have  $D_i$  considerably larger than the template diameter. C-CHS\_900 has  $D_i$  of 105 nm and S-CHS\_900 has even larger  $D_i$  of 165 nm. This effect was partially attributed to the fact that glucose and the resulting HTC intermediates are presumably less tightly bound to the surface of the hydroxyl-terminated latex particles (*i.e. via* non-covalent interactions such as hydrogen bonds) than the amino-terminated latex particles (covalent bonds arising from Maillard interactions). For S-CHS\_900 however the size increase is very large and must additionally be due to swelling of the latex particles themselves.

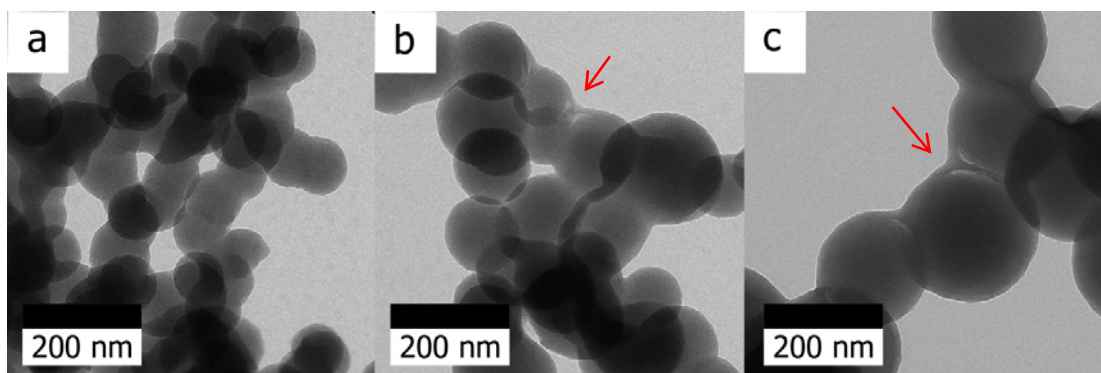


Fig. 4.4 TEM images of a) N-CHS, b) C-CHS and c) S-CHS after HTC at 180 °C prior to pyrolysis.

TEM images of all samples recorded after HTC but prior to template removal confirm this hypothesis: N-CHS latex spheres are well coated and no disruption between hydrothermal carbon layer and template could be observed (**Fig. 4.4a**). For C-CHS and S-CHS several locations where the hydrothermal carbon layer is “peeled” from the particles could be observed (marked by red arrows in **Fig. 4.4b and c**). The image of S-CHS additionally shows that the latex particle has increased in size compared to C-CHS. Swelling of sulfur containing polystyrene latexes has been observed by other groups.<sup>124, 131, 138</sup> In those cases, sulfonation of the polystyrene core renders the particle hydrophilic, allowing water to enter the core and cause swelling. Here, the swelling is induced by the addition of MPA which is, however, unlikely to cause sulfonation of the polystyrene core. Control experiments, namely HTC of pure  $O_{ps\_latex}$  in water and  $O_{ps\_latex}$  with MPA in water were carried out to further investigate the cause of particle increase. Surprisingly, the latex remained stable after hydrothermal treatments in both cases and no swelling was observed by TEM (**Fig. A 5 in the appendix**). The conclusion from this was that swelling of the latex is not due to the presence of MPA on its own, but most likely due to some species formed from the reaction of MPA with glucose. This effect however seems to be dependent on the type of latex since no swelling was observed if  $N_{ps\_latex}$  was used.

High resolution transmission electron microscopy (**HRTEM**) images of the heteroatom doped CHS all show the disordered graphitic layers that are typical for heteroatom doped carbons (**Fig. 4.5**).<sup>38, 63, 117</sup> The disorder is thought to arise from packing defects due to the presence of dopants. X-Ray diffraction (**XRD**) performed on the same samples gives rise to two main peaks at *ca.* 22.2 ° and *ca.* 43.7 °, corresponding to the 002 and 100 lattice spacings of graphite, respectively (**Fig. A 6 in the appendix**).<sup>116</sup> The large shift towards smaller angles is due to an

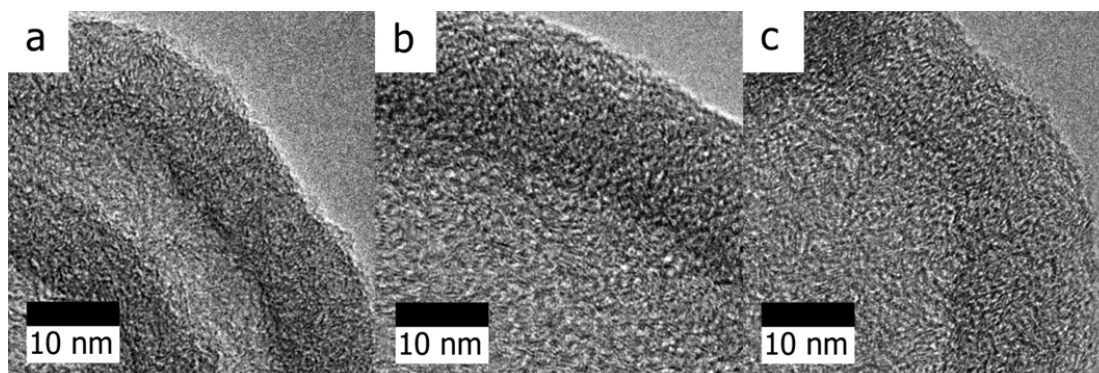


Fig. 4.5 HRTEM images of a) N-CHS\_900, b) S-CHS\_900 and c) SN-CHS\_900.

increased interlayer spacing arising from the presence of nitrogen and/or sulfur which are both large compared to carbon.<sup>38, 117</sup>

## 4.2.6 Electrochemical characterization of doped CHS

The heteroatom doped CHS were tested for their oxygen reduction reaction (ORR) related electrocatalytic activity (refer to **chapter 2.2** for details about ORR). Two main points were investigated:

- Whether doped CHS exhibit **superior catalytic activity** than undoped CHS
- The effect of the **type of heteroatom** on the electrocatalytic activity of the doped CHS

Cyclic voltammetry (CV) and linear sweep voltammetry (LSV) using a rotating disk electrode (RDS) were carried out in 0.1 M KOH. Featureless voltammetric curves were obtained in N<sub>2</sub>-saturated solution. A cathodic peak signal is observed for the cyclovoltammograms in O<sub>2</sub>-saturated solution, indicating the activity of the material towards oxygen reduction (**Fig. 4.6a**). **Fig. 4.6b** shows the polarization curves obtained by LSV with an RDE at 1600 rpm in O<sub>2</sub>-saturated 0.1 M KOH. Data for undoped CHS (C-CHS\_900, dashed red line), for **Vulcan**, a commercially available carbon support (dashed black line), and for a 20 wt % platinum catalyst supported on Vulcan (**Pt@C**, dashed grey line), are shown for reference. C-CHS\_900 and S-CHS\_900 shows an improved onset potentials (-185 mV *vs* Ag/AgCl) over N-CHS\_900 (-207 mV *vs* Ag/AgCl).

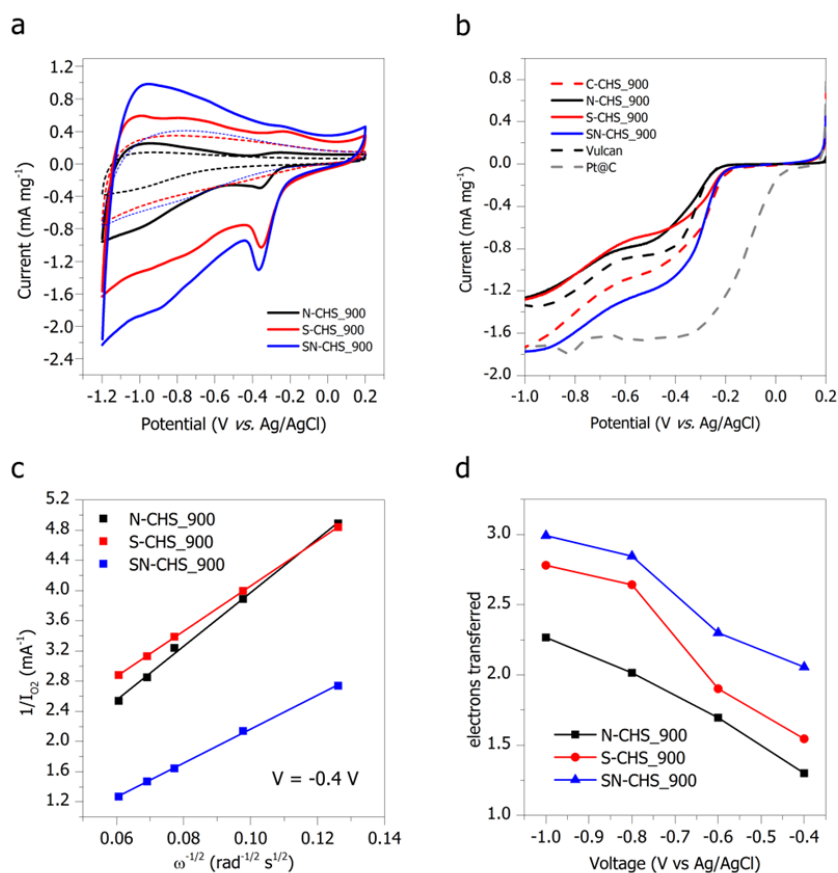


**Fig. 4.6** A comparison of electrochemical properties of heteroatom doped CHS. a) cyclic voltammograms in N<sub>2</sub>-saturated (dashed lines) and O<sub>2</sub>-saturated (solid lines) 0.1 M KOH. b) polarization curves taken at 1600 rpm in O<sub>2</sub>-saturated 0.1 M KOH. Data for undoped CHS (dashed red line), Vulcan carbon (dashed black line) and a platinum catalyst supported on Vulcan (dashed grey line) are shown for reference. c) Koutecky-Levich plots for V = -0.4 V, d) electron transfer numbers at various voltages.

In terms of maximum current density, the solely nitrogen or sulfur doped samples exhibit worse electrocatalytic performance than the undoped sample. There are several possible explanations for this. Firstly, the doping levels are generally very low in the order of 1 wt % which may not be sufficient to influence the catalytic properties of the doped CHS. Secondly, the surface area and morphology of the materials play an important role during electrocatalysis.<sup>139</sup> Good mass transport is required which will be affected by the CHS size and whether they are intact or broken, as well as the sizes of the interstitial voids. Generally speaking, CHS do not exhibit an optimal morphology for the use as ORR catalysts because the interior voids cannot easily be accessed by the electrolyte (only through the micropores in the CHS walls where mass transport is slow).<sup>139</sup> This means that the inner CHS surfaces are not well accessible active sites. As seen in

**Table 4.1** C-CHS\_900 indeed exhibits the highest surface area out of the samples tested which may be the reason for the improved performance over the sulfur or nitrogen doped CHS. However, SN-CHS\_900 has the lowest surface area out of the samples yet exhibits the best catalytic performance. The onset potential is similar to C-CHS\_900 and S-CHS\_900, but the maximum current density is significantly increased over the entire potential range. This indicates that the combined doping of CHS with sulfur and nitrogen has dramatic effects on the material properties. Koutecky-Levich plots taken at  $V = -0.4 \text{ V vs. Ag/AgCl}$  for the doped samples show good linearity (**Fig. 4.6c**). A plot of the electron transfer number (which is determined using the slope of the Koutecky-Levich plot at a given voltage) at various voltages shows that the reduction mechanism tends towards larger electron transfer numbers with decreasing voltages (**Fig. 4.6d**). None of the samples show good selectivity for either the 2 or the 4 electron process but it rather seems as if a mixture of the two processes is occurring.

### 4.3 Summary of chapter 4

The synthesis of nitrogen and/or sulfur doped carbon hollow spheres with nano-dimensions was demonstrated. It was shown that although the doping levels were low (1.3 to 2.5 wt %), the material properties could significantly be influenced, especially when CHS were doped simultaneously with sulfur and nitrogen. In terms of electrochemical testing, the sensitive interplay between the material's physicochemical (elemental composition, conductivity) and textural (surface area and morphology) properties was demonstrated. The benefits of higher surface area of undoped CHS outweighed low doping levels for solely nitrogen or sulfur doped CHS. However, dual S/N doped CHS exhibited the best catalytic performance in the oxygen reduction reaction in alkaline medium despite having the lowest surface area out of all tested samples. A similar phenomenon, *i.e.* that dual doped carbons show enhance catalytic performance over singly doped carbons, was observed for sulfur and nitrogen dual doped carbon aerogels, which are the topic of the next chapter. A more detailed electrochemical analysis is therein given and a tentative synergistic mechanism between sulfur and nitrogen is proposed. At this point it is merely important to keep in mind that sulfur as a dopant clearly imposes different properties on the carbon material than nitrogen, and doping carbon with both heteroatoms simultaneously results in yet different properties.

# 5 Chemical Modifications III

## Template-free nano-architectures - Heteroatom doped organic and carbon aerogels

---

### 5.1 Introduction

The previous chapter focused on the synthesis of doped carbon hollow spheres *via* a hard templating method. Returning to the 12 principles of chemistry, one criterion now comes to mind:<sup>40</sup>

**2. Atom Economy** - Synthetic methods should be designed to maximize the incorporation of all materials used in the process into the final product.

While the latex templating method in **chapter 4** is very mild compared to hard templating with, *e.g.* silica, template-free methods are still preferable.

**Aerogels** are a class of materials with defined nano-architectures that find applications in thermal and acoustic insulation, sorption, catalysis, chromatography and as electrode materials.<sup>140-142</sup> In simple terms, they are gels in which the liquid component has been replaced by air. Consequently, they are extremely light weight materials containing many voids within a continuous solid matrix which allows for excellent mass transport and good thermal insulation.<sup>140, 143</sup> The first reported aerogels (in 1931) were made of silica and thus represent the most studied materials in this class of materials.<sup>144</sup> Silica aerogels currently hold several entries in Guinness World records for material properties, including best insulator and low-density solids. **Carbon aerogels** (CA) were first introduced by Pekala in 1989 and nicely complement their inorganic counterparts owing to properties such as chemical inertness and electrical conductivity.<sup>145</sup> This makes them very attractive candidates for electrode materials or catalyst supports. Aerogels have also been prepared from metal oxides, alumina or chalcogens.<sup>142, 146</sup>

Aerogels are typically prepared *via* sol-gel methods, whereby particles in a colloidal suspension undergo condensation reactions until all particles in the sol are interlinked into a gel. Because this process is generally slow, acid or base catalysis is often used. Depending on the solute to

solvent ratio, as well as the pH of the reaction, the particle size may be tuned. Resorcinol-formaldehyde (**RF**) aerogels are prepared in a similar fashion.<sup>145</sup> The resulting aerogels still contain abundant oxygen functionalities are therefore classified as “**organic aerogels**”. They may be converted into “**carbon aerogels**” *via* pyrolysis, which (depending on the graphitizability of the precursor) results in higher electrical conductivity and therefore opens the door for electronic applications.<sup>141</sup>

Due to the high porosity of aerogels, special precautions are required during the drying of the material. **Supercritical drying** with CO<sub>2</sub> is commonly carried out in order to avoid collapsing of the solid matrix due to capillary forces, which normally occurs if the aerogel is dried under vacuum. The supercritical drying procedure is what distinguishes aerogels from the related xerogels (dried under vacuum) and cryogels (freeze-dried), which tend to have more condensed solid frameworks and lower surface areas.<sup>140</sup>

The RF system introduced by Pekala is still the most common route towards organic and carbon aerogels. Nitrogen doped aerogels have been prepared by slight modifications of the RF system, *e.g.* using melamine-formaldehyde.<sup>147, 148</sup> The drawbacks of these synthesis approaches however lie in the limited availability of the precursors and their potential harm to health and environment.

Hydrothermal carbonization (HTC) currently offers two alternative and more sustainable routes towards organic and carbon aerogels, each with its own advantages and drawbacks:

**1) Albumin-directed hydrothermal carbonization of glucose**<sup>63</sup>

This approach developed by White *et al.* uses the glycoprotein ovalbumin as a structure directing agent and as a nitrogen source. All reagents are part of the final structure. Unlike the borax system, it therefore adheres completely to the criterion of atom economy stated above. However, tuning of the particle size is not possible. This method inherently gives rise to nitrogen doped organic aerogels.

**2) Borax-mediated hydrothermal carbonization of glucose**<sup>52, 149</sup>

This approach developed by Feller *et al.* uses borax as a catalyst and stabilizing agent in the gel formation. While borax needs to be washed out after the carbonization process, it can in principal be recovered and re-used. The great advantage of this method is that the particle size of the gels can be controlled by varying the amount of borax added. No reports on the doping of these aerogels with nitrogen or sulfur currently exist.

This chapter focuses on the synthesis of sulfur and nitrogen dual doped carbon aerogels, based on method 1) in the first section, and the synthesis of sulfur and/or nitrogen doped carbon aerogels, based on method 2) in the second section. The incorporation of heteroatoms into the HTC-derived organic/carbon aerogels is expected to greatly increase the breadth of potential applications. To demonstrate this, the aerogels are used as non-metal electrocatalysts in the oxygen reduction reaction of fuel cells.

## 5.2 Sulfur and nitrogen doped organic/carbon aerogels *via* the albumin-directed HTC of glucose

### 5.2.1 Introduction

The hydrothermal carbonization (HTC) of pure glucose at  $T = 180 - 200$  °C, typically yields amorphous, non-porous carbon microspheres composed of a largely polyfuranic framework and abundant surface oxygen functional groups (*e.g.* hydroxyl, carboxylic acid, lactones *etc.*).<sup>4, 6, 8, 51, 150</sup> A simplified reaction mechanism involves the initial dehydration of glucose to hydroxymethylfurfural and other intermediates and their subsequent polymerization. When nitrogen containing molecules are present, such as ovalbumin, Maillard reactions can take place (refer to **chapter 2.1** for more details). White *et al.* observed the formation of a monolithic gel after HTC of glucose in the presence of ovalbumin at 180 °C for 5.5 h.<sup>63</sup> Further analysis of their material revealed a highly porous, three-dimensionally ordered structure, a morphology very atypical of HTC without the presence of templates. Due to the presence of albumin, the organic aerogel contained  $\sim 7$  wt % nitrogen and a surface area of  $\sim 250$  m<sup>2</sup> g<sup>-1</sup>.

This all-sustainable synthesis of a hierarchically ordered material was used a starting point for

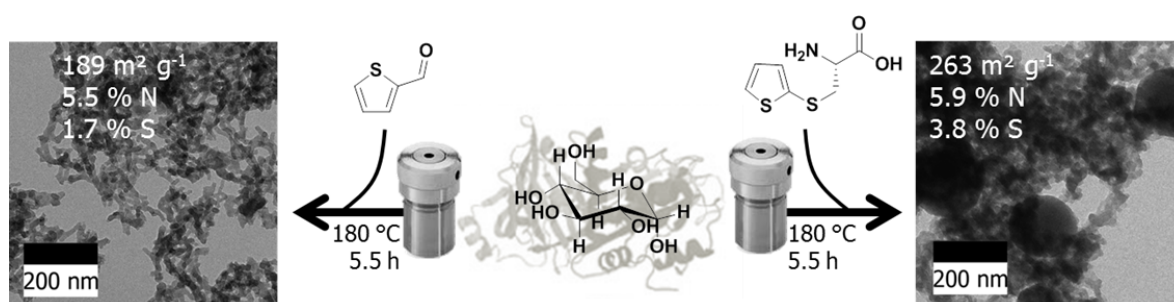


Fig. 5.1 graphical abstract of chapter 5.2



further chemical modification. In order to broaden the potential of the nitrogen doped organic aerogels for a wide range of applications, the incorporation of sulfur in addition to nitrogen was investigated (**Fig. 5.1**).

## 5.2.2 Mechanistic considerations

While the albumin-directed carbon aerogel formation is practically simple to carry out, it is mechanistically complex and easily disturbed by the addition of further reactants. The interplay between protein and saccharide is not well understood, making the use of additional molecules for doping non-trivial. One explanation given by White *et al.* is that the protein and associated Maillard products act as surface stabilizing/structure directing agents for the formation of flexible heteroatom-doped carbon scaffolds.<sup>63</sup> It is further assumed that part of the gelation process involves the crosslinking (*via* Maillard reactions) of forming hydrothermal particles by ovalbumin-derived amino groups, whereby the amino groups may arise from the free amine containing side chains of the protein or *via* the hydrolysis of peptide linkages during hydrothermal treatment. A highly simplified theory is that gel formation is hindered if the molecule added to the glucose/albumin system competes with this crosslinking process. Nucleophiles such as free amines or thiols are therefore not suited as dopant sources. Hydroxymethylfurfural (HMF) is a key intermediate of the glucose HTC mechanism.<sup>4, 6, 51</sup> The mechanistic discussion in **chapter 2.1** showed that HMF can undergo various reactions, such as nucleophilic addition, electrophilic aromatic substitution and cycloaddition. It is assumed that reactions that do not interfere with the nucleophilic attack of the protein-derived amino groups (*i.e.* electrophilic aromatic substitution or cycloaddition) can be exploited for the incorporation of heteroatoms without preventing gel formation. To test this hypothesis, three different sulfur sources, L-cysteine (CS), S-(2-thienyl)-L-cysteine (TC) and 2-thienyl-carboxaldehyde (TCA), were added to the original carbon aerogel recipe.<sup>63</sup> The nucleophilic sites are marked in red and the sites capable of electrophilic aromatic substitution or cycloaddition in blue (**Fig. 5.2**).

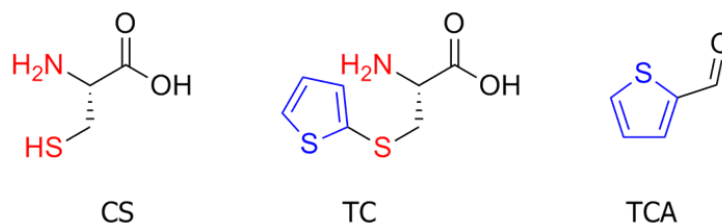


**Fig. 5.2** Structures of additives tested as sulfur source in the HTC of glucose and albumin.

### 5.2.3 Sulfur and nitrogen doped organic aerogels

L-cysteine (CS), an amino acid, was the initial choice for the sulfur source due to its environmentally benign nature and low cost. However, experiments using CS as the sulfur source resulted in micrometer sized spherical particles, very similar to those obtained when glucose is hydrothermally treated with cysteine without ovalbumin (see **chapter 3**), as well as condensed gel-like structures (**Fig. A 7 in appendix**). The BET surface area of this material was  $56 \text{ m}^2 \text{ g}^{-1}$ , which is only slightly higher than the typical value for classical hydrothermal carbon spheres ( $\sim 30 \text{ m}^2 \text{ g}^{-1}$ ). Because the obtained product had neither defined structure nor high surface area, CS was not further used as a dopant molecule.

In contrast, experiments with S-(2-thienyl)-L-cysteine (TC) and 2-thienyl-carboxaldehyde (TCA) resulted in successful monolith formation. The as-synthesized aerogels were dried in supercritical  $\text{CO}_2$  in order to preserve as high as possible the metastable hydrogel state and avoid capillary force-induced collapse of the three-dimensionally ordered nano-architectures.<sup>140</sup> Comparatively freeze drying is a more convenient option, but usually results in lower surface areas. The samples were labeled **CA-TC** and **CA-TCA** for TC and TCA containing aerogels, respectively. A

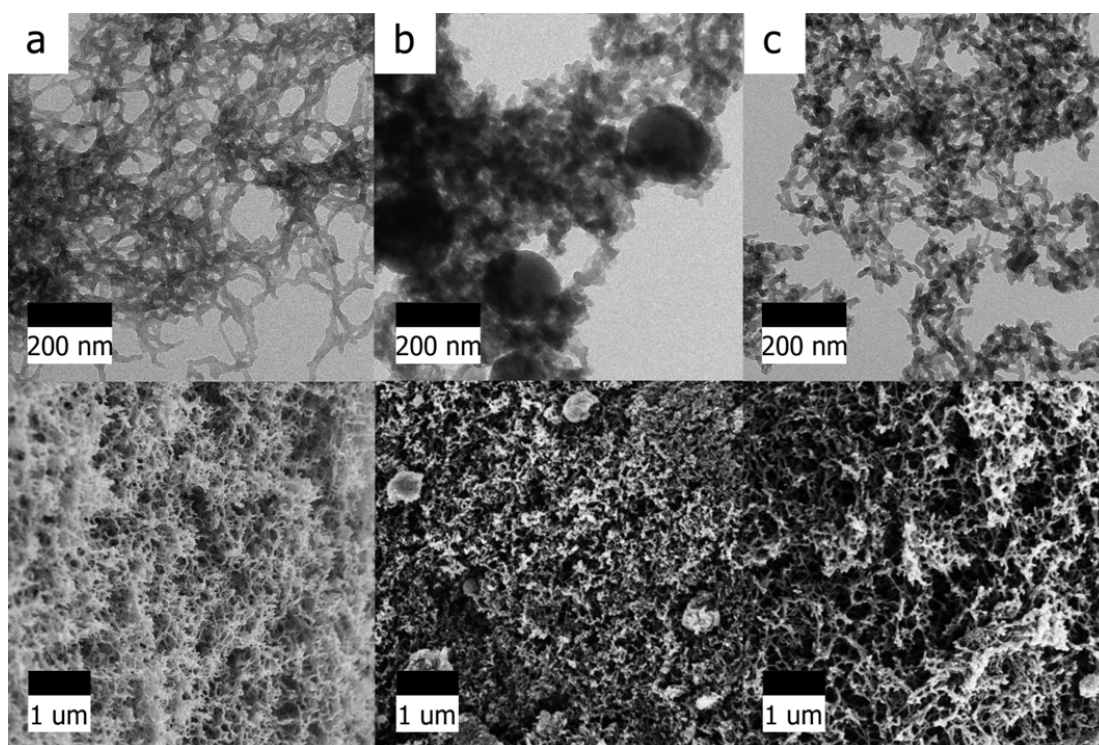
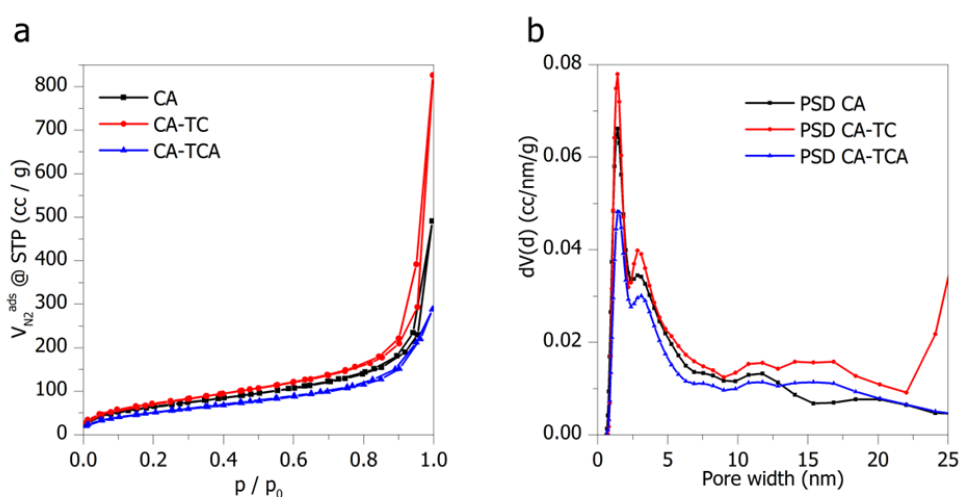


Fig. 5.3 TEM (top) and SEM (bottom) images of a) CA; b) CA-TC; c) CA-TCA

reference aerogel synthesized according the original recipe from White *et al.* was labeled **CA**.<sup>63</sup> Transmission electron microscopy (**TEM**) images show that the morphologies obtained for the sulfur doped aerogels depend on which additive/co-monomer is used. Addition of TC gives rise to larger spherical particles (*ca.*  $D = 200$  nm) which are linked to a smaller particle matrix (**Fig. 5.3b**). Addition of TCA results in a homogeneous interconnected particle matrix only, and the morphology is similar to that seen for the original nitrogen-doped CA (**Fig. 5.3c and a**, respectively). The difference in morphology of CA-TC is attributed to heterogeneous nucleation and structure formation, in accordance with the LaMer model.<sup>102</sup> Considering the presented hypothesis, simultaneous crosslinking and particle formation are expected to take place, arising from the presence of both nucleophilic and electrophilic aromatic substitution/cycloaddition-capable sites in TC. The amino groups compete with those of the hydrolyzed protein, but clearly not to the extent of complete crosslinking inhibition. A hybrid morphology between discrete particles and an interconnected particle matrix is the result. With TCA, the incorporation of sulfur presumably takes place exclusively *via* electrophilic aromatic substitution/cycloaddition and crosslinking can proceed unhindered.

Nitrogen sorption data are in good agreement with the TEM observations. The sulfur and nitrogen doped carbon aerogels after HTC at 180 °C exhibit Type IV/H3 reversible sorption isotherms with limited hysteresis loop profiles.<sup>63, 135</sup> The lack of an adsorption plateau at high relative pressures as well as the broad pore size distribution for all samples are indicative of slit shaped pores in an open pore system (**Fig. 5.4**).<sup>63</sup> These results are similar to those described for



**Fig. 5.4** a) Nitrogen sorption isotherms and b) pore size distributions (QSDFT model) obtained for aerogels after HTC at 180 °C.

CA by White *et al.*, although in the case of CA-TCA the BET surface area is lower than in CA and in CA-TC (**Table 5.1**).<sup>63</sup> The large increase in the nitrogen volume adsorbed as  $p/p_0$  approaches unity, particularly for CA-TC is attributed to the condensation of adsorbate in large mesopores or (very small) macropores within the continuous coral-like material architecture. CA-TC has the largest mesopore volume among the three samples ( $0.46 \text{ cm}^3 \text{ g}^{-1}$ , *c.f.*  $\sim 0.30 \text{ cm}^3 \text{ g}^{-1}$  for CA and CA-TCA), a result of the observed change in material morphology with precursor chemistry. This is also reflected in the pore size distributions of the samples (**Fig. 5.4b**). Whilst pore size distributions show that volume levels off after a pore width of *ca.* 20 nm for CA and CA-TCA, that of CA-TC shows a secondary increase towards still larger pores.

The simultaneous incorporation of nitrogen and sulfur into the HTC-derived carbons was confirmed by elemental analysis and X-ray Photoelectron Spectroscopy (**XPS**) (**Table 5.1**). The carbon content is slightly increased for the nitrogen and sulfur containing carbon aerogels. The additional nitrogen in the co-monomer TC does not influence the final nitrogen content of CA-TC (5.9 wt %) compared to CA-TCA (5.5 wt %) significantly, indicating that the predominant source of the nitrogen is the protein. Notably CA-TC contains more than twice the amount of sulfur than CA-TCA (3.8 wt % for CA-TC compared to 1.7 wt % for CA-TCA). The S/N ratios are similar for (surface) XPS but vary greatly when compared to the (bulk) elemental analysis data. For the presented HTC aerogels prepared at 180 °C, the elemental analysis-derived S/N ratios typically exceed the XPS-derived ones. Such deviations are very typical and are related to the fact that elemental analysis detects all sulfur atoms, while XPS is a surface sensitive technique and therefore reflects surface enrichment of functional groups. The bulk/surface ratio of sulfur, given by  $\text{sulfur}_{\text{EA}}/\text{sulfur}_{\text{XPS}}$  for CA-TC (2.39) is much higher than for CA-TCA (1.55). On the

**Table 5.1 Elemental composition of the bulk and surface of the organic aerogels after HTC at 180 °C, determined by elemental analysis and XPS, respectively. [NB: N<sub>2</sub> sorption-derived properties of the presented materials are shown on the right].**

Sample	Elemental composition by EA (wt %) and XPS (at %)					Textural properties			
	C	H	N	S	S/N	S <sub>BET</sub> m <sup>2</sup> g <sup>-1</sup>	V <sub>total</sub> cm <sup>3</sup> g <sup>-1</sup>	V <sub>meso</sub> cm <sup>3</sup> g <sup>-1</sup>	V <sub>micro</sub> cm <sup>3</sup> g <sup>-1</sup>
CA	61.8	5.5	5.9	1.1	0.2	239	0.34	0.28	0.06
	72.3	-	6.8	0.5	0.1				
CA-TC	59.8	5.4	5.9	3.8	0.7	263	0.52	0.46	0.06
	73.4	-	5.4	1.6	0.3				
CA-TCA	58.4	5.3	5.5	1.7	0.3	189	0.33	0.29	0.04
	74.2	-	4.6	1.1	0.2				

other hand, the bulk/surface ratios of nitrogen, given by  $\text{nitrogen}_{\text{EA}}/\text{nitrogen}_{\text{XPS}}$ , are similar (1.1 for CA-TC and 1.2 for CA-TCA) and much closer to unity, indicating the absence of surface depletion or enrichment. Hence, CA-TC contains the majority of sulfur atoms in the bulk while the bulk and surface sulfur species in CA-TCA are more balanced. It is very possible that some of the sulfur species in CA-TC are trapped within the species of larger particles, since this morphological feature is coupled to the presence of this sulfur source. In contrast, CA-TCA exhibits a uniform morphology and all the sulfur atoms are therefore better dispersed throughout the gel matrix. A large proportion of surface sulfur implies catalytically accessible sites, while bulk sulfur can contribute only indirectly by the altered electronic properties of carbon. Interestingly, also CA contains minor amounts of sulfur, arising from the cysteine moieties of ovalbumin.<sup>100</sup> Cysteine however cannot undergo cyclo-addition with HTC intermediates and is therefore only weakly incorporated within the carbon framework. The predominant species in this case are aliphatic thiol or oxidized sulfur groups (as was observed for sulfur doped materials derived from cysteine in **chapter 3**).

#### **5.2.4 The conversion of organic aerogels into conductive carbon aerogels *via* pyrolysis**

Overall, all CA, CA-TC and CA-TCA exhibit promising structures and compositions for catalytic applications, such as high surface areas, large diameter, continuous 3-dimensionally arranged porous morphologies (and hence good mass transfer properties) leading accessible dopant sites. However, the amorphous nature of hydrothermal carbon directly after HTC at 180 °C has the drawback of a rather low electrical conductivity. In order to convert the “organic aerogels” into conductive “carbon aerogels” which are suitable for electrocatalytic applications, a pyrolysis step at 900 °C was added to the synthesis process.

Following this temperature treatment, X-Ray diffraction (**XRD**) shows two main peaks for the pyrolyzed carbon aerogels (**Fig. A 8 in appendix**). The peaks at around 22 °-23 ° and at 43.5 ° are the equivalents of the hexagonal graphite 002 ( $2\Theta = 26^\circ$ ) and 100 ( $2\Theta = 43^\circ$ ) reflections, respectively.<sup>116</sup> However, the large shift towards smaller angles for the 002 reflection implies a significant increase in the interlayer spacing. The shift is more pronounced for the sulfur containing samples (22.5 ° for CA-TC\_900 and CA-TCA\_900 compared to 23.1 ° for CA\_900), and can be directly related to the much larger size of the sulfur atom, as compared to carbon or

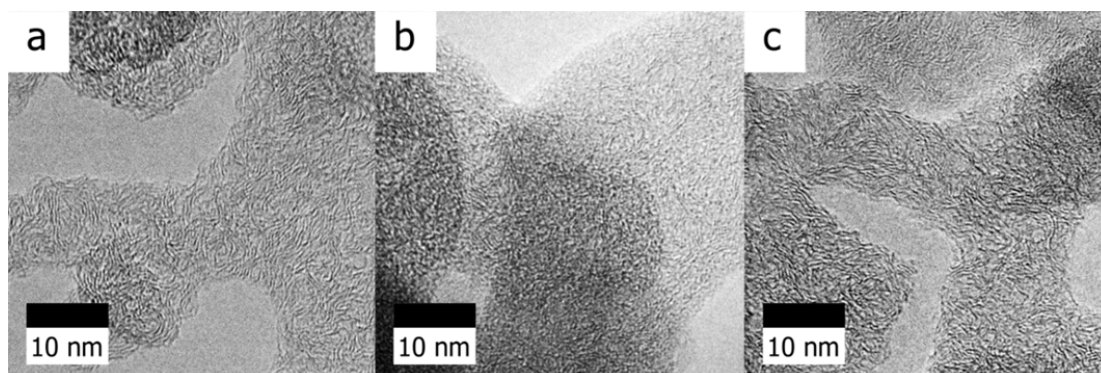


Fig. 5.5 HRTEM images of a) CA\_900; b) CA-TC\_900 and c) CA-TCA\_900

nitrogen.<sup>38, 117, 151</sup> This heat treatment leads to the specific conductivity values for the pyrolyzed aerogels increasing in the order CA\_900 < CA-TCA\_900 < CA-TC\_900, *i.e.* sulfur doped carbons are better electronic conductors (**Table 5.2**). TEM images show that the promising continuous 3-dimensional architecture is nicely retained after pyrolysis, whereby a slight contraction of the interconnected particle matrix occurs due to the further condensation and graphitization of the carbon framework (**Fig. A 9 in appendix**).

High resolution TEM (**HRTEM**) images show disordered, highly bent graphitic layers, typical of doped carbon materials (**Fig. 5.5**).<sup>38, 63, 117</sup> These defects may be beneficial for catalytic activity due to facilitated chemisorption of reactants at the sterically less hindered active sites.<sup>83</sup>

The nitrogen sorption isotherms of the pyrolyzed aerogels exhibit the same type IV/H3 profile as the as-synthesized aerogels (**Fig. A 10a in appendix**), but with a slightly more pronounced hysteresis feature, indicating more (mesoporous) cavities in the more rigid carbon structure; presumably the result of overall dimensional shrinkage and the number of mesopores in the lower “meso” diameter region. The aerogel surface areas increase upon pyrolysis, due to the loss of micropore-bound decomposition products (**Table 5.2**).<sup>63</sup> Again, the TCA containing sample presented the lowest surface area and pore volumes. There is a possibility of pore shrinkage after carbonization at 900 °C which explains the only moderate increase in aerogel surface areas.<sup>152</sup> Concerning the elemental composition of the pyrolyzed samples, the S/N ratios now agree well between XPS and elemental analysis (**Table 5.2**). This indicates that heating has homogenized the sulfur distribution between bulk and surface, presumably *via* the loss of pendant, weakly bound sulfur species.<sup>28</sup> CA\_900 has lost virtually all sulfur species, which is consistent with the statement earlier – that cysteine as sulfur source does not result in stable, structurally bound sulfur moieties. The aliphatic sulfur groups are hence easily lost upon heat treatment.

**Table 5.2 Elemental composition of the bulk and surface of the carbon aerogels after HTC at 180 °C and subsequent pyrolysis at 900 °C, determined by elemental analysis and XPS, respectively. [NB: N<sub>2</sub> sorption-derived textural and electrical conductivity properties of the presented materials are shown on the right].**

Sample	Elemental composition by EA (wt %) and XPS (at %)					Textural properties				
	C	H	N	S	S/N	S <sub>BET</sub> (m <sup>2</sup> g <sup>-1</sup> )	V <sub>total</sub> (cm <sup>3</sup> g <sup>-1</sup> )	V <sub>meso</sub> (cm <sup>3</sup> g <sup>-1</sup> )	V <sub>micro</sub> (cm <sup>3</sup> g <sup>-1</sup> )	σ (S m <sup>-1</sup> )
CA_900	88.5	0.8	5.3	0.1	0.0(2)	267	0.47	0.40	0.07	468
	93.2	-	3.6	-	-					
CA-TC_900	87.2	1.0	4.3	1.0	0.2	321	0.48	0.38	0.09	660
	93.6	-	3.5	0.7	0.2					
CA-TCA_900	86.5	0.8	5.0	0.7	0.2	225	0.27	0.20	0.07	504
	93.1	-	3.3	0.5	0.2					

σ = Specific conductivity as determined by impedance spectroscopy

Images of the deconvoluted C1(s), N1(s) and S2(p) photoelectron envelopes of the doped organic and carbon aerogels can be found in the appendix (**Fig. A 11** and **Fig. A 12**). The peak assignments are summarized in **Table 5.3**, whereby the fraction of different species (in %) is shown below the corresponding peak values. Following the mechanistic discussions earlier, it is no surprise that the majority of sulfur species are structurally bound (*i.e.* thiophenic sulfur, assigned as **S1**) already in the as-synthesized aerogels. In this regard, the “sulfur” precursor sources were chosen due to their ability to interact with the albumin/glucose HTC intermediates *via* electrophilic aromatic substitution/cycloaddition. This leads to sulfur bound structurally within the carbonaceous framework, as opposed to pending sulfur functionalities (*e.g.* thiol).<sup>152</sup> After pyrolysis at 900 °C, practically all surface sulfur atoms are bound in a thiophenic fashion. For nitrogen, a transformation of pyrrolic nitrogen (**N2**) in the as-synthesized aerogels towards more stable pyridinic (**N1**) and quaternary (or graphitic, **N3**) nitrogen is observed, similar to the results published on other N-doped carbons.<sup>63</sup> In the case of CA-TCA\_900, 9.2 % of surface nitrogen species are present as pyridinic-N-Oxide (**N4**). Oxidation may occur as a result of oxygen species, generated during heat treatment, reacting with surface heteroatoms. The major fraction of carbon species is sp<sup>2</sup> hybridized (**C1**), and the appearance of a π-π\* shake up satellite (**C5**) after pyrolysis clearly shows that further carbonization and aromatization take place during the heat treatment, rendering the carbonaceous materials electrically conducting.

**Table 5.3 Peak assignments for the C1(s), N1(s) and S2(p)3/2 photoelectron envelopes for CA-TC and CA-TCA samples after HTC at 180 °C and after subsequent pyrolysis at 900 °C.**

Peak	Binding Energy (eV) fraction of species (%)				Assignment	
	CA-TC	CA-TC_900	CA-TCA	CA-TCA_900		
C1s	285.00	285.00	285.00	285.00	<b>C1</b> sp <sup>2</sup> C-C or C-H <sup>35, 46, 99</sup>	
	52.1	67.8	53.8	86.0		
	286.30	286.10	286.40	286.20		<b>C2</b> C-O / C-N / C-S <sup>35</sup>
	32.4	16.0	28.5	18.2		
	287.89	287.20	288.10	287.70		<b>C3</b> C=O / C=N <sup>35, 101</sup>
10.0	9.0	14.3	7.0			
	289.10	289.00	289.70	289.56	<b>C4</b> O=C-O <sup>106</sup>	
	5.5	4.1	3.1	4.4	<b>C5</b> π-π* shake up satellite <sup>18, 46</sup>	
	-	291.00	-	291.35		
		3.2		2.3		
N1s	-	398.60	-	398.68	<b>N1</b> pyridinic <sup>44, 46</sup>	
		40.9		34.6		
	400.20	-	400.20	-	<b>N2</b> pyrrolic <sup>44</sup>	
	100.0		100.0			
	-	401.40	-	401.30	<b>N3</b> quaternary <sup>35, 44</sup>	
	59.1		56.2			
	-	-	-	403.96	<b>N4</b> pyridinic N-Oxide <sup>35</sup>	
				9.2		
S2p <sub>3/2</sub>	164.10	164.20	164.30	164.27	<b>S1</b> Thiophenic (aromatic) C-S-C <sup>99, 107</sup>	
	84.5	100.0	83.2	100.0		
	166.80	-	168.10	-	<b>S2</b> oxidized sulfur <sup>99, 107</sup>	
	15.5		16.8			

### 5.2.5 The application of the carbon aerogels as electrocatalysts for the ORR

CA\_900, CA-TC\_900 and CA-TCA\_900 were tested for their electrocatalytic activity in the oxygen reduction reaction (**ORR**) of fuel cells in both alkaline and acidic media. Three main points were investigated:

- The **general catalytic activity of CA\_900**. Material synthesis and characterization of nitrogen doped carbon aerogels has been presented by White *et al.*, but no applications for the materials were presented. The catalytic activity of CA\_900 is compared to a commercially available 20 wt % platinum catalyst (**Pt@C**) and also to pure **Vulcan** carbon.



- The **effect of sulfur doping** in addition to nitrogen doping, *i.e.* the catalytic activity of CA-TC\_900 and CA-TCA\_900 compared to solely nitrogen doped CA\_900.
- The effect of the **morphological difference** between CA-TC\_900 and CA-TCA\_900.

Cyclic voltammetry (CV) at a scan rate of  $100 \text{ mV s}^{-1}$  and rotating disk electrode (RDE) voltammetry at a scan rate of  $10 \text{ mV s}^{-1}$  were conducted in  $0.1 \text{ M KOH}$  and  $0.1 \text{ M HClO}_4$  (Fig. 5.6a and d). In both cases, featureless voltammetric curves are observed for all doped carbon aerogels in the  $\text{N}_2$ -saturated solution (dashed lines). The area of the voltammograms arises from capacitive currents of the electrodes. In contrast, a well-defined cathodic peak appears in the  $\text{O}_2$ -saturated  $0.1 \text{ M KOH}$  solution (Fig. 5.6d, solid lines), clearly demonstrating the electrocatalytic activity of the doped carbon aerogels towards oxygen reduction. The areas of the voltammograms are larger in  $\text{O}_2$ -saturated solution due to Faradaic currents (*i.e.* current generated by charge transfer between reacting species).

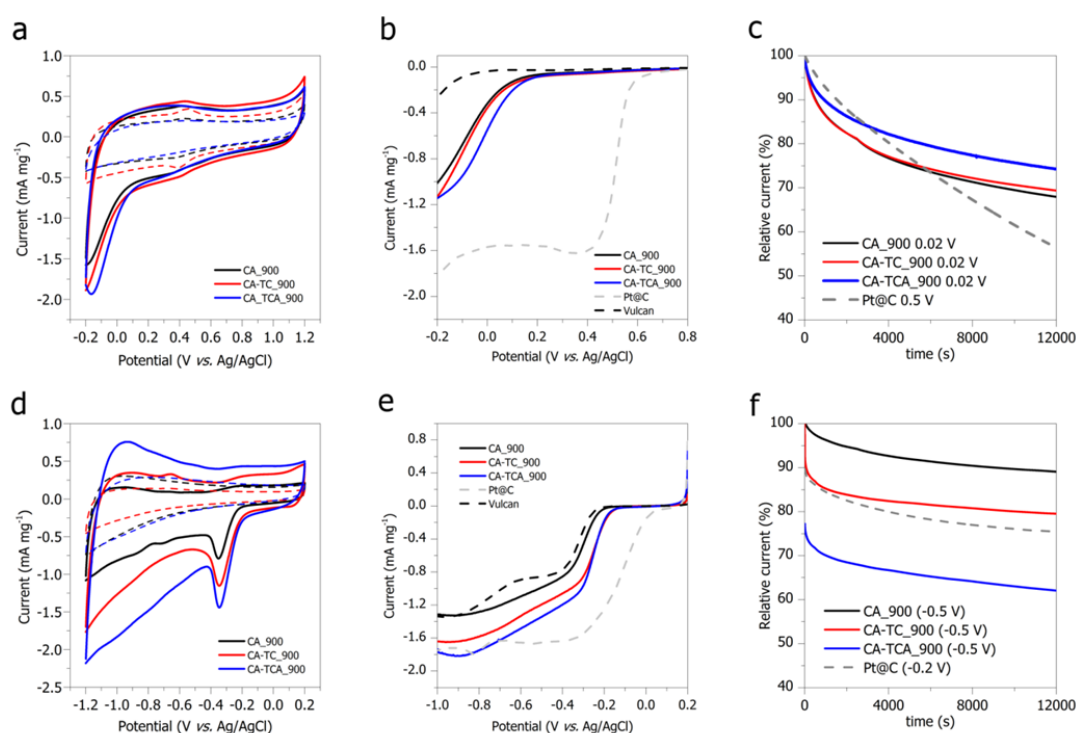


Fig. 5.6 Cyclic voltammograms of doped carbon aerogels compared to Pt@C and Vulcan in a)  $0.1 \text{ M HClO}_4$  and d)  $0.1 \text{ M KOH}$  (the dashed lines correspond to CVs obtained in  $\text{N}_2$  saturated solution and the solid lines to CVs obtained in  $\text{O}_2$ -saturated solution). Rotating disk electrode (RDE) polarization curves at 1600 rpm in b)  $0.1 \text{ M HClO}_4$  and e)  $0.1 \text{ M KOH}$ . Chronoamperic responses over 12000 s at a constant rotation speed of 1600 rpm in  $\text{O}_2$  saturated c)  $0.1 \text{ M HClO}_4$  and f)  $0.1 \text{ M KOH}$ .

In 0.1 M HClO<sub>4</sub>, Faradaic currents are similarly observed for the doped aerogels O<sub>2</sub>-saturated solution (**Fig. 5.6a, solid lines**). Because the aerogels are less active in acidic than in alkaline media, the pronounced cathodic peaks found in 0.1 M KOH are not visible in 0.1 M HClO<sub>4</sub> at the same scan rate of 10 mV s<sup>-1</sup>. The small redox peaks observed for CA\_900 and CA-TC\_900 in N<sub>2</sub>-saturated solution may be a result of heteroatom protonation on the carbon surface. The polarization curves obtained from RDE (1600 rpm) voltammetry in O<sub>2</sub>-saturated 0.1 M HClO<sub>4</sub> and 0.1 M KOH are shown in **Fig. 5.6b and e**, respectively. A summary of values derived from the plots is given in **Table 5.4**. In 0.1 M HClO<sub>4</sub>, both onset potential and maximum current density are significantly improved for all doped carbon aerogels relative to pure Vulcan. Compared to Pt@C however, the aerogels are still not competitive. In 0.1 M KOH, the performance of the doped aerogels is far more comparable with that of Pt@C. Compared to Vulcan, CA\_900 shows an improved onset potential of -185 mV as well as slightly improved current densities within the scanned potential range. The onset potential of the sulfur and nitrogen containing aerogels is more positive (both at around -130 mV) and the maximum current density is considerably higher than for Vulcan. Note that the lack of a current plateau observed for the doped aerogels may be due to either low general catalytic activity, but also due to an inhomogeneous distribution of catalytic sites.<sup>153</sup>

The chronoamperic responses (12000 s at a constant rotation speed of 1600 rpm) of all aerogels and Pt@C in O<sub>2</sub>-saturated 0.1 M HClO<sub>4</sub> and 0.1 M KOH are shown in **Fig. 5.6c and f**, respectively. Again, a summary of values can be found in **Table 5.4**. All aerogels exhibit better

**Table 5.4 Summary of values derived from linear sweep voltammetry and chronoamperometry measurements using a rotating disk electrode in O<sub>2</sub>-saturated 0.1 M HClO<sub>4</sub> and 0.1 M KOH.**

Electrochemical characterization in 0.1 M HClO <sub>4</sub> / 0.1 M KOH			
Sample	Onset potential mV <i>vs.</i> Ag/AgCl	Max. current density mA mg <sup>-1</sup>	Rel. current after 12k s CA %
CA_900	> 200 / -185	1.01 <sup>a</sup> / 1.32 <sup>b</sup>	68 / 89
CA-TC_900	> 200 / -130	1.14 <sup>a</sup> / 1.65 <sup>b</sup>	70 / 80
CA-TCA_900	> 200 / -130	1.14 <sup>a</sup> / 1.82 <sup>b</sup>	74 / 62
Pt@C	670 / 80	1.78 <sup>a</sup> / 1.73 <sup>b</sup>	56 / 75
Vulcan	33 / -220	0.26 <sup>a</sup> / 1.32 <sup>b</sup>	-

<sup>a</sup> at -0.2 V *vs.* Ag/AgCl

<sup>b</sup> at -0.9 V *vs.* Ag/AgCl

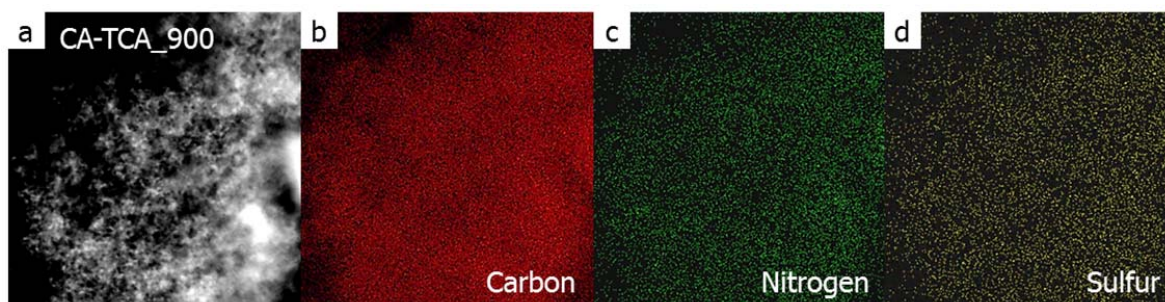


**Fig. 5.7** EDX mapping of CA-TCA\_900. a) Dark field STEM image of the sample area on which mapping was carried. b) carbon map; c) nitrogen map, d) sulfur map.

stability than Pt@C in 0.1 M HClO<sub>4</sub>. The stability decreases in the order CA-TCA\_900 > CA-TC\_900 > CA\_900. Interestingly, this order is reversed in 0.1 M KOH, *i.e.* the most active aerogel now has the lower stability, with the relative current decreasing to about 62 % after 12000 s. CA\_900 on the other hand shows a remarkable stability, retaining roughly 89 % of the initial current. CA-TC\_900 retains around 80 %, which is however still slightly higher than Pt@C (75 %). Importantly, the presented simultaneously nitrogen- and sulfur-doped aerogels show an enhanced overall performance over the solely nitrogen-doped aerogel. It is a little surprising that CA-TCA\_900, which has lower surface area, sulfur content and is also less conductive than CA-TC\_900, shows the overall best performance. Further experiments are required to identify the reasons for this behavior, but might be related to the presence of specific surface sites. The distribution of sulfur and nitrogen in CA-TCA\_900 is homogeneous, as was confirmed by EDX mapping shown in **Fig. 5.7**. Assuming that the sulfur sites are more prone to oxidation or decomposition reactions, this would also explain the order of durability in 0.1 M KOH (most active catalyst is the least stable). An explanation for the reverse trend in acidic conditions is however still required. One possibility would be that the sulfur and/or nitrogen groups are protonated in acidic media. This would render them chemically more stable compared to the more reactive form in alkaline media. This interpretation however seems inconsistent with the order of catalytic activity, which is the same as in 0.1 M KOH.

Another important factor concerning ORR catalysts is whether the mechanism goes *via* a 2 electron (forming H<sub>2</sub>O<sub>2</sub> as an intermediate) or a 4 electron process, and how selectively this occurs. Platinum usually catalyzes a 4 electron process, which is desired for efficient operation of a fuel cell.<sup>74</sup> **Fig. 5.8** shows the Koutecky Levich plots of the doped carbon aerogels in 0.1 M HClO<sub>4</sub> (at -0.2 V) and 0.1 M KOH (at -0.4 V), as well as number of electrons transferred

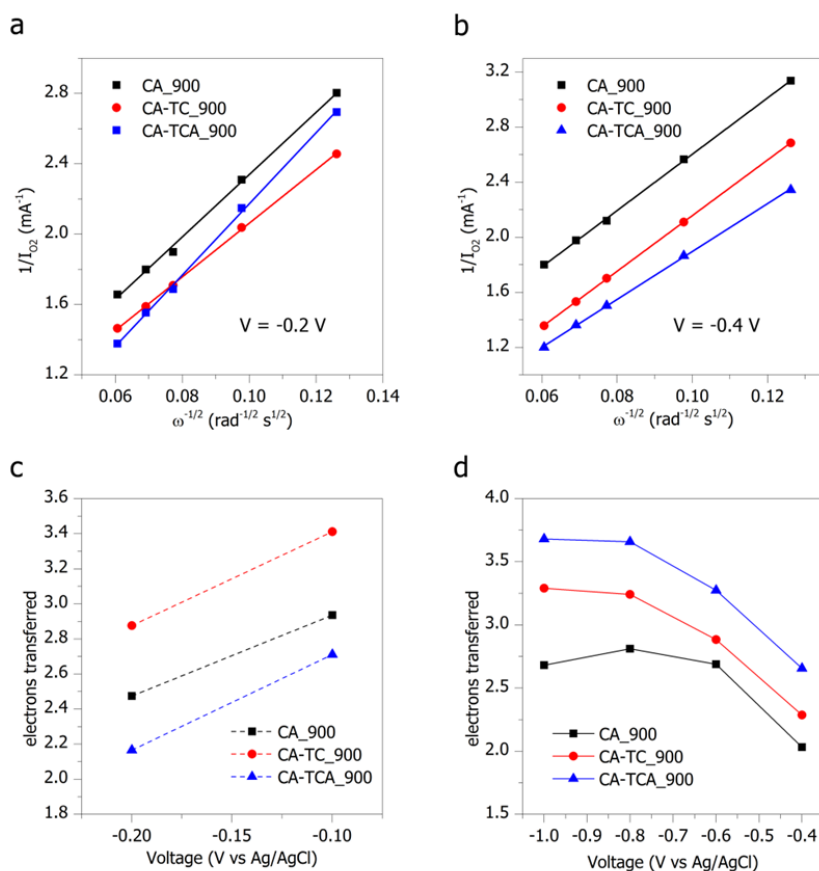


**Fig. 5.8** Koutecky-Levich plots in a) 0.1 M HClO<sub>4</sub> at -0.2 V; b) 0.1 M KOH at -0.4 V. Transferred electrons as determined by Koutecky-Levich plots at various voltages in c) 0.1 M HClO<sub>4</sub>, and d) 0.1 M KOH.

during the catalytic reaction at various voltages. The Koutecky-Levich plots show good linearity, though the mechanism for the carbon aerogels is not very selective for either the 2 or 4 electron process, but seems to comprise a mixture of the two (**Fig. 5.8a and b**). In 0.1 M HClO<sub>4</sub>, the selectivity tends towards a 2 electron process with decreasing voltages (**Fig. 5.8c**). In 0.1 M KOH, the opposite is observed, *i.e.* the electron transfer number tends towards 4 with decreasing voltages (**Fig. 5.8d**). This means that sulfur doping not only improves catalytic performance, but also the selectivity towards a 4 electron process in 0.1 M KOH, and towards a 2 electron process in 0.1 M HClO<sub>4</sub>. Note that selective 4 electron mechanisms are important for the ORR in fuel cells, because H<sub>2</sub>O<sub>2</sub> can poison the cell. Selective 2 electron processes however are also of great interest outside the context of ORR, namely for the electrochemical synthesis of H<sub>2</sub>O<sub>2</sub>.<sup>154</sup>

### 5.2.6 A possible synergistic mechanism between sulfur and nitrogen

Overall, the above findings provide indirect evidence that a small amount of sulfur doping (0.7 wt % in the case of CA-TCA\_900) is sufficient to generate profound effects on the electrocatalytic activity of carbon-based electrodes. The current knowledge in the scientific literature regarding sulfur and ORR is limited, and sulfur is usually thought to improve Pt particle adsorption onto carbon supports and thereby the lifetime of the electrode.<sup>155</sup> But what is the role of sulfur in metal free catalysts, and how does sulfur compare to nitrogen as a dopant?

In nitrogen-doped carbons, factors such as enhanced pi-bonding, electrical conductivity and Lewis basicity may facilitate reductive O<sub>2</sub> adsorption at the carbon surface<sup>156</sup> Structural defects in the carbon crystal lattice which are caused by the introduction of dopants also result in more edge-active sites.<sup>157</sup> It has however been shown that undoped carbon materials with more edge sites did not have an improved catalytic performance,<sup>158</sup> indicating that edge-bound heteroatoms, (*e.g.* pyridinic nitrogen), are catalytically important. It is generally accepted that the binding state is relevant with respect to the catalytic activity of nitrogen, though there are different opinions as to which exact binding states are responsible for good activity and 2 or 4 electron process selectivity. Pyridinic edge sites have been proposed as a likely candidate because edge planes facilitate oxygen chemisorption.<sup>83</sup> On the other hand, some reports also suggest that pyridinic nitrogen may not be an effective promoter of the 4 electron ORR process. Luo *et al.* synthesized purely pyridinic nitrogen doped carbons and found them to be selective for a 2 electron reduction pathway.<sup>159</sup> Lui *et al.* recently proposed that graphitic nitrogen accounts for good catalytic activity. They also showed that the nitrogen content does not directly correlate with the catalyst performance – materials (nitrogen-doped mesoporous graphitic arrays) with higher nitrogen content showed lower selectivity and activity.<sup>160</sup> A report by Strelko *et al.* suggested that there is a critical concentration of heteroatoms in a carbon matrix which will exhibit maximum catalytic activity and that this can be explained by the collective electronic properties and a minimal bandgap. They identified pyrrolic nitrogen as the binding state that gives rise to the smallest bandgap, and thus the best electron transfer capabilities.<sup>161</sup> DFT calculations suggest that nitrogen is not itself the catalytically active site, but that the high electronegativity of nitrogen polarizes the C-N bond, and the adjacent carbon atom therefore has a reduced energy barrier towards ORR.<sup>157, 162</sup>

In short, the many attempts to identify a mechanism for the catalytic activity of nitrogen doped carbons have yielded many different and sometimes contradicting interpretations, and a definite answer remains missing. It is possible that the catalytic mechanism of nitrogen doping is dependent on the electronic and morphological features of the material, so that a single definite catalytic pathway does not exist.

Coming back to the present case of sulfur doping, for which much less information is available, an unambiguous mechanistic proposition is clearly difficult. Some properties of sulfur can be compared to nitrogen:

- **Electronegativity.** Sulfur and carbon have electronegativities of 2.58 and 2.55, respectively (on the Pauling scale). Nitrogen on the other hand has an electronegativity of 3.04. This means that the C-S bond is not as polarized as the C-N bond, so a catalytic pathway based on a  $\delta+$  adjacent carbon atom is unlikely for sulfur.
- **Size.** Sulfur is a large atom with an (empirical) atomic radius of 100 pm compared to nitrogen (65 pm) and carbon (70 pm).<sup>151</sup> The disruption of the carbon crystal lattice is therefore more pronounced than for nitrogen, as seen by the larger interlayer spacing from XRD measurements. It is therefore likely that sulfur doping will induce more strain and defect sites in the carbon material, which may facilitate charge localization and the coupled chemisorption of oxygen.
- **Polarizability.** Sulfur has large, polarizable d-orbitals (sulfur groups are usually soft nucleophiles). The lone pairs of sulfur can therefore easily interact with molecules in the surrounding electrolyte. This effect is expected to be much more pronounced than for nitrogen.

If the “indirect” catalytic mechanism for nitrogen doped carbons is favored *i.e.* that the active site is in fact the  $\delta+$  carbon atom adjacent to nitrogen, it is immediately clear that the mechanism for sulfur doping cannot be the same as for nitrogen. Sulfur is however known to take part in proton transfer reactions. DFT calculations carried out by Chamorro *et al.* suggested that proton transfer in thiooxalic acid derivatives is facilitated by the high polarizability of the sulfur atom, which mediates ion-pair like transition states during the transfer process.<sup>163</sup> Scheiner *et al.* carried out *ab initio* calculations and showed that the greater polarizability of SH<sub>2</sub> as compared to OH<sub>2</sub> leads to greater charge transfer between (H<sub>2</sub>S--H--SH<sub>2</sub>)<sup>+</sup> units than between (H<sub>2</sub>O--H--OH<sub>2</sub>)<sup>+</sup> units and to a larger extent of spatial regions of density charge.<sup>164</sup> In their publication on sulfur-

doped graphene as ORR catalysts, Yang *et al.* propose that the increased spin density of sulfur compared to nitrogen or other dopants may be responsible for the increased catalytic activity.<sup>80</sup> This would mean that sulfur is favorable to interact with the triplet state of oxygen, as preservation of spin is a serious catalytic problem.

For the presented sulfur and nitrogen dual doped carbon aerogels, a synergistic or consecutive mechanism between sulfur and nitrogen is tentatively proposed, whereby nitrogen activates the oxygen molecule (either directly or indirectly *via* the adjacent carbon atom), while sulfur facilitates the proton transfer during the reduction process.

### 5.2.7 Summary of chapter 5.2 – albumin directed aerogels

A simple, one-pot synthesis for the preparation of dual sulfur and nitrogen-doped carbon aerogels based on sustainable precursors (*i.e.* glucose and ovalbumin) was demonstrated. This work presents the first *in situ* synthesis towards sulfur and nitrogen dual doped aerogels. The positive effect of sulfur added to nitrogen doping on the electrocatalytic performance in the oxygen reduction reaction in both acidic and basic media was demonstrated, whereby the carbon aerogels showed significantly enhanced activity in basic medium, as is typical for carbon materials. In acidic conditions all doped aerogels showed very good stability compared to a platinum based catalyst, as well as an activity which is still much better than ordinary carbon supports, but not competitive to the noble metal systems. Koutecky-Levich plots showed that both 2 and 4 electron processes take place for all aerogels tested. Finally, a synergistic mechanism between nitrogen and sulfur dopants was proposed, whereby nitrogen directly or indirectly (*via* the adjacent carbon atom) aids O<sub>2</sub> dissociation and sulfur facilitates proton transfer.

At this point it is convenient to refer back to the previous chapter on sulfur and nitrogen doped carbon hollow spheres (CHS), where it was equally observed that sulfur and nitrogen dual doped CHS show enhanced electrocatalytic performance over only sulfur and only nitrogen doped CHS. This phenomenon therefore also applies to other nano-architected carbons. Future research is required to confirm the hypothesis of a synergistic mechanism between sulfur and nitrogen. If it proves to be correct, this work provides new parameters which can be adjusted to optimize catalyst performance.

## 5.3 Heteroatom doped organic/carbon aerogels *via* the borax-mediated HTC of glucose

### 5.3.1 Introduction

Similar to the albumin-directed aerogels, the HTC of glucose in the presence of borax yields a monolithic structure comprising interconnected spherical particles. This system was originally developed by Fellerger *et al.* who were also able to show that the size of the interconnected particles could be tuned by varying the amount of borax added to the initial glucose solution. They obtained particle diameters down to  $\sim 10$  nm and surface areas of up to  $540 \text{ m}^2 \text{ g}^{-1}$ .<sup>52, 149</sup> The possibility to tune particle size, and hence surface area, is the great advantage of the borax-mediated gel formation over the albumin-directed gel formation from the previous chapter. In this regard, the borax-mediated aerogels are more competitive with the commonly used resorcinol-formaldehyde (RF) aerogels introduced by Pekala in 1989,<sup>145</sup> which similarly allow for the tuning of particle size and surface area. The drawback of the borax-mediated aerogels compared to the albumin system is that so far it has not been possible to introduce dopants into the carbon aerogels, which would be highly desirable to broaden the range of potential applications for this promising system.

It is this point at which the work reported in the following aims to extend the concept of the borax-mediated aerogel formation to the incorporation of nitrogen and/or sulfur as a dopant (**Fig. 5.9**). A series of nitrogen doped aerogels is used to investigate the extent to which the borax-mediated gel formation can be controlled in terms of particle size and heteroatom

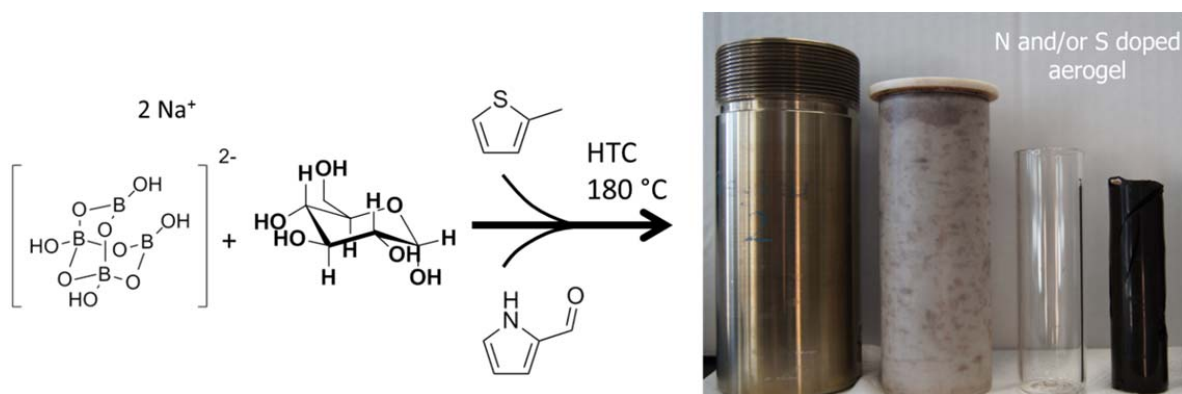


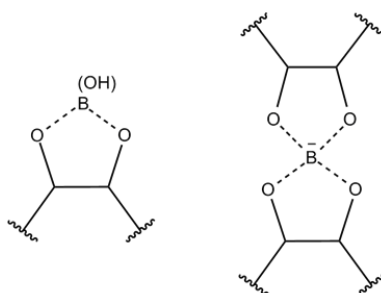
Fig. 5.9 graphical abstract of chapter 5.3



content. Using the thereby acquired knowledge, a nitrogen doped aerogel with specific properties is engineered for high performance in electrocatalysis in the oxygen reduction reaction. Finally, sulfur and sulfur/nitrogen dual doped are synthesized in order to compare the electrocatalytic behavior of carbon aerogels doped with different heteroatoms.

### 5.3.2 Mechanistic considerations

For the originally reported undoped gels derived from the borax-mediated HTC of glucose, the mechanistic proposition given by Fellingner *et al.* is as follows:



Under hydrothermal conditions, borax forms the boric acid  $B(OH)_3$  and borate  $B(OH)_4^-$ .<sup>165</sup> Borates can form reversible covalent bonds with vicinal diol groups and also crosslink two cis-diol containing molecules. Riisager *et al.* showed that the formation of negatively charged borate diol complexes enhances the reactivity towards the dehydration of glucose to HMF (*via* fructose).<sup>166</sup> They also showed that borates accelerate the isomerization of glucose to fructose, but this is expected to be negligible for the overall HTC rate since the dehydration of fructose to HMF is much slower compared to the glucose  $\leftrightarrow$  fructose isomerization that is already accelerated *via* the LBAE at elevated temperatures (see **chapter 2.1**). The borate diol complexes rather represent a competitive reaction to the formation of acetals from the aldehyde on HMF with sugar diols. Complexation of the aldehyde on HMF with sugars decreases the electron density within the furan ring, reducing its reactivity. Therefore the competitive reaction leads to increased overall reactivity due to a secondary catalytic effect in the presence of borax. According to the LaMer model (refer to **chapter 3.3.1** for more details), this accelerated reaction rate rapidly results in a critical supersaturation and hence a nucleation burst.<sup>102</sup> The large number of seeds results in smaller particles in the growth phase. The small particles together with the additional gelating effect of borax give rise to the aerogel morphology by aggregation and covalent crosslinking amongst each other. The more borax is added, the smaller the particles and the higher the surface area.

L-cysteine (**CS**), thienyl-carboxaldehyde (**TCA**), 2-methyl-thiophene (**MTP**) acid and pyrrol-carboxaldehyde (**PCA**) were tested as additives in the synthesis of sulfur and/or nitrogen doped organic aerogels using the borax-mediated approach. It was found that cysteine completely inhibited gel formation by forming large, discrete carbon microspheres. TCA, MTP and PCA resulted in successful gel formation. As before, it seems that the presence of nucleophilic amines and thiols inhibits gel formation. In the previous chapter this was attributed to competitive reactions between the heteroatom containing additive and the crosslinking protein which of course does not apply here. Instead, it was postulated that only additive which reacted with glucose and various HTC intermediates *via* cycloaddition or electrophilic aromatic substitution (like MTP, TCA, PCA) could be successfully incorporated without hampering gel formation. This is because, as seen in **chapter 2.1.3**, these reactions take place at a slow rate (compared to Maillard reactions in the presence of amino acids) and therefore do not compete with borax during the early stages of particle formation. If CS is used, fast Maillard reactions compete with the effects of borax and large microspheres are formed before particles can be effectively crosslinked to form gels.

### **5.3.3 Synthesis of organic aerogels with varying particle sizes and surface areas**

As previously mentioned, the great advantage of borax-mediated aerogels is that the size of the particles, and therefore the final surface area, may be tuned by adjusting the amount of borax added to the system (more borax – smaller particles – higher surface area). It was therefore investigated whether the introduction of a dopant influences this behavior. Three nitrogen doped organic aerogels were synthesized, each from a reaction mixture containing 0.8 g PCA, 6.0 g glucose and 14.0 g water. The borax amount was varied from 150 mg to 300 mg and 600 mg. The resulting aerogels were labeled **PCA1\_150mg**, **PCA1\_300mg** and **PCA1\_600mg** in order of increasing borax addition. The group of these three samples is hereafter referred to as the **borax series**.

### **5.3.4 Synthesis of organic aerogels with varying nitrogen contents**

It was further investigated whether the nitrogen content of the nitrogen doped aerogels could be tuned by varying the concentration of PCA added to the system. In addition to the initial

experiments which contained 0.8 g of PCA in the reactant mixture, another two experiments with higher amounts of PCA (1.3 g and 2.0 g) were carried out. All other parameters were kept constant. Each solution contained 300 mg of borax. The resulting aerogels were labeled **PCA1\_300mg**, **PCA2\_300mg** and **PCA3\_300mg** in order of increasing PCA addition. The group of these three samples is hereafter referred to as the **PCA series**.

### 5.3.5 Morphology, chemical composition and textural properties of the organic aerogels

Transmission electron microscopy (**TEM**) images (**Fig. 5.10**) show the typical borax-mediated aerogel morphology that was already observed by Fellingner *et al.*, *i.e.* a matrix comprising interconnected particles. The borax series is shown in the first row (**Fig. 5.10a to c**), nicely demonstrating the decrease in particle size with increasing borax addition. The particle size decreases from an average diameter of 75 nm, to 23 nm and finally to 16 nm with increasing borax addition.

The second row depicts the PCA series. Between PCA1\_300mg and PCA2\_300mg, there is no

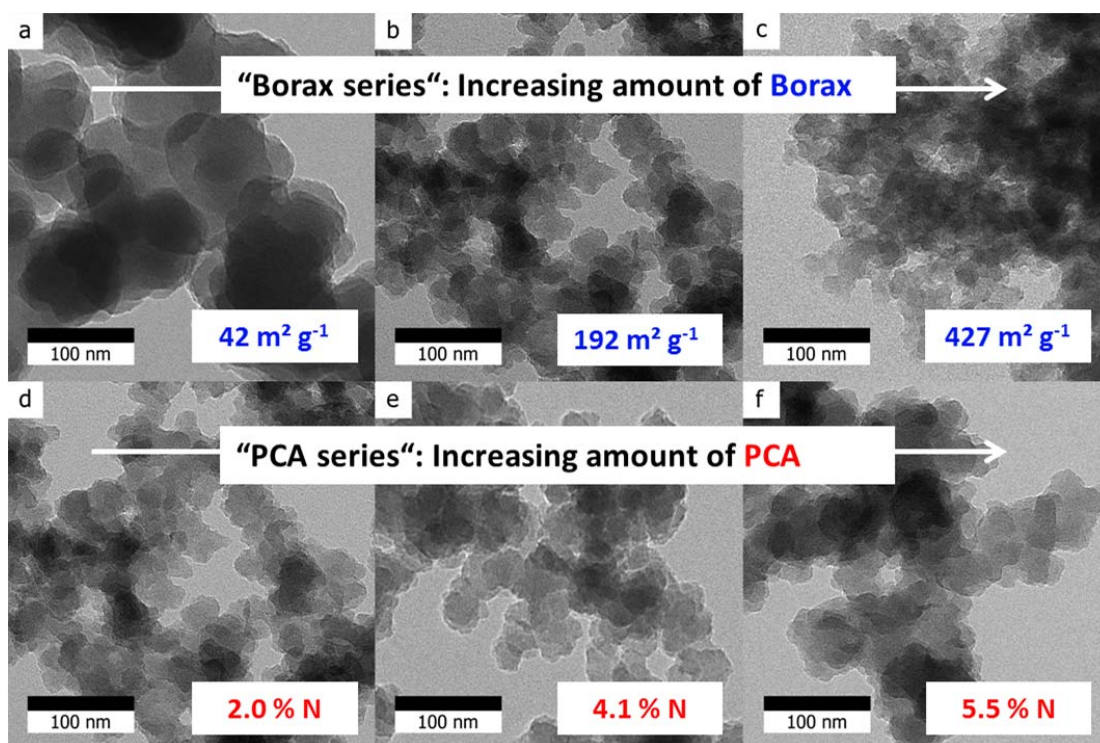


**Fig. 5.10** First row: TEM images of samples obtained with increasing Borax addition. a) PCA1\_150mg, b) PCA1\_300mg, c) PCA1\_600mg. Second row: TEM images of samples obtained with increasing PCA addition. d) PCA1\_300mg, e) PCA2\_300mg, f) PCA3\_300mg

notable particle size difference. The average particle diameters determined from TEM observations are both 23 nm (**Fig. 5.10d and e**). It seems that within this PCA concentration range, borax is the size determining factor and PCA addition does not interfere with the particle morphology. At the very high PCA levels in PCA3\_300mg (1 : 3 weight ratio of PCA to glucose, **Fig. 5.10f**) the average particle size increases to 30 nm, presumably because at such high PCA amounts, some of the borax is scavenged by the nitrogen source, thus lowering the “effective borax amount interacting with glucose”.

The elemental composition and textural properties determined by nitrogen sorption of the organic aerogels are summarized in **Table 5.5**. Within the borax series the nitrogen contents are similar, varying between 2.0 wt % and 2.2 wt %. As seen from the TEM images, the surface area increases with increasing borax addition and the resultant decrease in particle size. Within the PCA series the nitrogen content increases with increasing PCA addition, ranging from 2.0 wt % to 5.5 wt %. In accordance with TEM data, the surface areas of PCA1\_300mg and PCA2\_300mg are within a similar range while the surface area of PCA3\_300mg drops down to 80 m<sup>2</sup> g<sup>-1</sup> due to the observed increase in size.

All nitrogen doped organic aerogels after HTC at 180 °C exhibit Type IV/H3 reversible sorption isotherms with limited hysteresis loops (**Fig. 5.11**).<sup>63</sup> The lack of an adsorption plateau at high relative pressures as well as the broad pore size distribution for all samples are indicative of slit shaped pores in an open pore system. The increase in adsorbed volume at  $p/p_0$  near unity is attributed to capillary condensation in large meso or small macropores.<sup>63</sup>

Representative XPS data of PCA1\_300mg shows that the nitrogen contents solely derives from pyrrolic nitrogen (**Fig. 5.11d and Table A 1 in the appendix**).<sup>44</sup> Also, the nitrogen contents

**Table 5.5 Elemental composition and textural properties for the borax and PCA series.**

Sample	Elemental composition by EA (wt %) and XPS (at %)			Textural properties				D <sub>av</sub> nm
	C	H	N	S <sub>BET</sub> m <sup>2</sup> g <sup>-1</sup>	V <sub>total</sub> cm <sup>3</sup> g <sup>-1</sup>	V <sub>meso</sub> cm <sup>3</sup> g <sup>-1</sup>	V <sub>micro</sub> cm <sup>3</sup> g <sup>-1</sup>	
PCA1_150mg	64.2	4.4	2.2	42	0.07	0.07	0.00	75
PCA1_300mg	53.8	4.0	2.0	192	0.32	0.27	0.05	23
PCA1_600mg	82.4	-	2.0	427	0.71	0.60	0.11	16
PCA2_300mg	57.5	4.2	2.2	149	0.28	0.25	0.03	23
PCA3_300mg	64.2	4.8	4.1	80	0.17	0.15	0.02	30

D<sub>av</sub> = average diameter of aerogel particles determined from TEM images

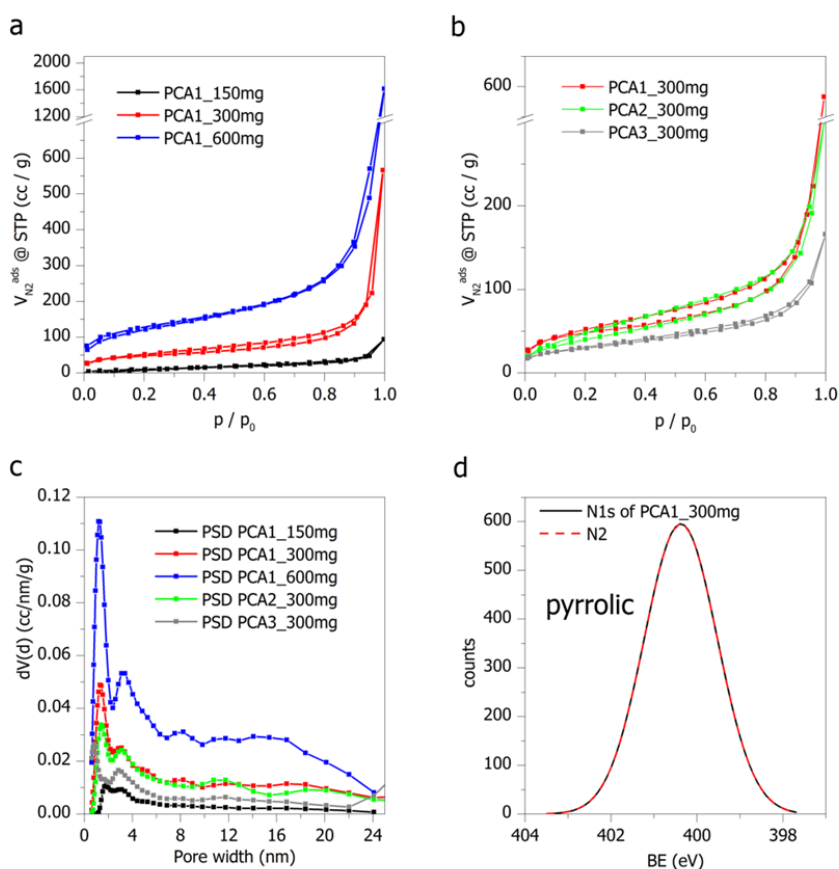


**Fig. 5.11** Nitrogen sorption isotherms of a) borax series and b) PCA series. c) pore size distributions (QSDFT model) obtained for as-synthesized aerogels after HTC at 180 °C. d) Deconvoluted N1s) photoelectron envelope of PCA1\_300mg.

derived from XPS (*i.e.* surface sensitive) and from elemental analysis (bulk) are very similar (2.00 at % and 2.0 wt %, respectively, whereby 2.00 at % correspond to 2.2 wt % nitrogen in the volume that is sampled by XPS)), indicating a homogeneous nitrogen distribution between the particle core and surface (**Table 5.5**). Fourier-transform infrared spectroscopy (**FT-IR**) of the PCA series was used to investigate the effect of increasing nitrogen concentration on the surface functionalities of the material (**Fig. 5.12**). A spectrum of CA\_300mg, *i.e.* an undoped organic aerogel, is shown for reference. The broad band at  $\sim 3300\text{ cm}^{-1}$  to  $\sim 3000\text{ cm}^{-1}$  is due to the presence of abundant hydroxyl groups in the hydrothermal carbon. Other bands that are typical for glucose-derived hydrothermal carbon are seen at  $\sim 2900\text{ cm}^{-1}$  and at  $\sim 1010\text{ cm}^{-1}$  and are attributed to aliphatic methyl/methylene and furanic C=C-O vibrations, respectively. These bands are similar in both undoped and nitrogen doped aerogels and are hence not discussed further. Regions with notable differences are highlighted in grey. The band at  $\sim 1710\text{ cm}^{-1}$

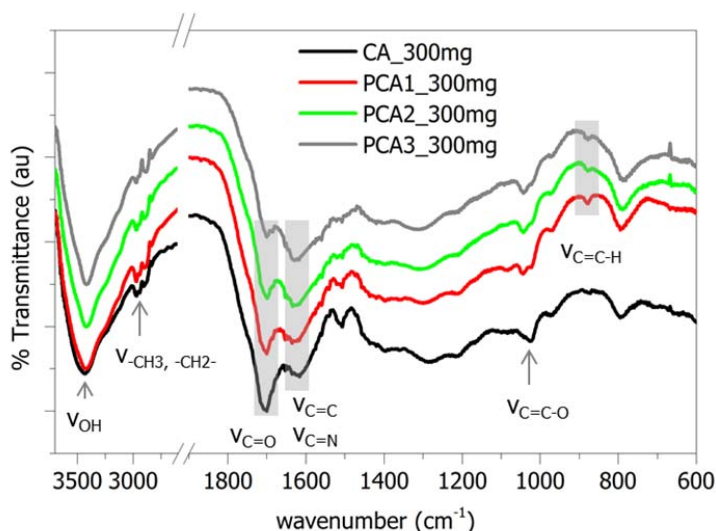


**Fig. 5.12** FT-IR spectra of the PCA series. A spectrum of CA\_300mg (*i.e.* an undoped organic aerogel) is shown for reference (black line). The spectra were vertically shifted from their original position for clarity.

corresponds carbonyl (aldehyde, ketone, carboxylic acid) functionalities whereas the bands at  $\sim 1620\text{ cm}^{-1}$  and  $\sim 870\text{ cm}^{-1}$  are attributed to aromatic C=C and C=C-H vibrations, respectively. Note the absence of amide bands ( $1630\text{ cm}^{-1}$  -  $1696\text{ cm}^{-1}$ ) for all samples, which is normally present if nitrogen nucleophilically interacts with glucose (see FT-IR spectrum of the hydrothermal carbon obtained from glucose and cysteine on **page 34**). With increasing nitrogen content, the intensity of the aromatic C=C and C=C-H bands relative to the carbonyl band increases, indicating a more aromatic carbon framework. Notably, aromatic, cyclic C=N bonds also give rise to bands in the  $\sim 1620\text{ cm}^{-1}$  region. From XPS data it is known that 100 % of surface nitrogen is bound as pyrrol, so it was concluded that the increased number of pyrrolic units in the hydrothermal carbon framework results in the increased aromaticity as seen by FT IR analysis.

### 5.3.6 Engineering a nitrogen doped aerogel with high surface area and high nitrogen content

From the studies of the effect of varying borax (at constant PCA amount) and varying PCA (at constant PCA amount) it can be concluded that:

- At constant PCA amounts (0.8 g), more borax addition results in smaller particles and hence higher surface areas. The nitrogen content is similar for all samples of the borax series.
- At constant borax amounts (300 mg), the addition of more PCA results in higher nitrogen contents. The surface area is similar for PCA amounts below a critical point, where after PCA addition results in an increased particle size and a drastic drop in surface area. This was attributed to a lower effective borax concentration caused by “scavenging” of borax by excess PCA.

The loss of surface area could make the increased nitrogen doping levels trivial when it comes to electrochemical applications, where high surface areas and good mass transport are crucial. Hence, a nitrogen doped aerogel was engineered, whereby the highest PCA (2.0 g) and the highest borax amount (600 mg) were combined. The sample was labeled **PCA3\_600mg** and exhibited the desired properties, *i.e.* both high nitrogen content (5.4 wt %) and high surface area (366 m<sup>2</sup> g<sup>-1</sup>). The average particle diameter was 15 nm. The elemental composition and textural properties are summarized in **Table 5.6** and TEM images as well as sorption isotherms/pore size distributions may be found in **Fig. A 13** and **Fig. A 14** in the appendix.

**Table 5.6 Elemental composition and textural properties PCA3\_600mg**

Sample	Elemental composition by EA (wt %)			Textural properties				
	C	H	N	S <sub>BET</sub> m <sup>2</sup> g <sup>-1</sup>	V <sub>total</sub> cm <sup>3</sup> g <sup>-1</sup>	V <sub>meso</sub> cm <sup>3</sup> g <sup>-1</sup>	V <sub>micro</sub> cm <sup>3</sup> g <sup>-1</sup>	D <sub>av</sub> nm
PCA3_600mg	62.4	4.6	5.4	366	0.44	0.33	0.11	15

D<sub>av</sub> = average diameter of aerogel particles determined from TEM images

### 5.3.7 Synthesis of sulfur and sulfur/nitrogen dual doped organic aerogels

Sulfur doping was carried out because results from previous chapters showed that sulfur and especially sulfur/nitrogen dual doped carbon materials exhibit interesting electrocatalytic properties in the ORR. Sulfur doping was achieved by using MTP as sulfur source (TCA could also be used but the results are not shown here). For the synthesis of a sulfur doped aerogel, 0.5 g MTP was added to 6.0 g glucose in 14.0 g water. In order to insure high surface area, 600 mg borax was added. The resulting aerogel will be referred to as **S-CA** from hereon. A

sulfur/nitrogen dual doped aerogel was obtained by adding 0.7 g MTP and 1.3 g PCA to a mixture of 6.0 g glucose and 600 mg borax in 14.0 g water. The resulting aerogel was labeled **SN-CA**. Elemental compositions and textural properties of the samples are summarized in **Table 5.7**. TEM images and sorption data may be found in **Fig. A 13** and **Fig. A 14** in the appendix.

**Table 5.7 Elemental composition and textural properties S-CA and SN-CA**

Sample	Elemental composition by EA (wt %)				Textural properties				
	C	H	N	S	S <sub>BET</sub> m <sup>2</sup> g <sup>-1</sup>	V <sub>total</sub> cm <sup>3</sup> g <sup>-1</sup>	V <sub>meso</sub> cm <sup>3</sup> g <sup>-1</sup>	V <sub>micro</sub> cm <sup>3</sup> g <sup>-1</sup>	D <sub>av</sub> nm
S-CA	59.0	4.5	-	1.7	292	0.60	0.54	0.06	26
SN-CA	62.3	4.4	4.1	1.4	246	0.47	0.41	0.06	17

D<sub>av</sub> = average diameter of aerogel particles determined from TEM images

FT-IR analysis of S-CA and SN-CA is shown in **Fig. 5.13**. The spectrum of S-CA is similar to a reference spectrum of undoped CA<sub>300mg</sub> while that of SN-CA is similar to the spectra obtained from the PCA series (**Fig. 5.12**). The aromatic C=C peak at 1620 cm<sup>-1</sup> has a stronger intensity than the carbonyl peak at 1710 cm<sup>-1</sup> in SN-CA which is attributed to a higher degree of aromaticity due to nitrogen doping. For S-CA the intensity is reversed although it seems to be

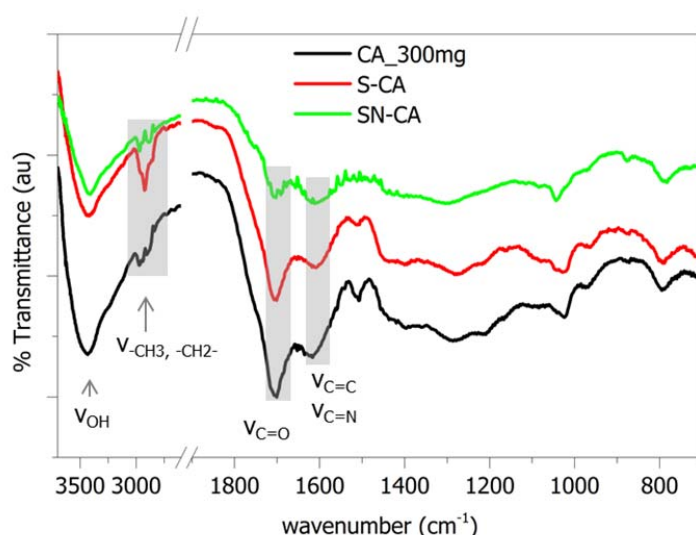


**Fig. 5.13** FT-IR spectra of S-CA and SN-CA. A spectrum of CA<sub>300mg</sub> (*i.e.* an undoped organic aerogel) is shown for reference (black line). The spectra were vertically shifted from their original position for clarity.



slightly more aromatic than CA\_300mg. Notably, S-CA exhibits a strong signal at  $\sim 2920 \text{ cm}^{-1}$  which is attributed to the methyl group on MTP.

It was also investigated whether the sulfur content could be increased by adding more MTP – an experiment with 2.0 g of MTP added to an otherwise equal reaction mixture gave a final sulfur content of 2.6 wt %. Because this sample did not exhibit superior performance in electrochemical testing, no further data is reported here. It is however interesting that the maximum sulfur doping levels accessible seem to be lower than for nitrogen.

### 5.3.8 Conversion of organic aerogels to carbon aerogels *via* pyrolysis

The aerogels obtained after HTC at 180 °C contained between 53 wt % and 65 wt % carbon and can therefore be classified as “organic” aerogels. In order to obtain “carbon” aerogels with an increased conductivity and material stability, pyrolysis at 900 °C was carried out. **Table 5.8** summarizes the elemental compositions and textural properties of the pyrolyzed carbon aerogels.

**Table 5.8 Elemental composition and textural properties of heteroatom doped carbon aerogels after pyrolysis at 900 °C. The specific conductivity values are shown on the right.**

Sample	Elemental composition by EA (wt %) and XPS (at %)				Textural properties					
	C	H	N	S	$S_{\text{BET}}$ $\text{m}^2 \text{ g}^{-1}$	$V_{\text{total}}$ $\text{cm}^3 \text{ g}^{-1}$	$V_{\text{meso}}$ $\text{cm}^3 \text{ g}^{-1}$	$V_{\text{micro}}$ $\text{cm}^3 \text{ g}^{-1}$	$D_{\text{av}}$ nm	$\sigma$ $\text{S m}^{-1}$
CA_300mg_900	93.0	1.5	0.4	-	373	0.40	0.27	0.13	16	641
PCA1_150mg_900	90.8	0.9	3.2	-	28	0.09	0.09	0.00	74	925
PCA1_300mg_900	86.6 94.0	1.0	3.0 2.5	-	179	0.36	0.32	0.04	17	549
PCA1_600mg_900	90.5	0.4	3.5	-	305	0.43	0.34	0.09	15	406
PCA2_300mg_900	88.9	1.0	4.6	-	159	0.33	0.29	0.04	22	588
PCA3_300mg_900	88.8	0.2	5.9	-	105	0.19	0.16	0.03	24	490
PCA3_600mg_900	88.4	1.3	6.3	-	265	0.48	0.41	0.07	11	433
S-CA_900	93.0	1.5	-	1.4	310	0.50	0.41	0.09	16	640
SN-CA_900	89.1	1.5	4.6	1.2	201	0.28	0.27	0.01	14	613

$D_{\text{av}}$  = average diameter of aerogel particles determined from TEM images

$\sigma$  = specific conductivity as determined by impedance spectroscopy

The carbon aerogels contained around 90 wt % carbon and have retained similar heteroatom contents. The slight increases are simply due to the relative changes in weight after loss of oxygen and hydrogen containing functionalities and are not due to the actual incorporation of nitrogen or sulfur during pyrolysis. The last column shows the corresponding specific conductivity values, confirming that pyrolysis has rendered the aerogels conducting. As a general trend, the conductivity increases with increasing particle size (due to better charge transport in the bulk) and is higher for sulfur doped samples than for nitrogen doped samples.

Low amounts of sulfur therefore seem to be better at improving electronic conductivity than nitrogen. However, attention should be paid because **chapter 3.4** showed that the conductivity increases when the sulfur doping level is too high (*ca.* 7 wt %). It is known that nitrogen doped carbons go through a maximum conductivity with nitrogen content, which however seems to be higher than for sulfur.

TEM analysis shows retention of the aerogel morphology (**Fig. A 15 in the appendix**) in all cases. The particle size has decreased slightly for most samples which is expected to arise from further condensation and carbonization of the carbonaceous framework. X-Ray diffractograms of the PCA2\_300mg\_900 shows two broad peaks at around 22 ° and 43 °, which correspond to the 002 and 100 reflections of graphite, respectively (**Fig. 5.14**). The large shift towards smaller angles indicates a large interlayer spacing. This is typical for hydrothermal carbon, and the interlayer spacing is expected to increase further due to the presence of dopants, because they can induce packing defects. Comparing the diffractogram of a nitrogen doped carbon aerogel with that of an undoped carbon aerogel (CA\_300mg\_900) however does not show a notable difference in the 002 peak position. The 002 peak for S-CA\_900 and SN-CA\_900 on the other hand is slightly shifted towards smaller angles, as is expected for the larger interlayer spacing

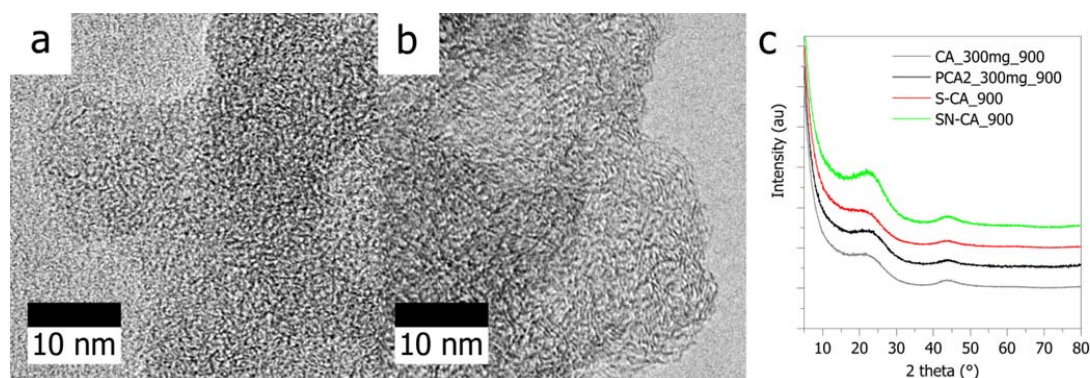


**Fig. 5.14** HRTEM images of a) CA\_300mg\_900 and b) PCA2\_300mg\_900. c) shows X-ray diffractograms of undoped, N, S and S/N doped carbon aerogels.

created by the comparatively large sulfur atom (**Fig. 5.14c**). High resolution transmission electron microscopy (**HRTEM**) images show that both the undoped and nitrogen doped carbon aerogels have highly disordered graphitic layers (**Fig. 5.14a and b**, respectively). All carbon aerogels continue to exhibit type IV H3 nitrogen sorption isotherms (**Fig. A 16 in appendix**). The decrease in the apparent BET surface areas for most of the samples is due to a) overall contraction of the carbon framework upon further carbonization and b) micropore shrinkage which results in ultramicropores (*i.e.* < 1 nm) which cannot be detected by nitrogen sorption.<sup>167</sup> The overall order of surface area between the samples is however similar to that observed for the as-synthesized organic aerogels.

### 5.3.9 Electrochemical characterization of carbon aerogels

The nitrogen doped carbon aerogels pyrolyzed at 900 °C were tested for their ORR related electrocatalytic activity. Four main points were investigated:

- The effect of **surface area** of the nitrogen doped carbon aerogels. A comparison among **the borax concentration series**.
- The effect of nitrogen content of the nitrogen doped carbon aerogels. A comparison among **the PCA concentration series**.
- The electrocatalytic performance of **PCA3\_600mg\_900**, *i.e.* high nitrogen content and high surface area.
- A comparison between sulfur, nitrogen and sulfur/nitrogen doped carbon aerogels.

Cyclic voltammetry (**CV**) and linear sweep voltammetry (**LSV**) using a rotating disk electrode (**RDE**) was carried out in 0.1 M KOH. Featureless voltammetric curves were observed for all samples in N<sub>2</sub>-saturated solution. A strong cathodic peak is seen upon saturating the solution with O<sub>2</sub>, showing the catalytic effect of the nitrogen-doped borax gels towards oxygen reduction (**Fig. 5.15a to c**).

**Analysis of the polarization curves for borax concentration series (Fig. 5.15b)** reveals a direct correlation of surface area, onset potential and maximum current density. The higher the surface area (*i.e.* the more borax is added), the better the onset potential and maximum current densities over the scanned potential range. Notably, the low surface area of PCA1\_150mg\_900 (28 m<sup>2</sup> g<sup>-1</sup>, **Table 5.8**) results in a poor catalyst performance which is even lower than pure

Vulcan carbon (dashed black line). PCA1\_300mg\_900 exhibits only slightly improved current densities, but a similar onset potential, to an undoped aerogel containing the same amount of glucose and borax, but no PCA (CA\_300mg\_900, red dashed line). It is assumed that the nitrogen content of 3.0 wt % improves material conductivity, but otherwise has no obvious effect on the electrocatalytic performance.

**Analysis of the polarization curves for PCA concentration series (Fig. 5.15e)** shows that the overall catalytic performance is in the order  $\text{PCA3}_{300\text{mg}_900} < \text{PCA1}_{30\text{mg}_900} < \text{PCA2}_{300\text{mg}_900}$ , *i.e.* the sample with the highest nitrogen doping levels has the lowest electrocatalytic activity. This can however be easily explained by the decreased surface area of PCA3\_300mg\_900 compared to the other two samples. As expected, the drop in surface area due to the increased particle size counteracts the potential benefits of higher nitrogen contents. PCA3\_300mg\_900 has a similar activity as Vulcan carbon whereas PCA2\_300mg\_900 is already more comparable to Pt@C. Between PCA1\_300mg\_900 and PCA2\_300mg\_900, the onset potential is similar but the current density varies, further supporting the earlier statement, that

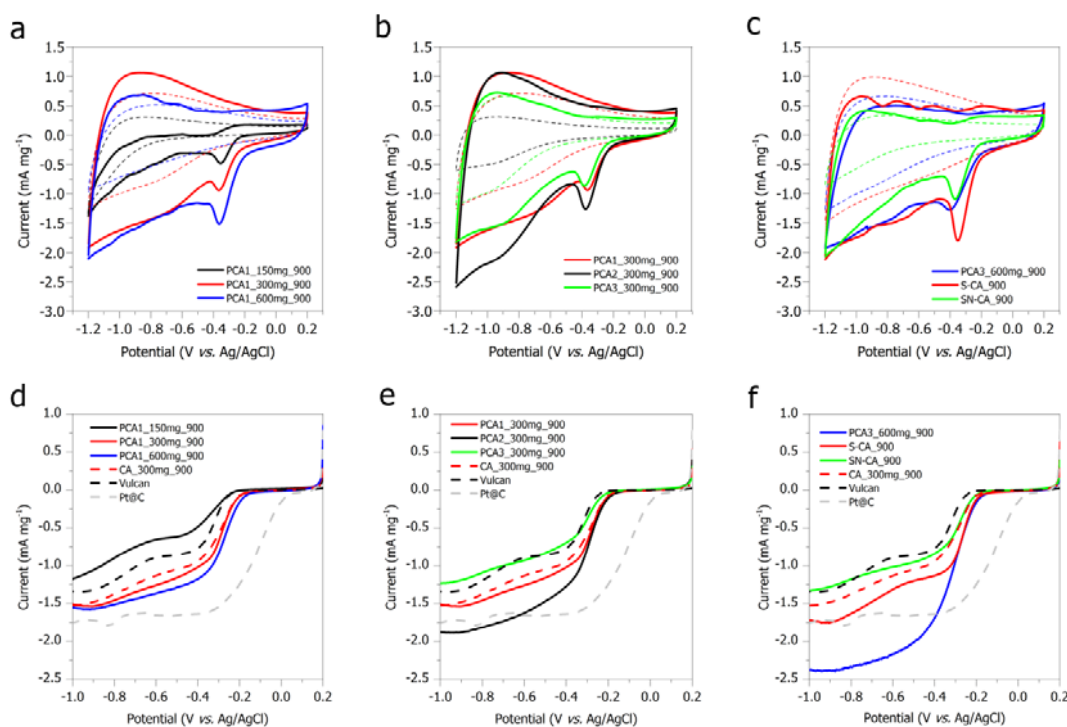


**Fig. 5.15** Cyclic voltammograms obtained in  $\text{N}_2$ -saturated (dashed lines) and  $\text{O}_2$ -saturated (solid lines) 0.1 M KOH for a) borax concentration series, b) PCA concentration series and c) nitrogen and/or sulfur doped carbon aerogels. Polarization curves obtained with an RDE in 0.1 M KOH at 1600 rpm for d) borax concentration series, e) PCA concentration series and f) nitrogen and/or sulfur doped carbon aerogels. Data for undoped CA\_900 (dashed red line), Vulcan (dashed black line) and 20 wt % Pt@C (dashed grey line) is shown for reference.

nitrogen doping improves conductivity but has otherwise no effect.

**PCA3\_600mg\_900** which has both high nitrogen content and surface area very clearly exhibits the best overall catalytic performance out of all tested samples (**Fig. 5.15f**). The current densities now exceed those of Pt@C and the onset potential is slightly improved compared to the remaining carbon aerogels. It seems that doping levels of > 6 wt % are required for nitrogen to exhibit an effect on the onset potential.

**S-CA\_900** exhibits the same onset potential as PCA3\_600mg\_900 as well as improved current densities compared to CA\_300mg\_900 over the scanned potential range. Doping with only sulfur therefore results in beneficial materials properties, similar to doping with only nitrogen. It should be noted that the sulfur doping levels are quite low (1.4 wt %). A material obtained with higher sulfur doping levels (~ 2.6 wt %) proved to be a less efficient catalyst (data not shown). It is hence likely that there is an optimal doping level for sulfur (< 2 wt %), which is much lower than for nitrogen (> 6 wt %). From the two previous chapters it might be expected that **SN-CA\_900** exhibits better electrocatalytic performance than the solely nitrogen or solely sulfur doped carbon aerogels due to a synergistic effect between sulfur (proton transfer) and nitrogen (activation of oxygen). However, it was found that SN-CA\_900 in fact exhibits the worst performance out of the three (**Fig. 5.15f**). This may on one hand be attributed to the comparatively low surface area of SN-CA\_900, but it is also likely that optimization of the nitrogen/sulfur ratio is required to achieve a beneficial synergistic effect between the two dopants. Importantly, the performance drop in SN-CA\_900 indicates that dual sulfur and nitrogen doped materials do not simply exhibit the sum of (solely) sulfur and (solely) nitrogen doped carbons, *i.e.* the effects of the individual dopant are not independent from each other (otherwise a catalytic performance similar to that of PCA2\_300mg\_900 would have been expected because the nitrogen doping levels as well as surface areas of the two samples are similar). Koutecky Levich plots were determined for the carbon aerogels with the best performance (*i.e.* PCA1\_300mg\_900, PCA1\_600mg\_900, PCA2\_300mg\_900 and PCA3\_600mg\_900) at -0.4 V (*vs.* Ag/AgCl). They all show good linearity (**Fig. 5.16a**). **Fig. 5.16b** shows the electron transfer numbers determined at various voltages. None of the samples show good selectivity for either the 2 or 4 electron process over the voltage ranges. The values for PCA3\_600mg\_900 are however closest to an ideal 4 electron process which is favored for applications in fuel cells. Since PCA3\_600mg\_900 demonstrates the best catalytic performance out of all tested samples, chronoamperometry was carried out to test catalyst stability over long

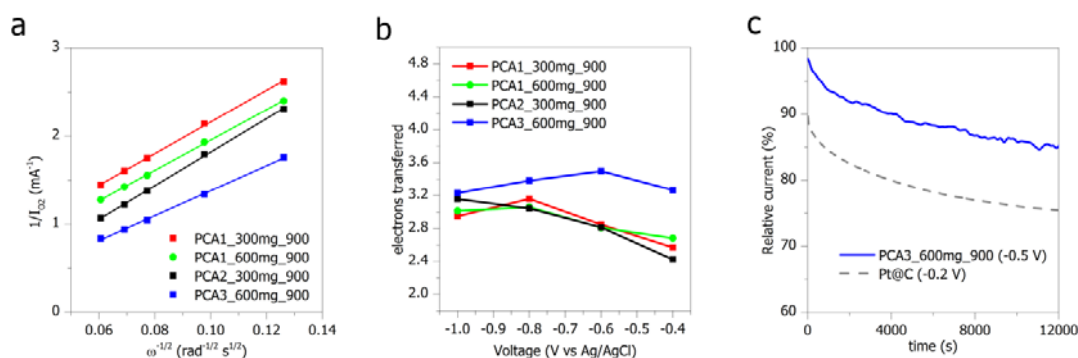


**Fig. 5.16** a) Koutecky-Levich plots determined at  $-0.4$  V for selected aerogels, b) electron transfer numbers at different voltages for the corresponding carbon aerogels and c) chronoamperometry of PCA3\_600mg\_900.

time periods (12 000 seconds) (**Fig. 5.16c**). Results indicate that the carbon aerogel is very stable under the tested conditions (0.1 M KOH,  $V = -0.5$  V *vs.* Ag/AgCl), retaining  $> 85$  % of its initial current density after 12000 s (blue line). Comparatively, the platinum catalyst current density drops down to 75 % (grey dashed line).

### 5.3.10 Summary of chapter 5.3 – borax mediated aerogels

Using a modification of the borax-mediated aerogel formation in the hydrothermal carbonization of glucose it was possible to successfully introduce nitrogen and/or sulfur as dopants. 2-pyrrol-carboxaldehyde (PCA) and 2-methyl-thiophene (MTP) were thereby simply added to a borax/glucose solution and hydrothermally treated at  $180$  °C. Supercritical  $\text{CO}_2$  drying was used to prevent collapse of the nanostructured aerogels due to capillary forces. It was shown that both the particle size (and hence surface area) and the nitrogen content can be tuned by varying the amounts of borax or PCA used. The MTP system can be similarly influenced, although the accessible amount of sulfur doping is lower than for nitrogen. Pyrolysis at  $900$  °C of the organic aerogels rendered the resulting carbon aerogels electrically conducting. Electrochemical testing of the carbon aerogels as catalysts in the oxygen reduction reaction showed that catalytic activity increases with higher surface area and with higher nitrogen content. A solely sulfur doped carbon aerogel showed improved catalytic activity over an undoped control, but lower activity than the best nitrogen doped carbon aerogel. A S/N dual doped carbon aerogel exhibited the lowest electrocatalytic activity with respect to the nature of the dopant molecules. This contradicts results from previous chapters where S/N dual doped

materials were superior catalysts over undoped or solely nitrogen doped carbons. However, only one S/N gel was tested and it is possible that the nitrogen to sulfur ratio must be adjusted to achieve a good synergistic activity between the two dopants. Importantly, a carbon aerogel with high surface area and high nitrogen content was engineered to maximize catalytic performance. The obtained sample PCA3\_600mg\_900 exhibited drastically improved current densities compared to a platinum catalyst (but lower onset potential), as well as excellent long term stability. Koutecky-Levich analysis indicated that the selectivity of PCA3\_300mg\_900 tended towards an ideal 4-electron process.

## 5.4 Summary of the “chemical modification” chapters

---

This concludes the chapters on chemical modifications of carbon materials derived from hydrothermal carbonization. To summarize, it was shown that even with a very naïve understanding of the mechanism, controlled manipulation of the HTC process is possible. Sulfur was introduced as a new dopant in the context of HTC and high potential materials that are doped with nitrogen, sulfur, or both sulfur and nitrogen were synthesized. **Chapter 3** demonstrated that the dopant containing additive can be chosen in such a way to influence the final binding state of the dopant molecule. Previously, tuning of the heteroatom binding states had occurred exclusively by tuning the pyrolysis temperature, whereby higher temperatures result in more stable binding motifs. The ability to control the chemical state already at the comparatively low temperature HTC stage facilitates the retention of higher doping levels after pyrolysis. HTC can therefore be regarded as an “intermediate” step in the formation of carbon materials with higher doping levels than materials obtained from direct pyrolysis of carbon precursors. **Chapters 3 and 4** concerned themselves with template and template-free routes to introduce surface area into the doped carbon materials. Surface area is a prerequisite for most catalytic applications and the first glucose based, HTC-derived, template-free nanostructured material that can partially outperform a state-of-the-art platinum catalyst in the ORR was presented. The next chapter will introduce a different method of manipulating hydrothermal carbonization. Rather than tuning the chemical nature of the process by using different reactants, the physical process is targeted. For this, we move away from the “low temperature” regime, *i.e.* HTC at 180 °C, and look at what happens during HTC at much higher temperatures of above 500 °C – HTC in superheated vapor.

# 6 High temperature hydrothermal carbonization I

## Carbon microspheres from different carbohydrates

---

### 6.1 Introduction

HTC may be categorized into two main regimes:<sup>8</sup>

- 1) The low temperature regime (*l*HTC) which proceeds below 300 °C. Functional carbonaceous materials are obtained *via* dehydration and polymerization schemes known from ordinary organic chemistry (refer to **chapter 2.1** for more details). All work in the previous chapters was carried out within this regime (at 180 °C).
- 2) The high temperature regime (*h*HTC) which proceeds between 300 °C and 800 °C, *i.e.* at temperatures beyond the stability of standard organic compounds.

HTC in the low and high temperature regimes gives rise to very different materials. *l*HTC results in carbonaceous materials (carbon content of *ca.* 60 wt %) with abundant oxygen-containing functional groups, whereas *h*HTC generally results more graphitic structures with high carbon contents.<sup>8</sup> Examples for the latter include the conversion of amorphous carbon to graphitic carbon nanocells,<sup>168</sup> or multi-walled carbon nanotubes<sup>168, 169</sup> at high temperature (> 600 °C) and pressure (100 MPa). There are also reports on the formation of carbon films on silicon carbides at 300 °C to 800 °C and 100MPa.<sup>170</sup>

The supercritical state of water (**scH<sub>2</sub>O**) lies beyond the critical point at  $T_c = 374$  °C and  $p_c = 22.1$  MPa.<sup>171</sup> The mentioned *h*HTC examples from literature were therefore carried out under scH<sub>2</sub>O conditions. Supercritical fluids have transport properties that are similar to those of gases (low viscosity, high diffusivity, low surface tension) but solvating powers similar to those of liquids. Restrictions due to mass transfer do not apply.<sup>172</sup> scH<sub>2</sub>O has low dielectric constants (as low as 3, but varies with temperature and pressure) that are in the range of that for common organic solvents, *i.e.* scH<sub>2</sub>O behaves like a non-polar solvent which can dissolve organic molecules and precipitate salts.<sup>173</sup> This makes it a suitable medium for a wide range of



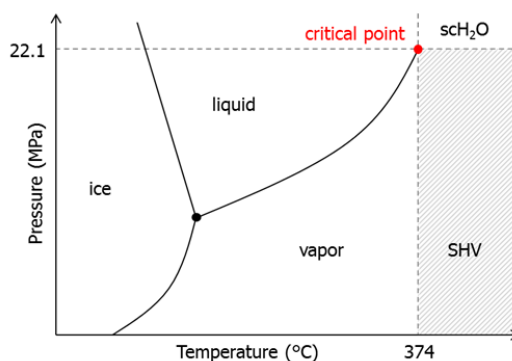


**Fig. 6.1** A simplified phase diagram for water showing the triple point (black circle) and the critical point (red circle). The superheated vapor (SHV) region is highlighted in grey.

reactions, such as hydrolysis, hydrations, dehydrations and oxidations.<sup>172</sup> A drawback for synthesis in  $\text{scH}_2\text{O}$  however is the highly corrosive nature of the medium. Especially in the presence of acids and oxygen (both found during HTC),  $\text{scH}_2\text{O}$  corrodes the reactor materials and fittings.<sup>172</sup> Few materials are able to resist corrosion by  $\text{scH}_2\text{O}$  - the authors cited above for example,<sup>168, 169</sup> used small gold capsules in which the carbon precursor was tightly sealed with water. The entire gold capsule was then placed in a high pressure autoclave for *h*HTC treatment. This approach clearly presents difficulties for the scale-up of the *h*HTC process. Hastelloy C (very stable Ni/Cr/Mo alloys) flow reactors were used by Salvador *et al.*<sup>173</sup> A Hastelloy C high pressure autoclave was used for the herein presented work. However, when  $\text{scH}_2\text{O}$  conditions were reached, metal traces from the reactor were found in the product and the reaction was difficult to control with irreproducible results. *h*HTC was therefore carried out at 550 °C but at subcritical pressures (*ca.* 10 to 50 bar).

In the water phase diagram (**Fig. 6.1**) this corresponds to superheated vapor (**SHV**). SHV (or in the case of water, superheated steam) is vapor that has been heated above its liquid/vapor saturation temperature for a given pressure (*i.e.* the system is no longer moving along the black phase equilibrium lines in **Fig. 6.1**). In SHV, liquid particles cannot exist as they would be evaporated as soon as they are formed due to the excess thermal energy of the system. All the water under SHV conditions is in a gaseous state, which is expected to have a different influence on the *h*HTC system than water in *h*HTC where the vapor and liquid phases are in equilibrium. For example, ionic reactions are enhanced in subcritical conditions while free radical mechanisms generally suppressed by liquid water. The latter become more dominant in supercritical conditions and at low density such as in superheated vapor.<sup>174</sup>

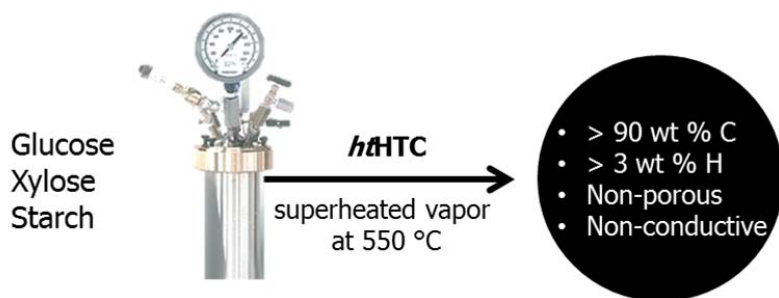


**Fig. 6.2** graphical abstract of chapter 6

This chapter concerns the initial synthesis and characterization of hydrothermal carbon microspheres *via* *h*HTC in superheated vapor. As for the previous sections, glucose (a hexose) was chosen as a model compound for biomass. However, because *h*HTC has not been previously carried out before, some experiments to verify a broader validity of the presented findings were also conducted with xylose and starch as model pentose and polysaccharide, respectively (**Fig. 6.2**). The obtained microspheres were characterized with respect to their physicochemical properties in comparison to carbon microspheres obtained *via* *l*HTC under mild conditions and subsequent pyrolysis at 550 °C. It was also investigated whether *h*HTC can replace pyrolysis as a post-treatment step to obtain highly carbonized and conductive materials.

## 6.2 Experimental considerations

The high temperature Hastelloy C autoclave used for the presented experiments allows for heating to maximum 600 °C, with pressures of up to 360 bar. A temperature of 550 °C was chosen in order to draw a direct comparison with samples prepared from *l*HTC at 180 °C followed by pyrolysis at 550 °C. 10 ml of a 10 wt % solution of the carbohydrate was prepared and placed into a quartz glass open-ended cylindrical vial which was then sealed into the high temperature autoclave. Note that the conventional borosilicate glass vials used in *l*HTC are not suitable for *h*HTC because they are partially dissolved by the hot water. The relatively small volumes of water gave rise to moderate pressures (< 50 bar), keeping the solvent in a superheated vapor regime.

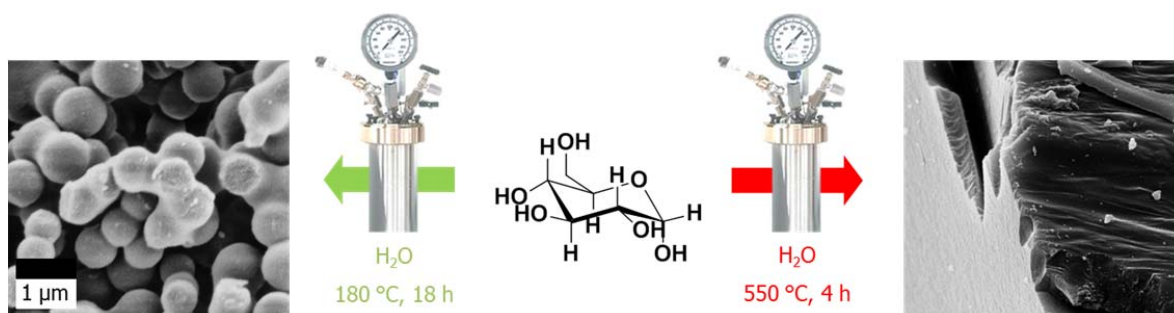


**Fig. 6.3** A schematic representing the difference in product morphology after HTC at 180 °C and after HTC at 550 °C using a single heating step.

Rapid heating to 550 °C (the final temperature was reached after *ca.* 1 h) of the carbohydrate precursor solution resulted in the loss of the spherical product morphology that is usually observed for HTC at 180 °C (**Fig. 6.3**). This may be attributed to the rapid reaction rates in superheated water and superheated vapor which resulted in uncontrolled carbonization before spheres can be formed. The uncontrolled morphology formation presents a clear disadvantage for the synthesis of defined nano-architectures. To circumvent nanostructure loss during high temperature treatment, a two-step heating profile was used:

- **Controlled morphology formation** at 180 °C for 16 h, similar to “low temperature” HTC. During this stage the morphology may be controlled in a similar fashion to the examples given in previous chapters. Specifically, carbon microspheres, hollow spheres and aerogels may be formed (see **chapters 3 to 5**).
- **Carbonization in superheated vapor** at 550 °C for 2 h to 4 h. During this stage, the material is further carbonized and loss of functional groups results.

The carbohydrate samples after *h*HTC using the two step heating profile are hereafter collectively referred to as **CBH\_180/550**, where CBH = **Glu**, **Xyl** or **Stc** for glucose, xylose and starch, respectively. The products obtained from the same precursors after HTC at 180 °C are referred to as **CBH\_180**. The products obtained by pyrolysis at 550 °C of CBH\_180 are referred to as **CBH\_P550**.

## 6.3 Carbon microspheres derived *via ht*HTC of xylose, glucose and starch

### 6.3.1 Morphological investigations

Scanning electron microscopy (SEM) images in **Fig. 6.4** show a comparison of CBH\_180 and the corresponding CBH\_180/550. The spherical morphology, both interconnected spheres for glucose and starch and discrete spheres for xylose retained after the high temperature treatment using a two-step heating profile. The increase in size is attributed to the SHV environment. During HTC, small organic molecules are formed as side products (*e.g.* levulinic acid and formic acid, refer to **chapter 2.1**). In *ht*HTC, not all of the side products are incorporated into the hydrothermal carbon. At 550 °C however, all small organic molecules are broken down and the thereby resulting carbon building blocks can then be added onto the existing spheres during further carbonization.<sup>172</sup> Additionally, the higher reaction pressure influences the process according to LeChatelier's principle, *i.e.* the reaction equilibrium shifts towards more dense

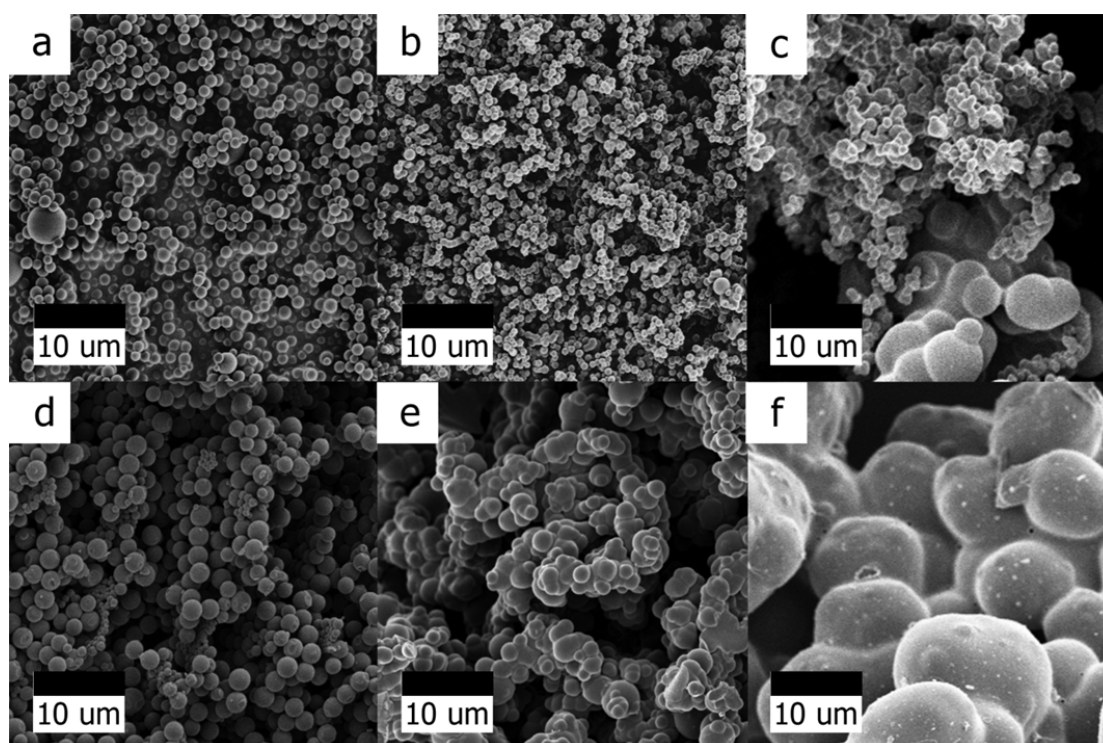


**Fig. 6.4** SEM images of xylose, glucose and starch (a, b and c, respectively) after HTC at 180 °C. The second row shows the corresponding carbohydrates treated at 550 °C using a two-step heating profile (d, e and f, respectively).

products as the overall pressure is increased. Products initially lost during the carbonization process as volatiles may therefore re-enter the reaction cycle.<sup>171</sup> The complete breakdown of small organic molecules is further evidenced by the fact that whilst after HTC at 180 °C the liquid phase is yellow to brown in color, it is clear after HTC at 550 °C.

### 6.3.2 Elemental composition and surface functionality

Fourier-transform infrared spectroscopy (**FT-IR**) of CBH\_180/550 reveals a significant decrease in the intensity of all vibrations corresponding to oxygen functional groups that are normally seen for hydrothermal carbon after HTC at 180 °C (Glu\_180 is shown for reference, dashed black line in **Fig. 6.5**). The broad –OH band at 3700-3000  $\text{cm}^{-1}$  seen for all CBH\_180 disappears completely (not shown) and the intensity of the carbonyl/carboxyl bands around 1700  $\text{cm}^{-1}$  as well as several bands in the region from 1000  $\text{cm}^{-1}$  to 1300  $\text{cm}^{-1}$ , assigned to various C-O (esters, lactones *etc.*) vibrations decrease significantly.<sup>106</sup> On the other hand, the aromatic vibrations at *ca.* 1600  $\text{cm}^{-1}$  (aromatic C=C) and the characteristic bands around 800  $\text{cm}^{-1}$  (aromatic C=C-H) are still present in CBH\_180/550. An FT-IR spectrum of glucose-derived hydrothermal carbon at 180 °C and subsequent pyrolysis at 550 °C is shown as a dashed grey line. Comparing this with the spectra of CBH\_180/550 clearly shows that the products obtained during *h*HTC at the same temperature are more carbonized and contain less functional groups. *h*HTC therefore goes through a different carbonization pathway than the products formed from HTC at 180 °C and subsequent pyrolysis.

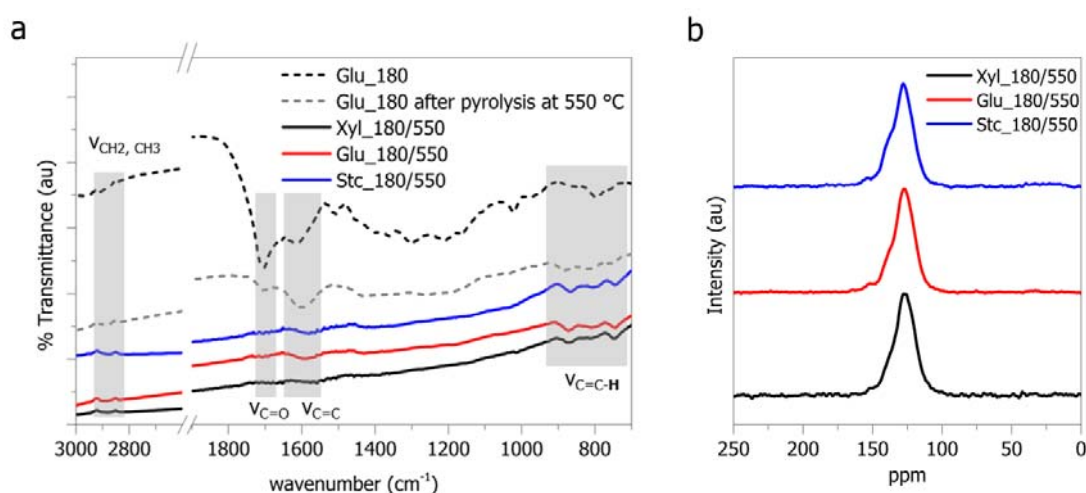


**Fig. 6.5** a) FT-IR spectra of CBH\_180/550. Spectra of Glu\_180 before and after pyrolysis at 550 °C are shown for reference. b)  $^{13}\text{C}$  ssNMR spectra of CBH\_180/550.

$^{13}\text{C}$  solid state NMR ( $^{13}\text{C}$  ssNMR) analysis reveals a single sharp peak at 129 ppm for CBH\_180/550 which is generally attributed to carbon materials with high aromaticity (*e.g.* graphitic carbons or long range conjugated double bonds). A  $^{13}\text{C}$  ssNMR spectrum obtained from pyrolyzed Glu\_180 at 550 °C can be found in a report by Falco *et al.* and similarly shows a sharp peak at 129 ppm, but also a strong shoulder at 151 ppm.<sup>175</sup> They attributed this to phenolic carbons (the *ipso* carbon of hydroxyl substituted aromatic domains), rather than to furanic units, the presence of which would give rise to a second shoulder at 121 ppm.<sup>55, 175, 176</sup> A shoulder at  $\sim 151$  ppm is also present in CBH\_180/550 but it is much weaker than for pyrolyzed hydrothermal carbon at the same temperature, indicating less phenolic functions in the *h*/HTC derived products.

Elemental analysis is in good agreement with FT-IR and  $^{13}\text{C}$  ssNMR data. In accordance with increased dehydration, decarboxylation and aromatization, the carbon contents are highly increased whereas the oxygen contents are decreased in CBH\_180/550 and CBH\_P550 relative to CBH\_180 (**Table 6.1**). The carbon content of CBH\_180/550 are higher than in CBH\_P550 by about 10 wt % whereas the hydrogen contents are similar, *i.e.* CBH\_180/550 contain abundant C-H groups which were not affected by heat treatment but have lost more oxygen functionalities than during pyrolysis. This is in fact also supported by the FT-IR spectra which show that the peak at around  $2900\text{ cm}^{-1}$  (aliphatic C-H stretches) remains to a certain extent in the high temperature samples. Representative X-ray photoelectron spectroscopy (XPS) data for

**Table 6.1 Elemental composition of the bulk and surface of CBH\_180, CBH\_180/550 and CBH\_P550, as determined by elemental analysis (wt %) and XPS (at %), respectively.**

Sample	Elemental composition by EA (wt %) and XPS (at %)		
	C	H	O <sub>calc</sub>
Xyl_180	68.5	4.1	27.4
Glu_180	66.8	4.4	28.9
Stc_180	67.1	4.5	28.4
Xyl_P550	83.6	3.5	12.9
Glu_P550	82.7	3.1	14.2
Stc_P550	83.5	3.5	13.0
Xyl_180/550	91.1	3.0	5.0
Glu_180/550	93.6	3.2	2.2
Stc_180/550	87.4	3.3	8.2

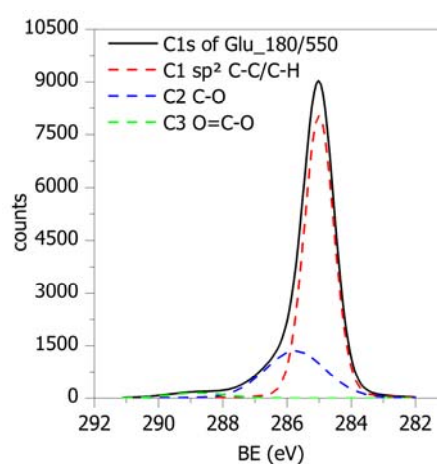


**Fig. 6.6 Deconvoluted C1s photoelectron envelope of Glu\_180/550.**

Glu\_180/550 indicate that the majority of carbon atoms are present in an  $sp^2$  hybridized state, with minor contributions from ether and ester groups (**Fig. 6.6**). Notably, no carbonyl groups were found in accordance with FT-IR and  $^{13}C$  ssNMR data.

### 6.3.2.1 Physical properties – crystallinity and conductivity

The increased aromatization is corroborated by X-Ray diffraction (**XRD**) and Raman measurements. The XR-Ray diffractograms of CBH\_180/550 exhibit two main peaks at around  $24^\circ$  and  $43^\circ$ , corresponding to the 002 and 100 lattice spacings of hexagonal graphite respectively (**Fig. 6.7a**). Notably the 002 reflection is at lower angles compared to pure graphite ( $26^\circ$ ) which indicates an increased spacing between the graphitic layers. These peaks are not as pronounced for Glu\_P550 (light grey line) which is more amorphous than CBH\_180/550. Clearly, the reaction medium plays a crucial role in the efficiency of the carbonization process. Stc\_180/550 seems the least crystalline out of the three samples. Since starch is the most complex out of the carbohydrate precursors it is conceivable that the carbonization process will be the least efficient because the polysaccharide needs to be broken down first. The Raman measurements shown in **Fig. 6.7b** provide additional support for high levels of aromatization. The D ( $1344\text{ cm}^{-1}$ ) and G ( $1601\text{ cm}^{-1}$ ) peaks can clearly be seen. The increased intensity of the G peak corresponds to graphitized domains within the sample. The G peak intensity is the least for Stc\_180/550 which is in agreement with the XRD data.

Overall *h*/HTC gives rise to materials that are on one hand highly condensed and aromatic (from XRD, Raman, FT-IR and  $^{13}C$  ssNMR) but at the same time contain high amounts of hydrogen

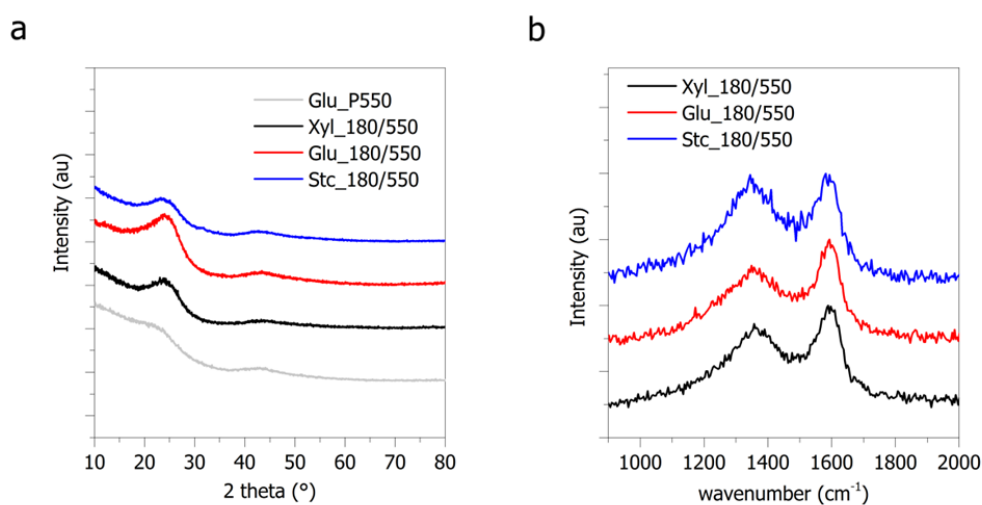


**Fig. 6.7 a) XRD diffractograms and b) Raman spectra of CBH\_180/550**

(from elemental analysis). These results seem contradicting because high degrees of aromatization should result in a loss of hydrogen atoms as well as oxygen atoms, as is observed when hydrothermal carbon after HTC at 180 °C is pyrolyzed at sufficiently high temperatures (*e.g.* at 900 °C). It is this carbonization and aromatization that renders pyrolyzed hydrothermal electronically conducting. However, electrical impedance spectroscopy showed that CBH\_180/550 samples had very low conductivities in the range of  $10^{-4}$  to  $10^{-5}$  S m<sup>-1</sup>. It was therefore concluded that *h*/HTC results in materials with highly aromatic domains which are not connected with each other, but ordered in a pseudo-aromatic fashion (presumably driven by  $\pi$ - $\pi$  stacking). Charge transport throughout the material is thereby inhibited, resulting in low conductivity. *h*/HTC therefore produces carbon materials that are different from both low temperature HTC but also from pyrolysis, a feature that is attributed to the SHV environment. As the temperature is increased to 550 °C various reactions such as dehydration and decarboxylation take place, as is the case in classical pyrolysis. Additionally, the SHV environment is expected to exert some catalytic effect on the carbonization process. scH<sub>2</sub>O molecules can “take part in the breakage and formation of bonds by significantly lowering the activation energy”.<sup>172</sup> Based on experimental observations, it is assumed that SHV exerts similar catalytic activity.

If xylose is treated hydrothermally at 180 °C for 18 h followed by a high temperature heating step at *ca.* 2 h, incomplete carbonization occurs as is evidenced by thermogravimetric analysis (TGA) (**Fig. 6.8a**, red curve). Two decomposition peaks can be seen rather than one, which is the case if the heating step at 550 °C is held for > 4 h (Xyl\_180/550 4h, black curve). Based on the assumption that SHV exerts a catalytic activity on the carbonization process, the first peak at 467 °C was assigned to a less carbonized particle core and the second peak at 500 °C was

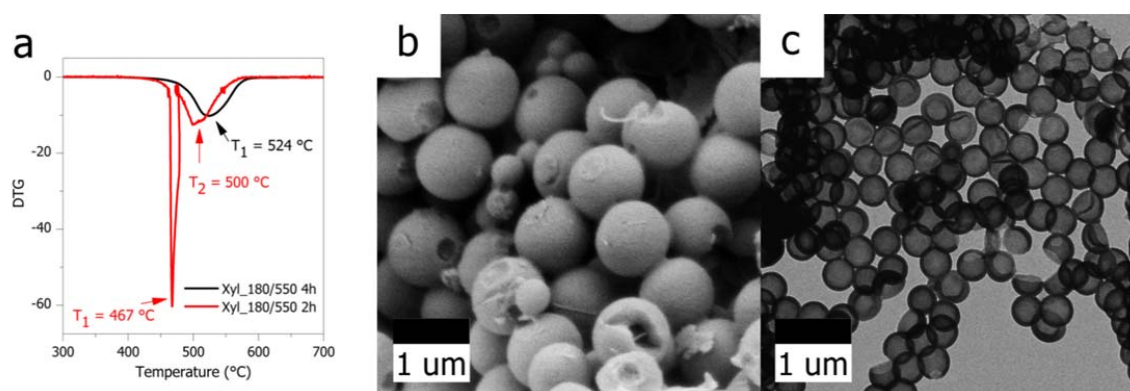


**Fig. 6.8** a) TGA of Xyl\_180/550 after 2 h at 550 °C in comparison with Xyl\_180/550 after 4 h at 550 °C. b) SEM and c) TEM image of Xyl\_180/550 (after 2 h) after calcination in air at 470 °C.



assigned to a more carbonized surface shell. The sample was then calcined under oxygen at the temperature of the lower decomposition peak. **Fig. 6.8b and c** show the results of this treatment. After calcination under oxygen the less carbonized core is burnt away leaving behind hollow spheres. It should however be noted that this experiment solely demonstrated the catalytic activity of SHV and is not suited for the large scale synthesis of hollow spheres. Firstly, the hollow sphere yield is extremely low (a few wt %) because the heterogeneous nature of the sample does not allow for homogeneous carbonization of all spheres. The temperatures at which the core or she shell decompose are broadly distributed which can be seen from the broad TGA peaks. Thirdly, calcination of the core must be carried out using extremely slow heating rates (9 h to reach the desired temperature) in order to avoid local temperature increases which would burn the carbon shells as well. A large scale and more controllable *h*HTC synthesis of carbon hollow spheres will be discussed in the next chapter.

## 6.4 Summary of chapter 6

Hydrothermal carbon microspheres were synthesized at 550 °C and  $p < 50$  bar. A two-step heating profile allowed for morphological control similar to *l*HTC conditions. A first heating step at 180 °C was used for morphology formation and a second heating step at 550 °C was used for further carbonization. The carbon microspheres obtained *via h*HTC were larger than those obtained *via l*HTC because the reaction conditions allowed access to organic side products which remain in solution during *l*HTC and do not carbonize. It was demonstrated that the carbon materials obtained *via h*HTC are distinct from those obtained *via l*HTC but also from low temperature hydrothermal carbon after pyrolysis at 550 °C. No difference in *h*HTC-derived material properties could be observed between pentoses and hexoses. The material obtained from a polysaccharide exhibited a slightly lower degree of carbonization but was otherwise similar to the monosaccharide derived samples. It was shown that in addition to thermally induced carbonization at 550 °C, the SHV environment exhibits a catalytic effect on the carbonization process. The resulting materials are chemically inert (*i.e.* they contain a negligible amount of reactive functional groups) and possess low surface area and electronic conductivity which distinguishes them from carbon obtained from pyrolysis. Compared to the materials presented in the previous chapters on chemical modifications of hydrothermal carbon, this makes them ill-suited candidates for electronic applications like lithium ion batteries or

electrocatalysts. It is therefore not possible to replace a second pyrolysis step of *h*HTC-derived carbons by *h*HTC if the purpose is to obtain conductive materials. However, *h*HTC derived materials could be interesting for applications that require chemical inertness but do not require specific electronic properties, *e.g.* filler materials for heat/sound insulating layers. The possibility to obtain such materials *via* a one-pot method rather than having to pyrolyze low temperature hydrothermal carbon, as well as the possibility to avoid high temperatures and inert conditions could make *h*HTC an attractive technique. One example of filler materials are hollow spheres or capsules that are already used as additives to paint to achieve acoustic and thermal insulation.

# 7 High temperature hydrothermal carbonization II

## A one pot synthesis of carbon hollow spheres

---

### 7.1 Introduction

The previous chapter showed that *h*/HTC results in inert, non-conductive carbon materials. While this excludes high-end energy-related applications which require specific electronic properties, these *h*/HTC derived materials may be interesting for applications where the physical structure, rather than the electronic or chemical properties are of importance. One potential application is the use of filler materials for improved acoustic and thermal insulation. Spherically shaped fillers are preferred over irregularly shaped fillers because they have lower surface area (resulting in lower resin demand) and the ability to roll past each other (which results in low impact on product viscosity). Hollow spheres are particularly interesting because they are light-weight and the internal voids are filled with stagnant air, which is a bad conductor of heat (heat transfer requires convection currents).<sup>177-179</sup> Coatings are usually manufactured on a weight basis and sold on a volume basis, making hollow fillers economically attractive to industry. Higher volume fillers additionally have the environmental benefit of reducing VOC (volatile organic compounds). Hollow glass micro spheres with low density (0.6 g/cc) and narrow particle size distribution can be used in flat wall paint. Commercial examples are the products Spherichel® by Potters industries LLC or 3M™ ceramic microspheres. These hollow borosilicate glass microspheres (available from 0.3 to 81 μm in diameter) are added to wall paints to achieve improved acoustic and thermal insulation. Thermoplastic microspheres are used as additive in coatings that help absorb impact or reduce damage (*e.g.* traffic coatings that need to withstand freeze-thaw cycles, space shuttle coatings). Limitations of glass microspheres are that their large size can influence the surface texture of the coating which results in gloss reduction, as well as breakage of the spheres during mechanic processing. Hollow carbon spheres in the submicron range would therefore be interesting candidates for coating additives.

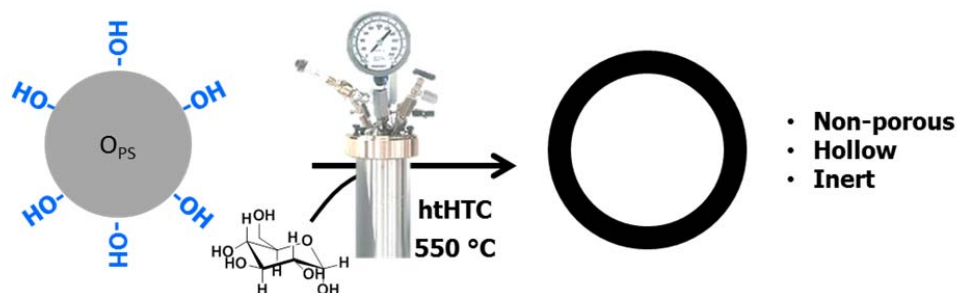


Fig. 7.1 graphical abstract of chapter 7

This chapter re-introduces the concept of carbon hollow sphere (**CHS**) formation *via* hard templating with polystyrene latex particles. It will be demonstrated that by using *htHTC* in a controlled fashion, the template removal step *via* pyrolysis can be eliminated (**Fig. 7.1**). A polystyrene latex/CHS dispersion was prepared to demonstrate the potential of using these materials as additives in water based coatings.

## 7.2 Experimental considerations

A polystyrene latex stabilized with 4-dodecylbenzenesulfonic acid (**SDBS**) surfactant was used as a sacrificial templating agent in the *htHTC* of glucose. 0.8 g of glucose were dissolved in 10 ml of a ~ 5 wt % aqueous latex dispersion. The mixture was placed in a quartz liner which was sealed into a Hastelloy C high pressure autoclave. From the previous chapter it is known that a two-step heating profile is required to obtain controlled product morphologies. Therefore, the mixture was first heated to 180 °C for 16 h as controlled coating step. Further carbonization was achieved by increasing the temperature to 550 °C for 4 h. The observed pressure varied between 50 to 60 bar for different experiments, *i.e.* the reaction took place in a superheated vapor environment (**SHV**, see **chapter 6**). The decomposition of polystyrene latex takes place at *ca.* 400 °C, *i.e.* the template is removed during *htHTC* at 550 °C and an additional pyrolysis step can be avoided. The sample was labeled CHS\_180/550. A reference sample was prepared based on the original method by White *et al.*, *i.e.* by hydrothermal treatment of a glucose/latex mixture at 180 °C for 16 h and subsequent pyrolysis at 550 °C under nitrogen for template removal. This sample was labeled **CHS\_P550**.

## 7.3 A one pot *h*HTC synthesis of carbon hollow spheres

### 7.3.1 Morphology, chemical composition and textural properties of the CHS

Transmission electron microscopy (TEM) images confirm successful *in situ* template removal (Fig. 7.2). The average diameter of the templates is 98 nm (Fig. 7.2a) which is much smaller than inner diameter,  $D_i = 127$  nm for CHS\_180/550 (Fig. 7.2b) but agrees well with  $D_i = 92$  nm for CHS\_P550 (Fig. 7.2c). Note that the slight decrease in  $D_i$  for CHS\_P550 compared to the template is due to contraction of the carbon framework during pyrolysis. Comparing the average shell thickness  $D_s$  of CHS\_180/550 (23 nm) and CHS\_P550 (17 nm) reveals that the *h*HTC derived samples also have a thicker shell in addition to the large diameter. What is the reason for this difference? The thicker shell for CHS\_180/550 can be explained by the fact carbonization is more efficient in SHV, where small organic molecules (side products of HTC) are broken down and can be added to the carbonized framework (*i.e.* the same reason why carbon microspheres are larger after *h*HTC than after *l*HTC treatment, see chapter 6). Concerning the larger inner diameter of CHS\_180/550, it could be argued that the increased reaction pressure causes expansion of the coated latex particles. However, the pressure is expected to be uniform and would hence similarly contract the coated particles. It was therefore postulated that the latex particles swell at higher temperatures due to the increasingly hydrophobic properties of water as it reaches 550 °C. Because the hydrothermal carbon layer formed at 180 °C is expected to be rather soft, it can expand with the swollen latex particles. Further carbonization in SHV then causes the carbon layer to rigidify as the template is

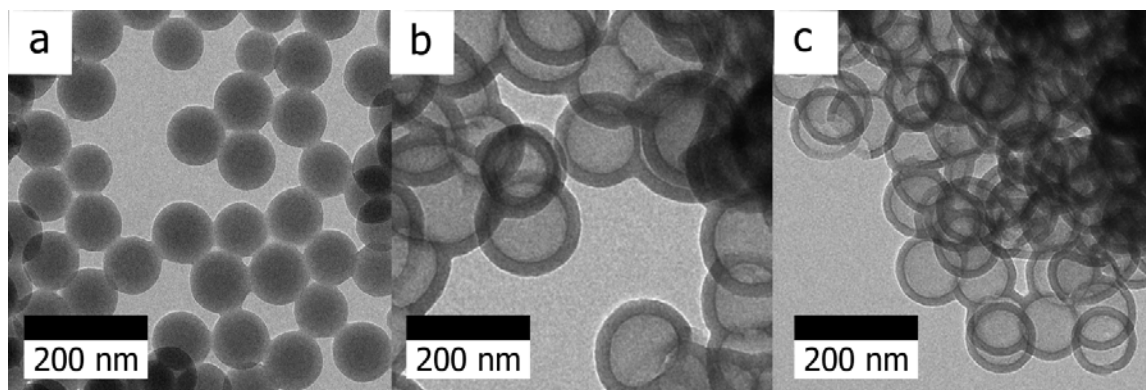


Fig. 7.2 TEM images of a) pure latex, b) CHS\_180/550 and c) CHS\_P550

**Table 7.1 Bulk elemental composition of the CHS after *h*HTC treatment at 550 °C as determined by elemental analysis. [NB: N<sub>2</sub> sorption-derived textural properties of the presented materials are shown on the right].**

Sample	Elemental composition (wt %)			Textural properties			
	C	H	O <sub>calc</sub>	S <sub>BET</sub> m <sup>2</sup> g <sup>-1</sup>	V <sub>total</sub> cm <sup>3</sup> g <sup>-1</sup>	D <sub>i</sub> nm	D <sub>s</sub> nm
CHS_180/550	93.8	3.4	2.8	30	0.14	127	23
CHS_P550	87.7	3.0	9.3	483	0.38	92	15

D<sub>i</sub> = average inner diameter of the CHS as determined from TEM images

D<sub>s</sub> = average shell thickness of the CHS as determined from TEM images

simultaneously removed.

The elemental composition of the CHS confirms a high degree of carbonization. As seen in the previous chapter, the *h*HTC derived materials have a larger carbon and lower oxygen content than *h*HTC materials pyrolyzed at 550 °C (**Table 7.1**). CHS\_180/550 exhibited very low specific conductivity in the range of 10<sup>-5</sup> S m<sup>-1</sup>, which is due to a structure where aromatic domains are not conjugated with each other but presumably connected *via* aliphatic moieties, as discussed in the previous chapter. Nitrogen sorption revealed a type IV H2 isotherm for CHS\_P550 (not shown), similar to the CHS presented in **chapter 4**, indicative of ink bottle shaped pores.<sup>135</sup> The “ink bottle” can be regarded as the hollow sphere cavity that is filled through narrow micropores (the “ink bottle neck”) in the CHS shell. The BET surface area was 568 m<sup>2</sup> g<sup>-1</sup>. In contrast, CHS\_180/550 exhibited a very low surface area of 30 m<sup>2</sup> g<sup>-1</sup> which is in the range of solid hydrothermal carbon microspheres. This means that the voids were not accessible to the adsorbate and that CHS\_180/550 presumably does not contain micropores in the carbon shell. This is in fact beneficial for their application as filler materials in coatings, because the resin cannot penetrate into the voids, leaving them filled with stagnant air.

### 7.3.2 Preliminary testing for the applicability of CHS as additives to insulating coatings

As a preliminary test for the feasibility of using *h*HTC derived CHS as additives in insulating coatings, ground CHS\_180/550 powder was dispersed in a polystyrene water based latex. The latex was prepared *via* a miniemulsion process as reported by Holtze.<sup>180</sup> The amounts of all reactants involved were the following: 24 g water, 0.074 g sodium dodecyl sulfate (**SDS**) surfactant, 6 g styrene monomer, 0.25 g hexadecane, 0.15 g V59 initiator and 0.01 g of

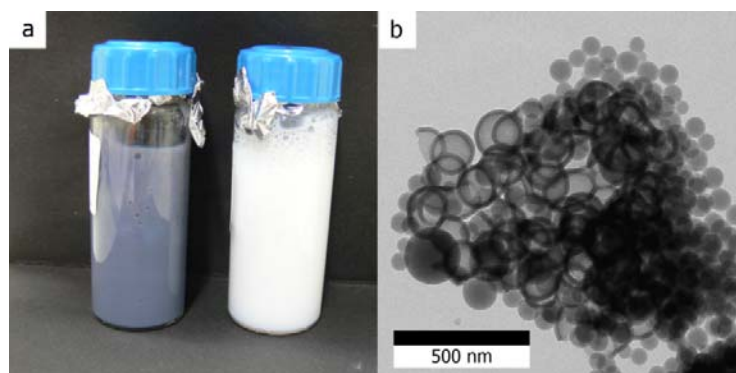


**Fig. 7.3** a) left: CHS\_180/550 in polystyrene latex. right: pure polystyrene latex. b) TEM image of CHS\_180/550 in polystyrene latex.

CHS\_180/550. The hydrophobic substances were mixed (styrene, CHS\_180/550, hexadecane and initiator) and added to the SDS in water. The mixture was emulsified by stirring for 1 h at 1000 rpm and then ultrasonicated for  $\sim 5$  min using a high power ultrasound device. Polymerization was then carried out at 70 °C for 20 h (without stirring).

The result was a stable, grey latex as shown in **Fig. 7.3a** (a reference of a control experiment without addition CHS\_180/550 is shown on the right). TEM analysis shows that the monomer does not penetrate into the hollow sphere voids and the latex particles are formed around CHS\_180/550. Any insulating properties should therefore be retained.

## 7.4 Summary of chapter 7

A one pot synthesis of carbon hollow spheres using polystyrene latex particles as hard templates was presented. Template removal occurred *in situ* in the *ht*HTC system which in that regard is advantageous over the originally reported method by White *et al.*, who carried out HTC at 180 °C and then pyrolyzed the product at 550 °C to induce latex decomposition and template removal. The *ht*HTC derived CHS were larger than CHS obtained *via* the original method, which was attributed to swelling of the polystyrene core as water becomes more apolar. Because carbon obtained *via ht*HTC is non-conductive and chemically inert, the obtained CHS are envisaged for applications which do not require specific electronic properties, such as filler materials. Preliminary tests showed that the CHS could be dispersed in an aqueous polystyrene latex without monomer penetrating into the hollow sphere voids. This leaves the stagnant air inside the CHS intact which in turn is promising for their application in heat and sound insulating coatings.

# 8 Summary, Conclusions, Outlook

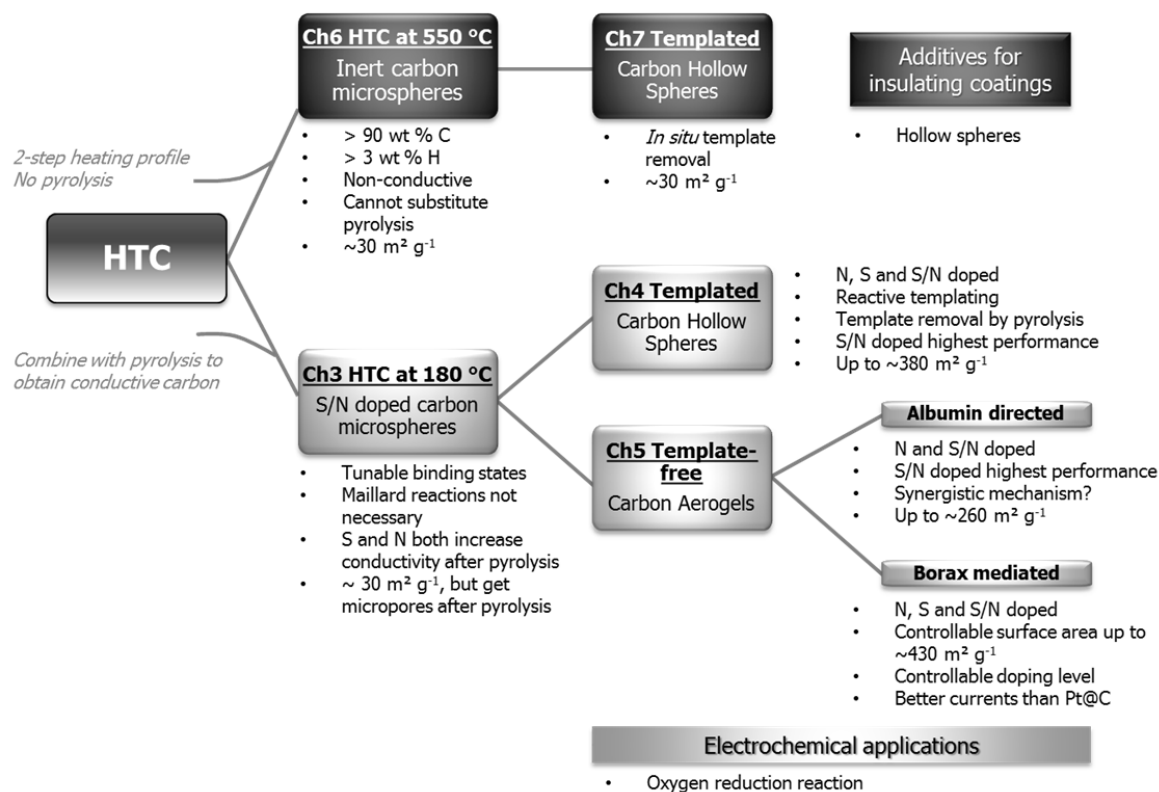


**Fig. 8.1 Schematic overview of main results obtained in this thesis**

The underlying motivation for the work carried out for this thesis was the ever-growing need to reduce the dependence on fossil fuels and move towards more sustainable technologies. The aim was to synthesize a “palette” of functional nanomaterials using the established technique of hydrothermal carbonization (HTC). With this, it was demonstrated that HTC, a simple and sustainable technique for carbon material formation, is a viable and powerful addition to the toolbox of carbon-based technologies. Two main strategies were used to modify the materials obtained by HTC of glucose, a model precursor representing biomass (**Fig. 8.1**). The first approach was the introduction of heteroatoms, or “doping” of the carbon framework. Sulfur was for the first time introduced as a dopant in hydrothermal carbon.

After a thorough review of scientific literature to summarize the main reaction pathways through which heteroatoms may be incorporated into hydrothermal carbon (**chapter 2**), the synthesis of S and S/N doped microspheres was presented in **chapter 3**. It was shown that the mechanisms



assumed in chapter 2 could be manipulated to influence the binding state of sulfur by varying the type of sulfur source as well as the pyrolysis temperature. If sulfur is bound aromatically in the precursor (*e.g.* thienyl-cysteine, **TCys** or 2-thienyl-carboxaldehyde, **TCA**), it is most likely incorporated *via* cycloaddition or EAS reactions which leave the aromatic ring intact in the product. In contrast, aliphatically bound sulfur (*e.g.* L-cysteine, **Cys** or 3-mercapto propionic acid, **MPA**) may be incorporated *via* nucleophilic substitution or Michael addition reactions and therefore more likely result in aliphatic binding motifs (thiol ether) in the HTC product. Post pyrolysis results in more stable, aromatic binding states as the temperature is increased from 550 °C to 900 °C due to thermal rearrangements of the carbonaceous framework. Importantly, the presence of aromatic binding states in the as-synthesized hydrothermal carbon allows for higher heteroatom retention levels after pyrolysis and hence more efficient use of dopant sources. In this regard, HTC may be considered as an “intermediate” step in the formation of conductive heteroatom doped carbon for electronic applications. Both nitrogen and sulfur act to increase the conductivity of the doped carbon material after pyrolysis.

**Chapters 4 and 5** aimed at introducing high surface area and defined nano-architectures which are important for electrochemical applications. The first approach (**chapter 4**) built on a hard templating approach using the established polystyrene latex templating, developed by White *et al.* Sulfur doped carbon hollow spheres (**CHS**) could be synthesized by adding MPA to the original glucose/latex HTC mixture. A reactive templating approach was further developed to obtain nitrogen doped CHS, by exchanging the originally hydroxyl-terminated latex with amino-functionalized latex. The nitrogen was partially retained upon template removal. S/N dual doped CHS could be obtained by a combination of the two doping strategies. Electrochemical testing of the doped CHS revealed that the solely sulfur or nitrogen doped CHS did not exhibit improved performance over an undoped control. This was attributed to unfavorable surface areas and mass transport properties which could not be compensated for by the low doping levels (1.3 to 2.5 wt %). However, the S/N dual doped CHS showed the best catalytic performance despite the lowest surface area out of all tested samples. This was the first indicator that S/N dual doped carbons obtained *via* HTC could have drastically improved properties as catalysts in the ORR. Increasing the doping levels and testing the doped CHS for more suitable applications such as anode materials in lithium ion batteries are topics to be addressed in future work.

**Chapter 5** aimed at introducing surface area without the use of templates, which is favored in terms of atom economy. Two established hydrothermal approaches for the synthesis of organic/carbon aerogels were used as basis. Firstly, the albumin-directed formation of nitrogen-doped carbon aerogels from glucose (developed by White *et al.*)<sup>63</sup> was extended to include the incorporation of sulfur. TCys or TCA were thereby added to the original glucose/ovalbumin recipe. Electrochemical testing showed that S/N dual doped carbon aerogels exhibited superior catalytic performance in the ORR compared to solely nitrogen doped carbon aerogels in both acidic and basic media. A synergistic mechanism between nitrogen and sulfur dopants was proposed, whereby nitrogen directly or indirectly (*via* the adjacent carbon atom) aids O<sub>2</sub> dissociation and sulfur facilitates proton transfer. Future investigations are required to confirm the presented hypothesis. If it proves to be correct, this work provides new parameters which can be adjusted to optimize catalyst performance. Secondly, aerogels were synthesized by an extension of the borax-mediated formation of carbonaceous aerogels from glucose (developed by Fellingner *et al.*). It was possible to successfully introduce nitrogen and/or sulfur as dopants. 2-pyrrol-carboxaldehyde (**PCA**) and 2-methyl-thiophene (**MTP**) were thereby simply added to a borax/glucose solution and hydrothermally treated at 180 °C. It was shown that both the particle size (and hence surface area) and the nitrogen content can be tuned by varying the amounts of borax or PCA used. The MTP system could be similarly influenced, although the accessible amount of sulfur doping was lower than for nitrogen (< 3 wt % for S as opposed to > 6 wt % for N). Electrochemical testing of the carbon aerogels as catalysts in the oxygen reduction reaction showed that catalytic activity increases with higher surface area and with higher nitrogen content. By adjusting the amount of borax and PCA, a carbon aerogel with both high nitrogen content and high surface areas was engineered to maximize catalytic performance. The obtained sample exhibited drastically improved current densities compared to a platinum catalyst (but lower onset potential), as well as excellent long term stability. Koutecky-Levich analysis indicated that the selectivity tended towards an ideal 4-electron process which is desirable for fuel cell operation. This nitrogen doped carbon aerogel represents the first sustainable, scalable and non-metal material to partially outperform platinum catalysts in the ORR. S and S/N doped gels showed lower performance than solely N doped gels, although optimization of the S/N ratio and doping levels was not carried out and presents an interesting future project.

Although not addressed in this thesis, the doped carbon materials without further pyrolysis are also attractive candidates for applications in sorption and chromatography, where the ability to influence the type of functional group incorporated would be highly advantageous.

**Chapter 6** provided the basis for the second “physical” approach taken to produce useful carbon materials *via btHTC*. Xylose, glucose and starch were used as model compounds (representing pentoses, hexoses and polysaccharides, respectively) and treated hydrothermally at 550 °C and < 50 bar, *i.e.* under superheated vapor (SHV) conditions. It was shown that morphological control is possible if a two-step heating profile was used. “Conventional” HTC (*lHTC*) was carried out at 180 °C for 18 h for controlled morphology formation (microspheres in this case) after which the temperature was increased to 550 °C for further carbonization. The carbon microspheres obtained *via btHTC* were larger than those obtained *via lHTC* because the reaction conditions allowed access to organic side products which remain in solution during *lHTC* and do not carbonize. It was demonstrated that the carbon materials obtained *via btHTC* are distinct from those obtained *via lHTC* and subsequent pyrolysis at 550 °C. No difference in *btHTC*-derived material properties could be observed between pentoses and hexoses. The material obtained from a polysaccharide exhibited a slightly lower degree of carbonization but was otherwise similar to the monosaccharide derived samples. It was shown that in addition to thermally induced carbonization at 550 °C, the SHV environment exhibits a catalytic effect on the carbonization process. The resulting materials are chemically inert (*i.e.* they contain a negligible amount of reactive functional groups) and possess low surface area and electronic conductivity which distinguishes them from carbon obtained from pyrolysis. Compared to the materials presented in the previous chapters on chemical modifications of hydrothermal carbon, this makes them ill-suited candidates for electronic applications like lithium ion batteries or electrocatalysts. It is therefore not possible to replace a second pyrolysis step of *lHTC*-derived carbons by *btHTC* if the purpose is to obtain conductive materials. However, *btHTC* derived materials could be interesting for applications that require chemical inertness but do not require specific electronic properties, *e.g.* light weight filler materials for heat/sound insulating layers.

This was the topic of **chapter 7** in which the latex hard templating approach from **chapter 4** was revisited to synthesize carbon hollow spheres. However, by using *btHTC* it was possible to carry out template removal *in situ* because the second heating step at 550 °C was above the polystyrene latex decomposition temperature. The thus obtained, *btHTC* derived CHS were larger than CHS obtained *via* the original method, which was attributed to swelling of the

polystyrene core as water becomes more apolar. Preliminary tests showed that the CHS could be dispersed in an aqueous polystyrene latex without monomer penetrating into the hollow sphere voids. This leaves the stagnant air inside the CHS intact which in turn is promising for their application in heat and sound insulating coatings. The possibility to obtain such materials *via* a one-pot method rather than having to pyrolyze low temperature hydrothermal carbon, as well as the possibility to avoid high temperatures and inert conditions could make *ht*HTC an attractive technique for sustainable technologies, such as to synthesize materials for more energy efficiency in buildings.

Overall the work carried out in this thesis represents a noteworthy development in demonstrating the great potential of sustainable carbon materials. The incredible diversity of HTC was demonstrated together with small but steady advances in how HTC can be manipulated to tailor material properties for specific applications. Future optimization of the herein presented materials and detailed deconvolution of the complex HTC mechanism are necessary. However, it is highly likely that HTC derived carbon based materials will ultimately overcome current favoured fossil-based materials and in that way contribute to more sustainable technologies.

# 9 Appendix

---

## 9.1 Experimental Methods

### 9.1.1 Experimental procedures

#### 9.1.1.1 Chemicals

D-(+)-glucose (Glu) and D-(+)-xylose (Xyl) were purchased from Roth chemicals. Starch (soluble, Stc) was purchased from ABCR GmbH & Co. KG. Borax (SIGMA grade) was purchased from SIGMA. 2-thienyl-carboxaldehyde (TCA), 2-pyrrol-carboxaldehyde (PCA), 2-thiophene-carboxylic acid (TCAcid) and 2,5-thiophene-dicarboxaldehyde (TDCA), 3-mercaptopropionic acid (MPA) and lyophilized Albumin powder (from chicken egg white) were purchased from Aldrich. 2-methyl-thiophene (MTP) and 2,5-dimethyl-thiophene (DMT) were purchased from Alfa Aesar. All chemicals were used as received. Functionalized polystyrene latexes were kindly prepared and supplied by Ursula Lubahn at the Max Planck Institute of Colloids and Interfaces.

#### 9.1.1.2 General procedure for hydrothermal carbonization at 180 °C

The solution containing all reactants was filled into a glass inlet which was then placed in a Teflon lined, stainless steel autoclave (45 ml volume, purchased from Parr Instruments). The autoclave was placed in a pre-heated furnace at 180 °C for **X h** after which it was allowed to cool down to room temperature. The solid product was collected by filtration and washed three times with approx. 150 ml H<sub>2</sub>O and EtOH (or until the solution ran clear) before drying in vacuo at 70 °C overnight. (Note: In order to exclude any contributions from physisorbed molecules on the surface of the materials, Soxhlet extraction was performed on various samples (*e.g.* Cys0.2 and TCys0.2 in chapter 3.3) and the values for elemental analysis compared to those obtained from the same samples by washing with EtOH until the filtrate ran clear. Since the results were almost identical, the time consuming Soxhlet extraction step was no longer carried out for any of the products obtained in this work.)

### 9.1.1.3 Generalized procedure for pyrolysis

The dried powder sample was placed in a ceramic crucible and covered with a ceramic lid. The crucible was placed in a nitrogen atmosphere furnace and flushed for 30 minutes before heating to the final **temperature Y** (550 °C or 900 °C) at a heating rate of 10 K min<sup>-1</sup>. The final temperature was kept for 4 h after which the furnace was allowed to cool down to room temperature. The obtained black powders were characterized without further purification.

## Chapter 2

For each control experiment, 0.2 g of the corresponding heteroatom source were added to 1.5 g of glucose dissolved in 18.0 g of double distilled H<sub>2</sub>O. The mixture was then hydrothermally treated at 180 °C as described above with **X = 18 h**.

## Chapter 3

In a typical experiment 1.5 g of Glu and Z g (Z = 0.1, 0.2, 0.3 or 0.4) of Cys, TCys, MPA or TCA were dissolved in 13.5 g of double distilled H<sub>2</sub>O. Hydrothermal Carbonization at 180 °C was carried out with **X = 5.5 h** for Cys and TCys containing samples, and with **X = 18 h** for MPA and TCA containing samples.

The samples were pyrolyzed at either **Y = 550 °C** or **Y = 900 °C**.

## Chapter 4

**Undoped control.** 0.8 g of Glu were added to 10 ml of a ~ 5 wt % O<sub>PS</sub> latex dispersion and hydrothermally treated at 180 °C with **X = 18 h**. Template removal was achieved by pyrolysis at **Y = 900 °C**.

**Sulfur doped CHS.** 0.8 g of Glu and 0.1 g MPA were added to 10 ml of a ~ 5 wt % O<sub>PS</sub> latex dispersion and hydrothermally treated at 180 °C with **X = 18 h**. Template removal was achieved by pyrolysis at **Y = 900 °C**.

**Nitrogen doped CHS.** 0.8 g of Glu were added to 10 ml of a ~ 5 wt % N<sub>PS</sub> latex dispersion and hydrothermally treated at 180 °C with **X = 18 h**. Template removal was achieved by pyrolysis at **Y = 900 °C**.

**Sulfur and nitrogen doped CHS.** 0.8 g of Glu and 0.1 g MPA were added to 10 ml of a ~ 5 wt % N<sub>PS</sub> latex dispersion and hydrothermally treated at 180 °C with **X = 18 h**. Template removal was achieved by pyrolysis at **Y = 900 °C**.

## Chapter 5

### 1) Albumin directed aerogel formation

1.5 g Glu and 0.3 g ovalbumin were dissolved in 13.5 g distilled water. For the sulfur doped aerogels, 1 mmol of the sulfur source (0.2 g for TC and 0.1 g for TCA) was added to the mixture. The solution was hydrothermally treated at 180 °C with **X = 5.5 h (without the drying step)**. After washing the resulting hydrothermal monoliths were washed with excess water and ethanol, supercritical CO<sub>2</sub> drying was carried out to yield a low density carbonaceous aerogel. Pyrolysis was carried out at **Y = 900 °C**.

### 2) Borax mediated aerogel formation

6.0 g of Glu and Z g of Borax (Z = 150 mg, 300 mg or 600 mg) were dissolved in 14.0 g of double distilled H<sub>2</sub>O. For an undoped control, a mixture with Z = 300 mg was hydrothermally treated at 180 °C with **X = 18 h (without the drying step)**.

**Nitrogen doped aerogels.** Z' g of PCA (Z' = 0.8 g, 1.3 g or 2.0 g) were added to the above reaction mixture and hydrothermally treated at 180 ° with **X = 18 h (without the drying step)**.

**Sulfur doped aerogel.** 0.5 g MTP was added to the above reaction mixture containing 600 mg of Borax and hydrothermally treated at 180 °C with **X = 18 h (without the drying step)**.

**Sulfur and nitrogen doped aerogel.** 0.7 g MTP and 1.3 g PCA were added to the above reaction mixture containing 600 mg of Borax and hydrothermally treated at 180 °C with **X = 18 h (without the drying step)**.

All gels were dried using supercritical CO<sub>2</sub> to maintain the delicate nanostructure. Pyrolysis was carried out at **Y = 900 °C**.

## Chapter 6

1.0 g of Glu, Xyl or Stc was dissolved in 10.0 g of double distilled H<sub>2</sub>O. The solution was placed into a quartz inlet which was then sealed into a Hastelloy C high pressure autoclave equipped with a heating mantle, thermocouple and pressure gauge (75 ml volume, purchased from Parr

Instruments). The solution was heated to 180 °C using the “fast heating” setting. The temperature was kept at 180 °C for 18 h and then increased to 550 °C and kept at that temperature for 4 h. The observed pressures were usually in the range of 10 to 50 bar. After letting the autoclave cool down to room temperature, one of the pressure valves was opened to release any excess pressure. The solid product was then collected by filtration and washed several times with distilled water and ethanol. The samples were dried *in vacuo* at 70 °C overnight.

## Chapter 7

0.8 g of Glu was added to 10 ml of a ~ 5 wt % O<sub>PS</sub> latex dispersion. High temperature hydrothermal carbonization was carried out as described for chapter 6, except that the second heating step was carried out at the “slow heating” setting in order to avoid overheating at the latex decomposition temperature (*ca.* 400 °C) during *in situ* template removal.

### 9.1.2 Sample Characterization

#### Scanning electron microscopy (SEM)

SEM was performed using a Gemini Leo-1550 instrument (acceleration voltage 0.1 to 30 kV). Samples were prepared by loading the ground powder samples onto carbon tapes and sputtering with Au/Pd.

#### Transmission electron microscopy (TEM)

TEM was carried out with a Carl Zeiss Omega 912X at an acceleration voltage of 120 kV. Samples (disperse in ethanol) were prepared by drop deposition onto copper grids coated with amorphous carbon.

#### High resolution transmission electron microscopy (HRTEM)

HRTEM measurements were carried out by **Sören Selve** at the **TU Berlin** using a TECNAI G<sup>2</sup> 20 S-TWIN equipped with an LaB<sub>6</sub> electron gun operating at 200 kV. Samples were prepared by dry deposition of the material onto holey carbon copper grids.



**Analytical TEM** was performed by **Marc Willinger** at the **FHI Berlin** using a Philips CM 200 microscope with a field emission gun operated at 200kV.

### **<sup>13</sup>C solid state magic angle spinning nuclear magnetic resonance (<sup>13</sup>C MAS ssNMR)**

<sup>13</sup>C MAS ssNMR spectra were acquired on a Bruker Avance 300 MHz (7T) spectrometer using 4mm zirconia rotors as sample holders, spinning at MAS rate of 14 kHz. The chemical shift reference was tetramethylsilane (TMS  $\delta = 0$  ppm). <sup>1</sup>H  $t_1$  relaxation time was set to 3 s. Proton-to-carbon CP MAS was used to enhance carbon sensitivity with a cross polarization time equal to 1 ms.

### **Elemental Analysis (EA)**

EA measurements were carried out using a Vario El elemental analyzer for the detection of the elements C, H, N, S. The wt % of oxygen was calculated.

### **X-Ray photoelectron spectroscopy (XPS)**

XPS analysis of the samples was performed using a Thermo Scientific K $\alpha$  ESCA instrument equipped with Al K $\alpha$ 1, 2 monochromatized radiation at 1486.6 eV X-ray source. Charge neutralization was performed by using both a low energy flood gun (0 to 14 eV) and a low energy Ar ion gun. The XPS measurements were carried out using monochromatic Al-K $\alpha$  radiation ( $h\nu = 1486.6$  eV). Photoelectrons were collected at 90° to the sample surface. A constant analyzer energy mode (CAE) with 100 eV pass energy for survey spectra and 20 eV pass energy for high resolution spectra was used. The spectra were calibrated by setting the C1s photo peak at 285.0 eV. For sulfur, the S2p<sub>3/2</sub> peak was used for the assignment of binding states. Surface elemental composition was determined using standard Schofield photoemission cross sections. Peak assignments were carried out by using the values reported in the NIST XPS Database and references indicated in the text.

### **Electrochemical analysis**

**Specific conductivity measurements** were carried out with Gamry Reference 600/3000 potentiostat (Gamry Instruments) and Gamry EIS 300/Physical Electrochemistry software.

Electrical conductivity was achieved applying R-model on potentiostatic impedance spectroscopy at 1-1000 Hz using a two electrode setup.

To perform **electrochemical testing** a standard ink was prepared from ~5 mg of catalyst with 95  $\mu\text{l}$  Nafion® binder solution and 350  $\mu\text{l}$  of ethanol. The ink was ultrasonicated for at least 30 minutes for homogenization. A 5  $\mu\text{l}$  aliquot was dropped onto a freshly polished glassy carbon rotating disk electrode (diameter ~ 5 mm, electrode area 0.196  $\text{cm}^2$ ) to prepare a catalyst thin film. When necessary, the electrode was warmed to ~ 50 °C in an oven prior to ink application in order to achieve better electrode coverage of the catalyst film. Electrochemical tests were performed in 0.1 M KOH or 0.1 M HClO<sub>4</sub> in a standard three - electrode setup with an Ag / AgCl reference electrode using Gamry Reference 600 potentiostat (Gamry Instruments) and Gamry EIS 300/Physical Electrochemistry software. The obtained current values were normalized to the mass of the catalyst used (*i.e.* given in  $\text{mA mg}^{-1}$ ) for direct comparison between samples. For **Koutecky-Levich analysis** (refer to **chapter 2.2.2**), the un-normalized currents obtained from measurements at varying rotation rates (600, 1000, 1600, 2000, and 2600 rpm) were used.

### **Fourier-transform infrared spectroscopy (FT-IR) and Raman spectroscopy**

FT-IR spectra were recorded using a Varian600 FT-IR spectrometer. KBr pellets were pressed containing the ground powder samples.

Raman spectra were recorded using a WiTec Confocal Raman Microscope R-300 instrument. A green Nd/YAG laser ( $\lambda = 532 \text{ nm}$ ) was used with an intensity of 1 mW (objective: 20x).

### **Thermogravimetric Analysis (TGA)**

TGA was carried out using a NETZSCH TG 209 from 0 °C to 1000 °C at a heating rate of 10 K  $\text{min}^{-1}$  under O<sub>2</sub>.

### **Gas Sorption Analysis**

Gas sorption analysis for the determination of carbon surface areas and pore size distributions were measured by nitrogen adsorption and desorption at 77 K using Autosorb 1MP or Quadrasorb Kr/MP machines (Quantachrome Instruments). Carbon dioxide sorption isotherms were collected at 273 K using the same device. High purity gases were used. Data evaluation was

performed using the AS1Win Software from Quantachrome Instruments. Surface area was determined using the Brunauer-Emmet-Teller (BET) model ( $N_2$ , assuming carbon adsorbent with slit pores) or the Non-linear density functional theory (NLDFT) method ( $CO_2$ , assuming carbon adsorbent with slit pores). Pore size distributions (PSD) and pore volumes were derived from the adsorption branches using Quenched Solid Density Functional Theory (QSDFT), as this evaluation model takes into account the effects of surface roughness and chemical heterogeneity of the material surfaces. Before analysis, samples were degassed at 60 °C (as synthesized hydrothermal carbon) or at 150 °C (pyrolyzed hydrothermal carbon) for 20 h using a “Masterprep” degassing system.

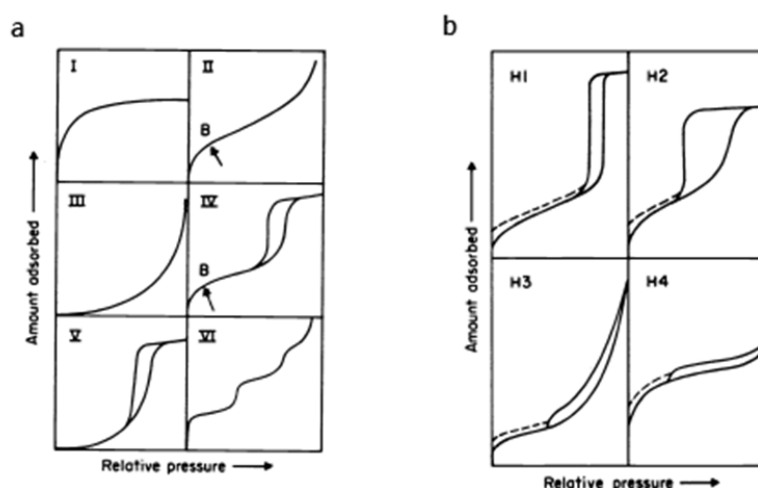


Fig. 9.1 a) types of isotherms and b) types of hysteresis loops.

The isotherm shapes discussed in this thesis are Type IV H3 and Type IV H2 isotherms so only these are discussed here (Fig. 9.1). For a detailed explanation about different sorption isotherms by IUPAC classification, refer to Sing *et al.*<sup>135</sup>

- Characteristic features of the **Type IV isotherm** are its hysteresis loop, which is associated with capillary condensation taking place in mesopores, and the limiting uptake over a range of high  $p/p^0$ . The initial part of the Type IV isotherm is attributed to monolayer-multilayer adsorption.
- **Type H2 loops** are characteristic of pore size and shapes that are not well-defined. The H2 loop is especially difficult to interpret but often attributed to a difference in mechanism between condensation and evaporation processes occurring in pores with narrow necks and wide bodies (often referred to as 'ink bottle' pores).

- The **Type H3 loop**, which does not exhibit any limiting adsorption at high  $p/p^\circ$ , is observed with aggregates of plate-like particles giving rise to slit-shaped pores.

### X-Ray diffraction (XRD)

XRD patterns were recorded on a Bruker D8 Advance diffractometer equipped with Cu-K $\alpha$  radiation ( $\lambda = 0.154$  nm) monochromized using a multilayer Glöbel mirror. The X-Ray gun was operated at 40 kV and 40 mA. Diffractograms were recorded over the  $2\theta$  range of 5 to  $80^\circ$  using a scan rate of  $1^\circ \text{ min}^{-1}$ . Ground powder samples were placed on silicon sample holders for measurement.

## 9.2 Supplementary information

### Chapter 3

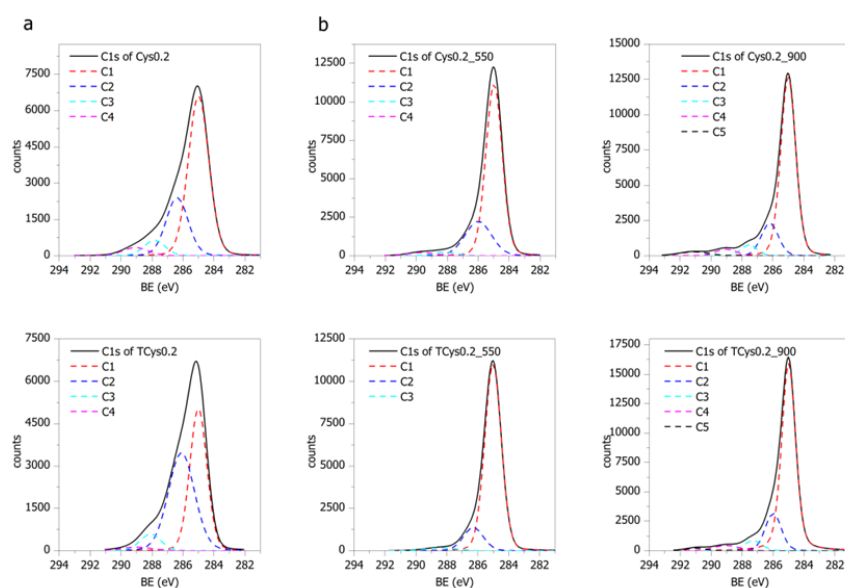


Fig. A 1 Deconvoluted high resolution XPS of the C 1(s) photoelectron envelopes for Cys0.2 and TCys0.2 after hydrothermal treatment at 180 °C and after pyrolysis at 550 °C and 900 °C.

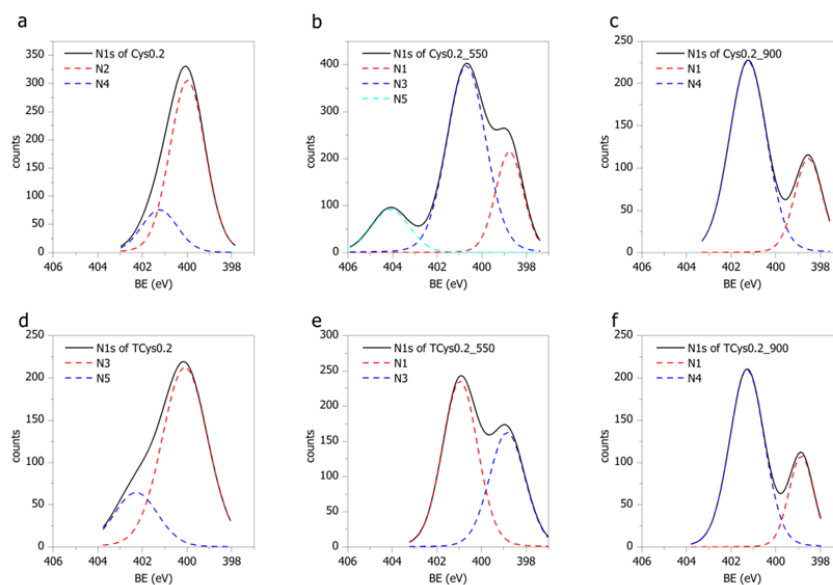


Fig. A 2 Deconvoluted high resolution XPS of the N 1(s) photoelectron envelopes for Cys0.2 and TCys0.2 after hydrothermal treatment at 180 °C and after pyrolysis at 550 °C and 900 °C.

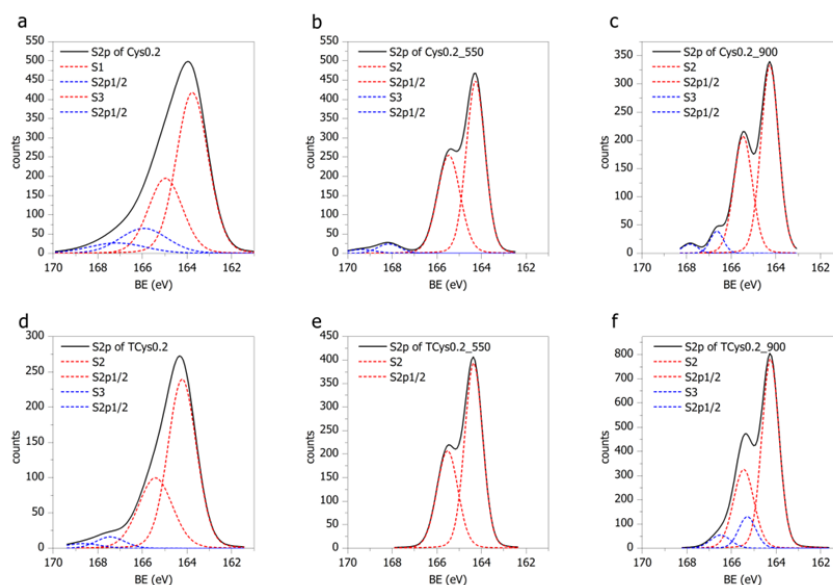


Fig. A 3 Deconvoluted high resolution XPS of the S 2(p) photoelectron envelopes for Cys0.2 and TCys0.2 after hydrothermal treatment at 180 °C and after pyrolysis at 550 °C and 900 °C.

## Chapter 4

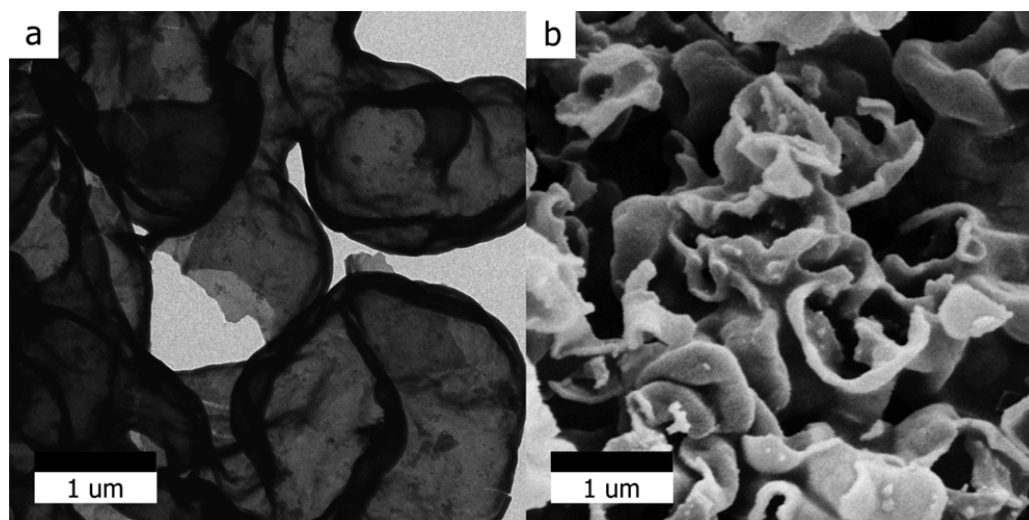


Fig. A 4 a) TEM and b) SEM image of  $O_{PS}$ -Cys after template removal at 550 °C. Elemental analysis shows an elemental composition of 84.4 wt % C, 2.7 wt % H, 3.4 wt % N and 1.9 wt % S.

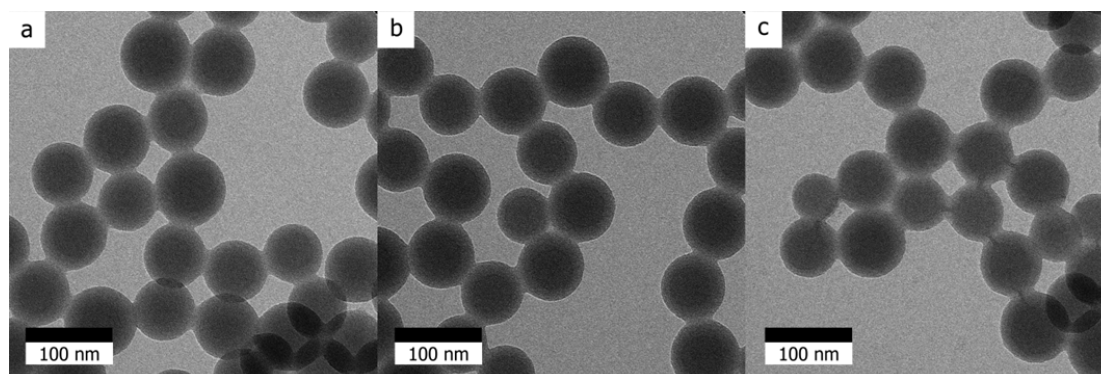


Fig. A 5 TEM images of a)  $O_{PS}$ \_latex, b)  $O_{PS}$ \_latex after HTC at 180 °C and c)  $O_{PS}$ \_latex + MPA after HTC at 180 °C.

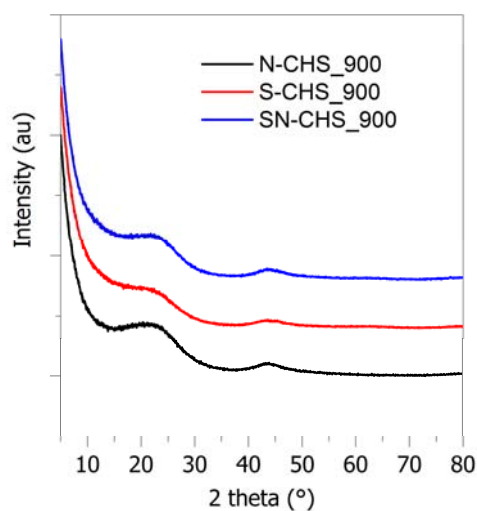


Fig. A 6 X-Ray diffractograms of nitrogen, sulfur and sulfur/nitrogen dual doped CHS.

## Chapter 5

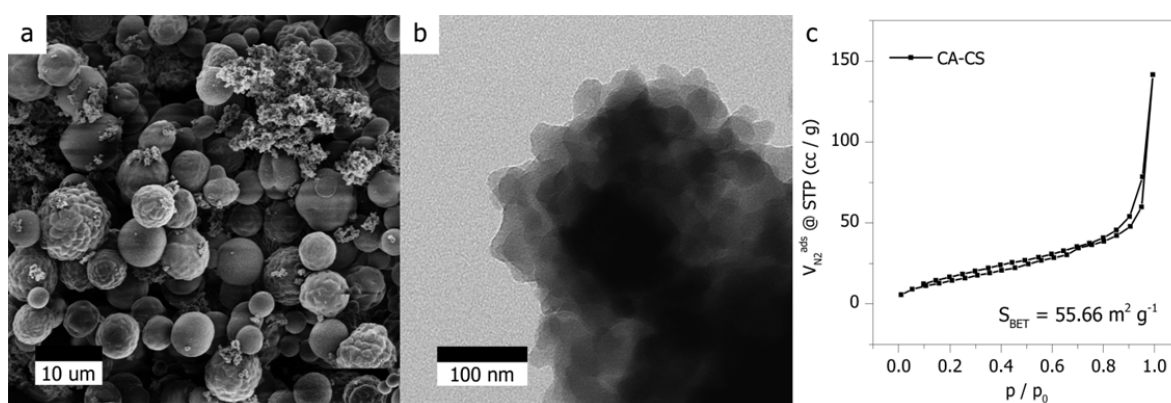


Fig. A 7 a) SEM and b) TEM image of solid product obtained with cysteine after HTC at 180 °C. A heterogeneous morphology is obtained, implying that the controlled gel formation is hindered by addition of cysteine. c) nitrogen sorption isotherm for CA-CS, showing the low surface area of the material.

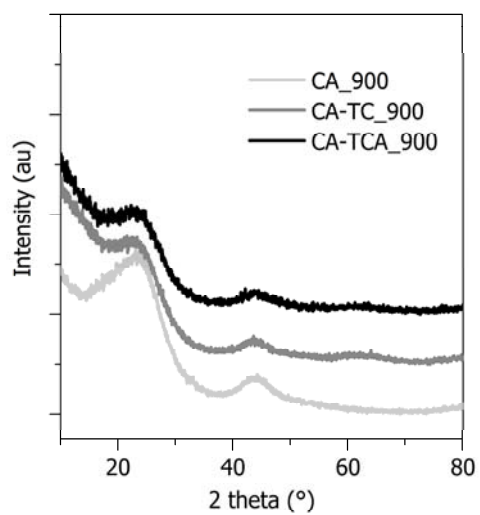


Fig. A 8 X-Ray diffractograms of pyrolyzed carbon aerogels

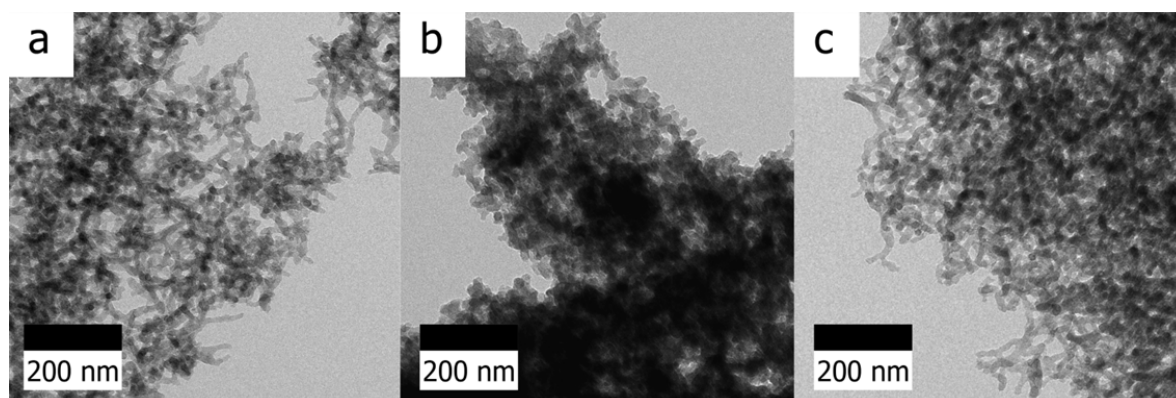


Fig. A 9 TEM images of a) CA\_900, b) CA-TC\_900, and c) CA-TCA\_900



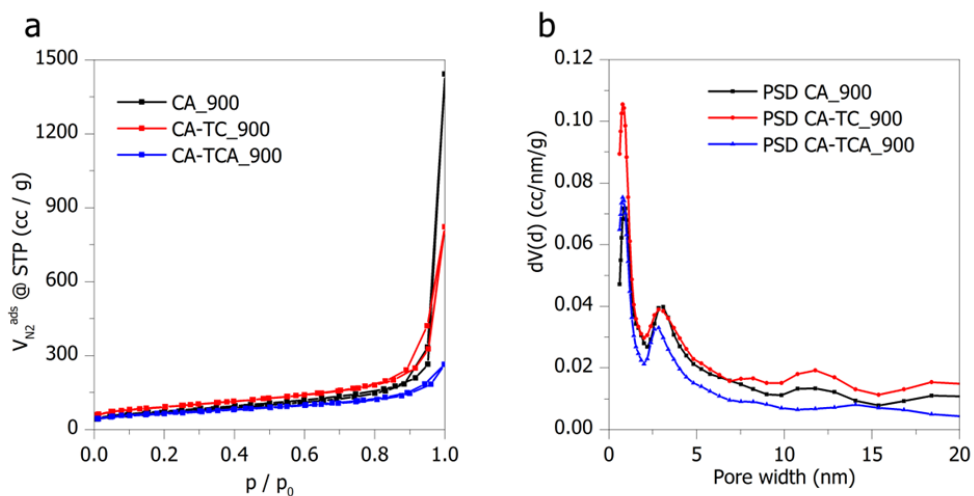


Fig. A 10 a) Nitrogen sorption isotherms and b) pore size distributions (QSDFT model) obtained for aerogels after HTC at 180 °C.

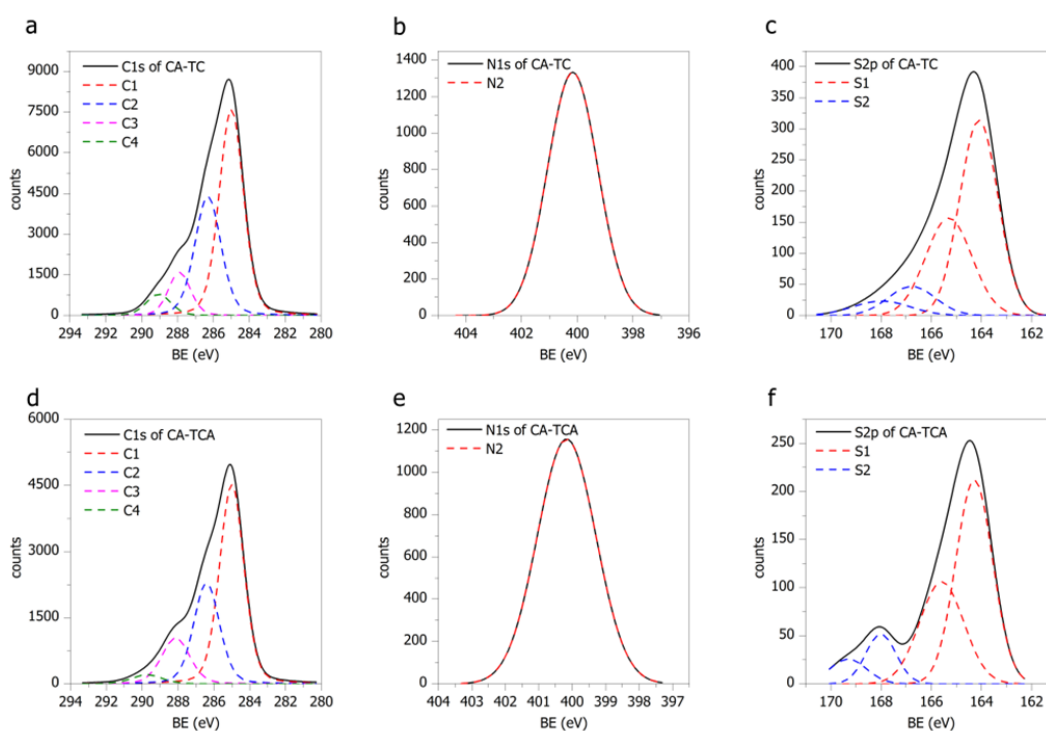


Fig. A 11 Deconvoluted C1(s) N1(s) and S2(p) photoelectron envelopes of CA-TC (a, b, c, respectively), and CA-TCA (d, e, f, respectively)

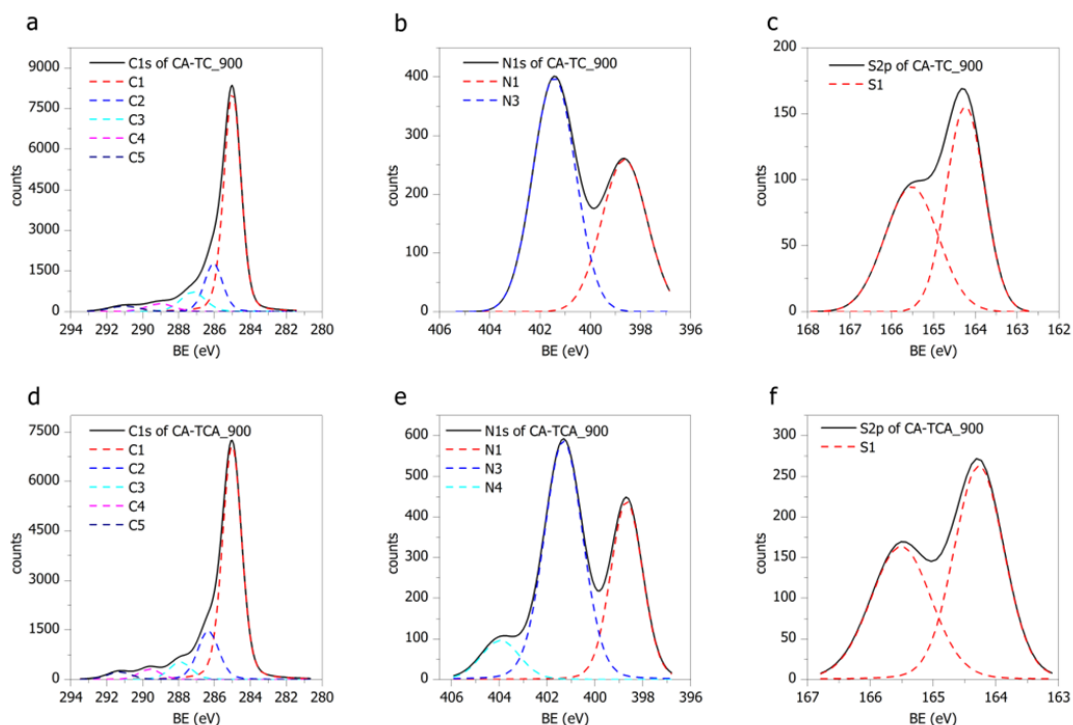


Fig. A 12 Deconvoluted C1(s) N1(s) and S2(p) photoelectron envelopes of CA-TC\_900 (a, b, c, respectively), and CA-TCA\_900 (d, e, f, respectively)

Table A 1 Peak assignments for the the C1(s) and N 1(s) photoelectron envelopes for PCA1\_300mg and PCA1\_300mg\_900.

Peak	Binding Energy (eV)		Assignment
	PCA1_300mg	PCA1_300mg_900	
C1s	285.00 59.4	285.00 75.8	C1 sp <sup>2</sup> C-C or C-H <sup>35, 46, 99</sup>
	286.02 29.1	286.30 13.6	C2 C-O / C-N / C-S <sup>35</sup>
	287.80 8.7	287.50 5.3	C3 C=O / C=N <sup>35, 101</sup>
	289.60 2.9	288.90 2.1	C4 O=C-O <sup>106</sup>
	-	290.50	C5 $\pi$ - $\pi^*$ shake up satellite <sup>18, 46</sup>
	-	3.2	
N1s	-	398.50	N1 pyridinic <sup>44, 46</sup>
	-	38.5	
	400.40 100.0	-	N2 pyrrolic <sup>44</sup>
	-	401.38	N3 quaternary <sup>35, 44</sup>
	-	38.4	
	-	403.50	N4 pyridinic N-Oxide <sup>35</sup>
-	23.1		

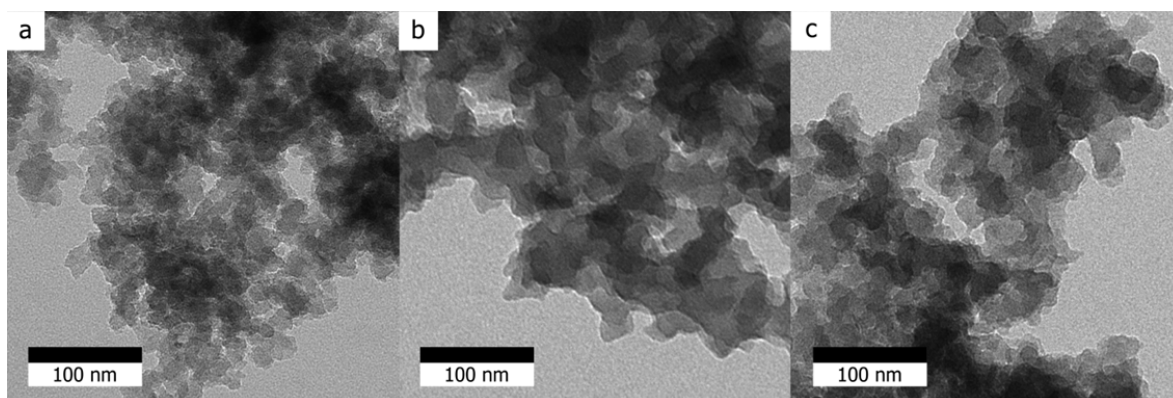


Fig. A 13 TEM images of a) PCA3\_600mg, b) S-CA and c) SN-CA

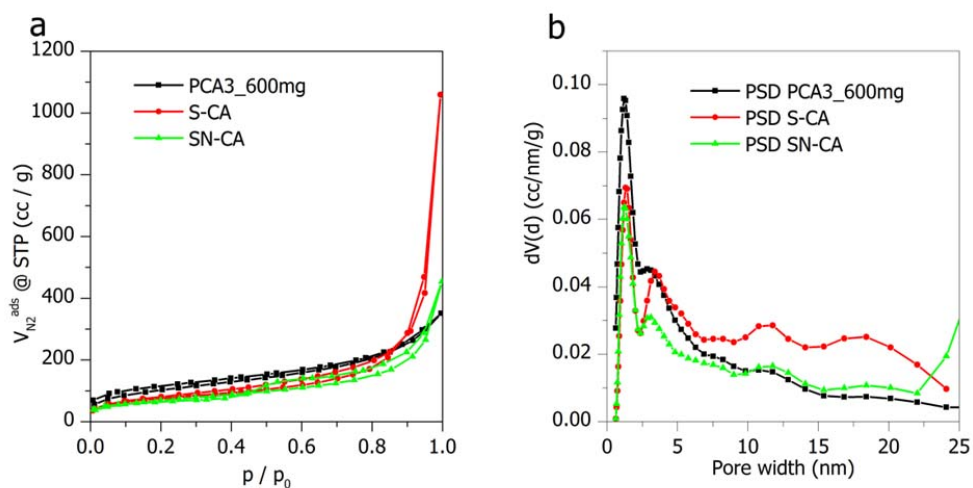


Fig. A 14 a) Nitrogen sorption isotherms and b) pore size distributions (QSDFT model) obtained for S, N and SN doped aerogels after HTC at 180 °C.

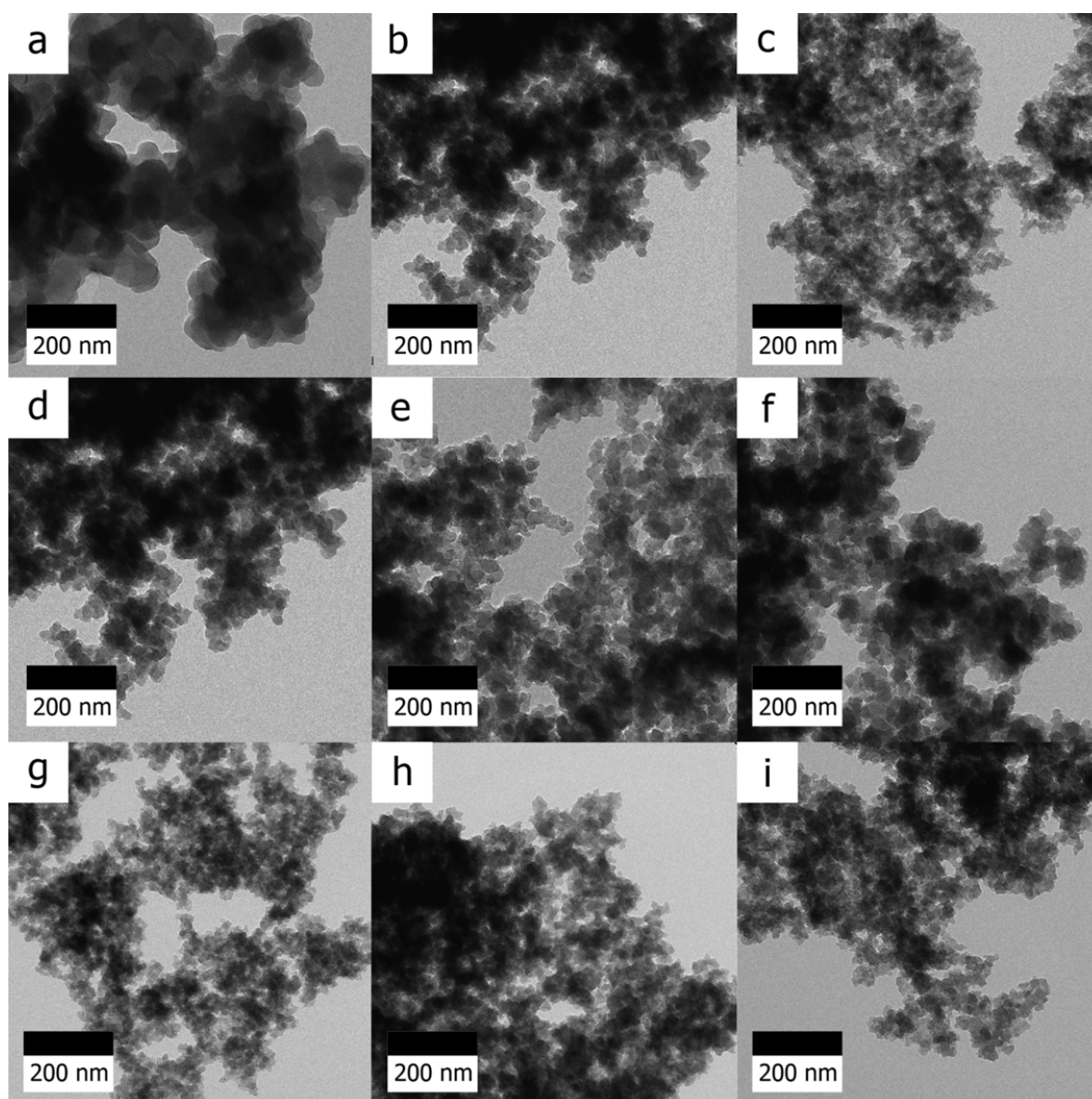


Fig. A 15 TEM images of a) PCA1\_150mg\_900, b) PCA1\_300mg\_900, c) PCA1\_600mg\_900, d) PCA1\_300mg\_900, e) PCA2\_300mg\_900, f) PCA3\_300mg\_900, g) PCA3\_600mg\_900, h) S-CA\_900 and i) SN-CA\_900

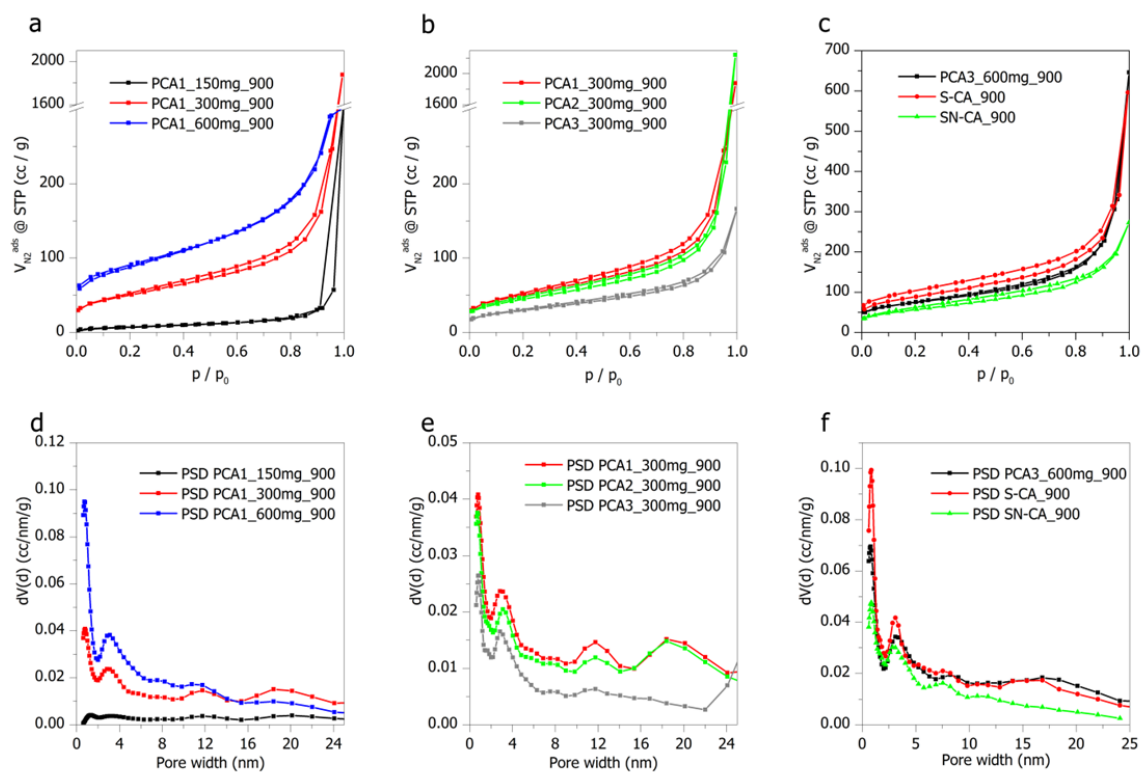


Fig. A 16  $N_2$  sorption isotherms of a) Borax series, b) PCA series and c) PCA3\_600mg\_900, S-CA and SN-CA after pyrolysis at 900 °C. The corresponding pore size distributions (QSDFT model) are shown in d), e) and f), respectively.

### 9.3 List of abbreviations

---

$^{13}\text{C}$ MAS ssNMR	$^{13}\text{C}$ Magic Angle Spinning solid state Nuclear Magnetic Resonance
BET	Brunauer-Emmett-Teller
CA	Carbon aerogel
CHS	Carbon Hollow Spheres
CV	Cyclic Voltammetry
Cys/CS	L-Cysteine
DFT	Density Functional Theory
DMT	2,5 DiMethyl-Thiophene
EAS	Electrophilic Aromatic Substitution
EDG	Electron-Donating Group
EDX	Energy Dispersive X-ray spectroscopy
EWG	Electron-Withdrawing Group
FT-IR	Fourier-Transform Infrared Spectroscopy
Glu	D-(+)-Glucose
HMF	HydroxyMethylFurfural
HRTEM	High-Resolution Transmission Electron Microscopy
HSAB	Hard and Soft Acids and Bases
HTC	HydroThermal Carbonization
<i>h</i> HTC	High temperature HydroThermal Carbonization
LBAE	Lobry de Bruyn – Alberda van Ekenstein transformation
LbL	Layer-by-layer
LSV	Linear Sweep Voltammetry
<i>l</i> HTC	Low temperature HydroThermal Carbonization
MPA	3-Mercapto-Propionic Acid
MTP	2-Methyl-ThioPhene
ORR	Oxygen Reduction Reaction
PCA	2-Pyrrol-CarboxAldehyde
PEG	PolyEthylene Glycol
PS	PolyStyrene

QSDFT	Quenched Solid Density Functional Theory
RDE	Rotating Disk Electrode
RF	Resorcinol-formaldehyde
SDBS	4-DodecylBenzeneSulfonic acid
SDS	Sodium Dodecyl Sulfate
SEM	Scanning Electron Microscopy
SHV	SuperHeated Vapor
Stc	Starch (soluble)
STEM	Scanning Transmission Electron Microscopy
TCA	2-Thienyl-CarboxAldehyde
TCAcid	2-Thiophene-Carboxylic Acid
TCys/TC	S-(2 Thienyl)-L-Cysteine
TDCA	2,5-Thiophene-DiCarboxAldehyde
TEM	Transmission Electron Microscopy
TGA	ThermoGravimetric Analysis
XPS	X-ray Photoelectron Spectroscopy
XRD	X-Ray Diffraction
Xyl	D-(+)-Xylose

## 10 References

---

1. D. E. Stokes, *Pasteur's quadrant: basic science and technological innovation.*, Brookings Institution Press., Washington, D.C., 1997.
2. K. M. Einhäupl, OECD workshop on "Basic research: Policy relevant definitions and measurement", Oslo, Norway, 2001.
3. F. Bergius, *J. Soc. Chem. Ind.*, 1913, **32**, 462-467.
4. M. M. Titirici and M. Antonietti, *Chem. Soc. Rev.*, 2010, **39**, 103-116.
5. B. Hu, K. Wang, L. Wu, S.-H. Yu, M. Antonietti and M.-M. Titirici, *Adv. Mater.*, 2010, **22**, 813-828.
6. M. M. Titirici, A. Thomas and M. Antonietti, *New J. Chem.*, 2007, **31**, 787-789.
7. S. Meyer, B. Glaser and P. Quicker, *Environmental Science & Technology*, 2011, **45**, 9473-9483.
8. B. Hu, K. Wang, L. H. Wu, S. H. Yu, M. Antonietti and M. M. Titirici, *Adv. Mater.*, 2010, **22**, 813-828.
9. A. J. Ragauskas, C. K. Williams, B. H. Davison, G. Britovsek, J. Cairney, C. A. Eckert, W. J. Frederick, J. P. Hallett, D. J. Leak, C. L. Liotta, J. R. Mielenz, R. Murphy, R. Templer and T. Tschaplinski, *Science*, 2006, **311**, 484-489.
10. G. R. Walther, E. Post, P. Convey, A. Menzel, C. Parmesan, T. J. C. Beebee, J. M. Fromentin, O. Hoegh-Guldberg and F. Bairlein, *Nature*, 2002, **416**, 389-395.
11. C. D. Keeling, T. P. Whorf, M. Wahlen and J. Vanderpligt, *Nature*, 1995, **375**, 666-670.
12. C. D. Thomas, A. Cameron, R. E. Green, M. Bakkenes, L. J. Beaumont, Y. C. Collingham, B. F. N. Erasmus, M. F. de Siqueira, A. Grainger, L. Hannah, L. Hughes, B. Huntley, A. S. van Jaarsveld, G. F. Midgley, L. Miles, M. A. Ortega-Huerta, A. T. Peterson, O. L. Phillips and S. E. Williams, *Nature*, 2004, **427**, 145-148.
13. R. K. Pachauri and A. Reisinger, *Climate Change 2007: Synthesis Report*, IPCC, Geneva, 2007.
14. M. I. Hoffert, K. Caldeira, G. Benford, D. R. Criswell, C. Green, H. Herzog, A. K. Jain, H. S. Kheshgi, K. S. Lackner, J. S. Lewis, H. D. Lightfoot, W. Manheimer, J. C. Mankins, M. E. Mauel, L. J. Perkins, M. E. Schlesinger, T. Volk and T. M. L. Wigley, *Science*, 2002, **298**, 981-987.
15. M. A. Shannon, P. W. Bohn, M. Elimelech, J. G. Georgiadis, B. J. Marinas and A. M. Mayes, *Nature*, 2008, **452**, 301-310.
16. S. P. Sohi, E. Krull, E. Lopez-Capel and R. Bol, in *Advances in Agronomy, Vol 105*, ed. D. L. Sparks, Elsevier Academic Press Inc, San Diego, 2010, vol. 105, pp. 47-82.
17. C. Petit, G. W. Peterson, J. Mahle and T. J. Bandosz, *Carbon*, 2010, **48**, 1779-1787.
18. M. Sereych, M. Khine and T. J. Bandosz, *ChemSusChem*, 2011, **4**, 139-147.
19. K. Kordas, T. Mustonen, G. Toth, H. Jantunen, M. Lajunen, C. Soldano, S. Talapatra, S. Kar, R. Vajtai and P. M. Ajayan, *Small*, 2006, **2**, 1021-1025.
20. R. Leboda, A. Lodyga and A. Gierak, *Materials Chemistry and Physics*, 1997, **51**, 216-232.
21. R. Leboda, A. Lodyga and B. Charnas, *Materials Chemistry and Physics*, 1998, **55**, 1-29.
22. T. Hanai, *Journal of Chromatography A*, 2003, **989**, 183-196.
23. Y. Zhai, Y. Dou, D. Zhao, P. F. Fulvio, R. T. Mayes and S. Dai, *Adv. Mater.*, 2011, **23**, 4828-4850.
24. D. S. Su and R. Schlögl, *ChemSusChem*, 2010, **3**, 136-168.



25. P. Serp, M. Corrias and P. Kalck, *Appl. Catal. A-Gen.*, 2003, **253**, 337-358.
26. R. Jasinski, *Nature*, 1964, **201**, 1212-&.
27. E. Guilminot, F. Fischer, M. Chatenet, A. Rigacci, S. Berthon-Fabry, P. Achard and E. Chainet, *J. Power Sources*, 2007, **166**, 104-111.
28. S.-A. Wohlgemuth, F. Vilela, M.-M. Titirici and M. Antonietti, *Green Chem.*, 2012, **14**.
29. K. P. Gong, F. Du, Z. H. Xia, M. Durstock and L. M. Dai, *Science*, 2009, **323**, 760-764.
30. M. Terrones, P. M. Ajayan, F. Banhart, X. Blase, D. L. Carroll, J. C. Charlier, R. Czerw, B. Foley, N. Grobert, R. Kamalakaran, P. Kohler-Redlich, M. Ruhle, T. Seeger and H. Terrones, *Appl. Phys. A-Mater. Sci. Process.*, 2002, **74**, 355-361.
31. A. Marchand and J. V. Zanchetta, *Carbon*, 1966, **3**, 483-491491.
32. E. T. Thostenson, Z. F. Ren and T. W. Chou, *Compos. Sci. Technol.*, 2001, **61**, 1899-1912.
33. P. Avouris, Z. H. Chen and V. Perebeinos, *Nat. Nanotechnol.*, 2007, **2**, 605-615.
34. H. J. Dai, *Surf. Sci.*, 2002, **500**, 218-241.
35. C. H. Choi, S. H. Park and S. I. Woo, *Green Chem.*, 2011, **13**, 406-412.
36. T. Tsubota, K. Takenaka, N. Murakami and T. Ohno, *J. Power Sources*, 2011, **196**, 10455-10460.
37. Y. Xia and R. Mokaya, *Advanced Materials*, 2004, **16**, 1553-1558.
38. S. Glenis, A. J. Nelson and M. M. Labes, *J. Appl. Phys.*, 1999, **86**, 4464-4466.
39. T. W. Ebbesen and P. M. Ajayan, *Nature*, 1992, **358**, 220-222.
40. P. Anastas and N. Eghbali, *Chem. Soc. Rev.*, 2010, **39**, 301-312.
41. A. Funke and F. Ziegler, *Biofuels Bioprod. Biorefining*, 2010, **4**, 160-177.
42. R. Demir-Cakan, N. Baccile, M. Antonietti and M.-M. Titirici, *Chem. Mat.*, 2009, **21**, 484-490.
43. R. Demir-Cakan, Y.-S. Hu, M. Antonietti, J. Maier and M.-M. Titirici, *Chem. Mat.*, 2008, **20**, 1227-1229.
44. R. J. White, M. Antonietti and M. M. Titirici, *J. Mater. Chem.*, 2009, **19**, 8645-8650.
45. R. J. White, N. Yoshizawa, M. Antonietti and M.-M. Titirici, *Green Chem.*, 2011, **13**, 2428-2434.
46. Z. Li, N. Baccile, S. Gross, Z. Yuanjian, W. Wei, S. Yuhan, M. Antonietti and M. M. Titirici, *Carbon*, 2010, **48**, 3778-37873787.
47. Q. Wang, H. Li, L. Chen and X. Huang, *Carbon*, 2001, **39**, 2211-2214.
48. X. M. Sun and Y. D. Li, *Angew. Chem.-Int. Edit.*, 2004, **43**, 597-601.
49. X. Cui, M. Antonietti and S.-H. Yu, *Small*, 2006, **2**, 756-759.
50. M. M. Titirici, A. Thomas, S. H. Yu, J. O. Muller and M. Antonietti, *Chem. Mat.*, 2007, **19**, 4205-4212.
51. M. M. Titirici, M. Antonietti and N. Baccile, *Green Chem.*, 2008, **10**, 1204-1212.
52. T.-P. Fellingner, Dr. rer. nat., Universität Potsdam, 2011.
53. X. Sun and Y. Li, *Angew. Chem.*, 2004, **116**, 607-611.
54. C. Falco, N. Baccile and M.-M. Titirici, *Green Chem.*, 2011, **13**, 3273-3281.
55. N. Baccile, G. Laurent, F. Babonneau, F. Fayon, M.-M. Titirici and M. Antonietti, *The Journal of Physical Chemistry C*, 2009, **113**, 9644-9654.
56. B. M. Kabyemela, T. Adschiri, R. M. Malaluan and K. Arai, *Industrial & Engineering Chemistry Research*, 1999, **38**, 2888-2895.
57. M. Möller, P. Nilges, F. Harnisch and U. Schröder, *ChemSusChem*, 2011, **4**, 566-579.
58. T. M. Aida, K. Tajima, M. Watanabe, Y. Saito, K. Kuroda, T. Nonaka, H. Hattori, R. L. Smith and K. Arai, *J. Supercrit. Fluids*, 2007, **42**, 110-119.

59. H. E. Hoydonckx, W. M. Van Rhijn, W. Van Rhijn, D. E. De Vos and P. A. Jacobs, in *Ullmann's Encyclopedia of Industrial Chemistry*, Wiley-VCH Verlag GmbH & Co. KGaA, 2000.
60. M. Choura, N. M. Belgacem and A. Gandini, *Macromolecules*, 1996, **29**, 3839-3850.
61. H. Steinhart, *Angewandte Chemie International Edition*, 2005, **44**, 7503-7504.
62. F. Ledl and E. Schleicher, *Angew. Chem.-Int. Edit.*, 1990, **29**, 565-594.
63. R. J. White, N. Yoshizawa, M. Antonietti and M.-M. Titirici, *Green Chem.*, 2011.
64. S.-A. Wohlgemuth, F. Vilela, M.-M. Titirici and M. Antonietti, *Green Chem.*, 2012.
65. N. Baccile, G. Laurent, C. Coelho, F. Babonneau, L. Zhao and M.-M. Titirici, *The Journal of Physical Chemistry C*, 2011, **115**, 8976-8982.
66. F. Ledl and E. Schleicher, *Angewandte Chemie International Edition in English*, 1990, **29**, 565-594.
67. E. Capuano and V. Fogliano, *LWT - Food Science and Technology*, 2011, **44**, 793-810.
68. J. Koch, M. Pischetsrieder, K. Polborn and T. Severin, *Carbohydrate Research*, 1998, **313**, 117-123.
69. P. Buonora, J.-C. Olsen and T. Oh, *Tetrahedron*, 2001, **57**, 6099-6138.
70. A. Schonberg and R. Moubacher, *Chem. Rev.*, 1952, **50**, 261-277.
71. F. Brody and P. R. Ruby, in *Chemistry of Heterocyclic Compounds*, John Wiley & Sons, Inc., 2008, pp. 99-589.
72. V. A. Yaylayan and C. P. Locas, *Molecular Nutrition & Food Research*, 2007, **51**, 437-444.
73. G. T. Wondrak, R. Tressl and D. Rewicki, *Journal of Agricultural and Food Chemistry*, 1997, **45**, 321-327.
74. J. Zhang, *PEM fuel cell electrocatalysts and catalyst layers: fundamentals and applications*, Springer, 2008.
75. R. Bashyam and P. Zelenay, *Nature*, 2006, **443**, 63-66.
76. A. Morozan, B. Joussetme and S. Palacin, *Energy Environ. Sci.*, 2011, **4**, 1238-1254.
77. J. Ozaki, T. Anahara, N. Kimura and A. Oya, *Carbon*, 2006, **44**, 3358-3361.
78. L. Yang, S. Jiang, Y. Zhao, L. Zhu, S. Chen, X. Wang, Q. Wu, J. Ma, Y. Ma and Z. Hu, *Angew. Chem.-Int. Edit.*, 2011, **50**, 7132-7135.
79. Z. Yang, Z. Yao, H. Nie, X. Zhou, Z. Liu and S. Huang, *Chem. Commun.*, 2011.
80. Z. Yang, Z. Yao, G. Li, G. Fang, H. Nie, Z. Liu, X. Zhou, X. a. Chen and S. Huang, *ACS Nano*, 2011.
81. K. A. Kurak and A. B. Anderson, *J. Phys. Chem. C*, 2009, **113**, 6730-6734.
82. P. H. Matter, E. Wang, M. Arias, E. J. Biddinger and U. S. Ozkan, *J. Phys. Chem. B*, 2006, **110**, 18374-18384.
83. P. H. Matter, L. Zhang and U. S. Ozkan, *Journal of Catalysis*, 2006, **239**, 83-96.
84. T. Iijima, K. Suzuki and Y. Matsuda, *Synth. Met.*, 1995, **73**, 9-20.
85. Y. P. Wu, S. B. Fang and Y. Y. Jiang, *J. Mater. Chem.*, 1998, **8**, 2223-2227.
86. Y. P. Wu, S. B. Fang and Y. Y. Jiang, *Solid State Ion.*, 1999, **120**, 117-123.
87. Y. P. Wu, S. B. Fang, Y. Y. Jiang and R. Holze, *J. Power Sources*, 2002, **108**, 245-249.
88. E. Frackowiak, *Phys. Chem. Chem. Phys.*, 2007, **9**, 1774-1785.
89. G. Lota, B. Grzyb, H. Machnikowska, J. Machnikowski and E. Frackowiak, *Chemical Physics Letters*, 2005, **404**, 53-58.
90. C. West, C. Elfakir and M. Lafosse, *Journal of Chromatography A*, 2010, **1217**, 3201-3216.
91. G. W. Muna, V. M. Swope, G. M. Swain and M. D. Porter, *Journal of Chromatography A*, 2008, **1210**, 154-159.
92. S. H. Lim, H. I. Elim, X. Y. Gao, A. T. S. Wee, W. Ji, J. Y. Lee and J. Lin, *Phys. Rev. B*, 2006, **73**.

93. D. P. Kim, C. L. Lin, T. Mihalisin, P. Heiney and M. M. Labes, *Chem. Mat.*, 1991, **3**, 686-692.
94. F. Jaouen, M. Lefevre, J. P. Dodelet and M. Cai, *J. Phys. Chem. B*, 2006, **110**, 5553-5558.
95. R. Pietrzak, H. Wachowska and P. Nowicki, *Energy Fuels*, 2006, **20**, 1275-1280.
96. S. H. Lim, H. I. Elim, X. Y. Gao, A. T. S. Wee, W. Ji, J. Y. Lee and J. Lin, *Phys. Rev. B*, 2006, **73**, 045402.
97. S. Glenis, A. J. Nelson and M. M. Labes, *J. Appl. Phys.*, 1996, **80**, 5404-5407.
98. L. Li, E. Liu, Y. Yang, H. Shen, Z. Huang and X. Xiang, *Materials Letters*, 2010, **64**, 2115-2117.
99. J. P. Paraknowitsch, A. Thomas and J. Schmidt, *Chem. Commun.*, 2011, **47**, 8283-8285.
100. T. X. Cui, R. Lv, Z. H. Huang, F. Y. Kang, K. L. Wang and D. H. Wu, *Nanoscale Res. Lett.*, 2011, **6**.
101. N. Baccile, M. Antonietti and M.-M. Titirici, *ChemSusChem*, 2010, **3**, 246-253.
102. V. K. Lamer and R. H. Dinegar, *J. Am. Chem. Soc.*, 1950, **72**, 4847-4854.
103. A. Laaksonen, V. Talanquer and D. W. Oxtoby, *Annu. Rev. Phys. Chem.*, 1995, **46**, 489-524.
104. C. Billaud, C. Maraschin, M. N. Peyrat-Maillard and J. Nicolas, in *Maillard Reaction: Chemistry at the Interface of Nutrition, Aging, and Disease*, eds. J. W. Baynes, V. M. Monnier, J. M. Ames and S. R. Thorpe, New York Acad Sciences, New York, 2005, vol. 1043, pp. 876-885.
105. C. Billaud, C. Maraschin, Y. N. Chow, S. Cheriot, M. N. Peyrat-Maillard and J. Nicolas, *Mol. Nutr. Food Res.*, 2005, **49**, 656-662.
106. M. Sevilla and A. B. Fuertes, *Chem.-Eur. J.*, 2009, **15**, 4195-4203.
107. B. J. Lindberg, K. Hamrin, G. Johansson, U. Gelius, A. Fahlman, C. Nordling and K. Siegbahn, *Phys. Scr.*, 1970, **1**, 286-298298.
108. U. Gelius, C. J. Allan, Johansso.G, H. Siegbahn, D. A. Allison and K. Siegbahn, *Phys. Scr.*, 1971, **3**, 237-&.
109. J. D. Mao, B. Xing and K. Schmidt-Rohr, *Environmental Science & Technology*, 2001, **35**, 1928-1934.
110. B. R. Sinha, F. D. Blum and D. Oconnor, *Journal of Applied Polymer Science*, 1989, **38**, 163-171.
111. G. Erbatur, O. Erbatur, M. F. Davis and G. E. Maciel, *Fuel*, 1986, **65**, 1265-1272.
112. T. Narasimhaswamy, D. K. Lee, N. Somanathan and A. Ramamoorthy, *Chem. Mat.*, 2005, **17**, 4567-4569.
113. L. Frydman, A. C. Olivieri, L. E. Diaz, A. Valasinas and B. Frydman, *J. Am. Chem. Soc.*, 1988, **110**, 5651-5661.
114. B. Nowacki, E. R. deAzevedo and L. Akcelrud, *Polymer Testing*, 2011, **30**, 342-347.
115. A. Abraham, E. Mihaliuk, B. Kumar, J. Legleiter and T. Gullion, *The Journal of Physical Chemistry C*, 2010, **114**, 18109-18114.
116. Z. Q. Li, C. J. Lu, Z. P. Xia, Y. Zhou and Z. Luo, *Carbon*, 2007, **45**, 1686-1695.
117. Y. P. Wu, S. Fang, Y. Jiang and R. Holze, *J. Power Sources*, 2002, **108**, 245-249.
118. I. Sakaguchi, M. N. Gamo, Y. Kikuchi, E. Yasu, H. Haneda, T. Suzuki and T. Ando, *Phys. Rev. B*, 1999, **60**, R2139-R2141.
119. L. Kumari and S. V. Subramanyam, *Appl. Phys. A-Mater. Sci. Process.*, 2009, **95**, 343-349.
120. Z. R. Ismagilov, A. E. Shalagina, O. Y. Podyacheva, A. V. Ischenko, L. S. Kibis, A. I. Boronin, Y. A. Chesalov, D. I. Kochubey, A. I. Romanenko, O. B. Anikeeva, T. I. Buryakov and E. N. Tkachev, *Carbon*, 2009, **47**, 1922-1929.
121. F. Caruso, *Chem.-Eur. J.*, 2000, **6**, 413-419.

122. R. J. White, K. Tauer, M. Antonietti and M. M. Titirici, *J. Am. Chem. Soc.*, 2010, **132**, 17360-17363.
123. F. Caruso, R. A. Caruso and H. Mohwald, *Science*, 1998, **282**, 1111-1114.
124. X.-y. Dai, X. Zhang, Y.-f. Meng and P.-k. Shen, *New Carbon Materials*, 2011, **26**, 389-395.
125. R. A. Caruso, A. Sussha and F. Caruso, *Chem. Mat.*, 2001, **13**, 400-409.
126. M. M. Ashton-Patton, M. M. Hall and J. E. Shelby, *Journal of Non-Crystalline Solids*, 2006, **352**, 615-619.
127. H. P. Liang, H. M. Zhang, J. S. Hu, Y. G. Guo, L. J. Wan and C. L. Bai, *Angew. Chem.-Int. Edit.*, 2004, **43**, 1540-1543.
128. M. M. Titirici, M. Antonietti and A. Thomas, *Chem. Mat.*, 2006, **18**, 3808-3812.
129. X. D. Wang, W. L. Yang, Y. Tang, Y. J. Wang, S. K. Fu and Z. Gao, *Chem. Commun.*, 2000, 2161-2162.
130. F. Caruso, R. A. Caruso and H. Mohwald, *Chem. Mat.*, 1999, **11**, 3309-3314.
131. Z. Niu, Z. Yang, Z. Hu, Y. Lu and C. C. Han, *Advanced Functional Materials*, 2003, **13**, 949-954.
132. Y. Xia, Z. Yang and R. Mokaya, *The Journal of Physical Chemistry B*, 2004, **108**, 19293-19298.
133. Q.-F. Lü, Z.-W. He, J.-Y. Zhang and Q. Lin, *Journal of Analytical and Applied Pyrolysis*, 2012, **93**, 147-152.
134. S. K. Grandhee and V. M. Monnier, *J. Biol. Chem.*, 1991, **266**, 11649-11653.
135. K. S. W. Sing, D. H. Everett, R. A. Haul, W. L. Moscou, R. A. Pierotti, J. Rouquérol and T. Siemieniewska, 1985, **57**, 603.
136. P. I. Ravikovitch and A. V. Neimark, *Langmuir*, 2002, **18**, 9830-9837.
137. M. Thommes, B. Smarsly, M. Groenewolt, P. I. Ravikovitch and A. V. Neimark, *Langmuir*, 2006, **22**, 756-764.
138. Z. Yang, D. Li, J. Rong, W. Yan and Z. Niu, *Macromolecular Materials and Engineering*, 2002, **287**, 627-633.
139. D. R. Rolison, *Science*, 2003, **299**, 1698-1701.
140. A. C. Pierre and G. M. Pajonk, *Chem. Rev.*, 2002, **102**, 4243-4266.
141. J. Biener, M. Stadermann, M. Suss, M. A. Worsley, M. M. Biener, K. A. Rose and T. F. Baumann, *Energy Environ. Sci.*, 2011, **4**.
142. G. M. Pajonk, *Applied Catalysis*, 1991, **72**, 217-266.
143. J. Fricke and T. Tillotson, *Thin Solid Films*, 1997, **297**, 212-223.
144. S. S. Kistler, *Nature*, 1931, **127**, 741-741.
145. R. W. Pekala, *J. Mater. Sci.*, 1989, **24**, 3221-3227.
146. J. L. Mohanan, I. U. Arachchige and S. L. Brock, *Science*, 2005, **307**, 397-400.
147. D. H. Long, J. Zhang, J. H. Yang, Z. J. Hu, G. Cheng, X. M. Liu, R. Zhang, L. Zhan, W. M. Qiao and L. C. Ling, *Carbon*, 2008, **46**, 1259-1262.
148. G. C. Ruben and R. W. Pekala, *Journal of Non-Crystalline Solids*, 1995, **186**, 219-231.
149. T.-P. Fellingner, R. J. White, M. M. Titirici and M. Antonietti, *Advanced Functional Materials*, 2012.
150. B. Hu, S. H. Yu, K. Wang, L. Liu and X. W. Xu, *Dalton Trans.*, 2008, 5414-5423.
151. J. C. Slater, *J. Chem. Phys.*, 1964, **41**, 3199-&.
152. S.-A. Wohlgemuth, F. Vilela, M.-M. Titirici and M. Antonietti, *Green Chem.*, DOI: 10.1039/C2GC16415A.
153. R. Z. Jiang and F. C. Anson, *J. Electroanal. Chem.*, 1991, **305**, 171-184.
154. T.-P. Fellingner, F. Hasché, P. Strasser and M. Antonietti, *J. Am. Chem. Soc.*, 2012, **134**, 4072-4075.

155. W. S. Baker, J. W. Long, R. M. Stroud and D. R. Rolison, *Journal of Non-Crystalline Solids*, 2004, **350**, 80-87.
156. Y. Y. Shao, J. H. Sui, G. P. Yin and Y. Z. Gao, *Appl. Catal. B-Environ.*, 2008, **79**, 89-99.
157. H. Jin, H. Zhang, H. Zhong and J. Zhang, *Energy Environ. Sci.*, 2011, **4**, 3389-3394.
158. Q. H. Yang, W. H. Xu, A. Tomita and T. Kyotani, *Chem. Mat.*, 2005, **17**, 2940-2945.
159. Z. Luo, S. Lim, Z. Tian, J. Shang, L. Lai, B. MacDonald, C. Fu, Z. Shen, T. Yu and J. Lin, *J. Mater. Chem.*, 2011, **21**, 8038-8044.
160. R. L. Liu, D. Q. Wu, X. L. Feng and K. Mullen, *Angew. Chem.-Int. Edit.*, 2010, **49**, 2565-2569.
161. V. V. Strelko, V. S. Kuts and P. A. Thrower, *Carbon*, 2000, **38**, 1499-1503.
162. R. A. Sidik, A. B. Anderson, N. P. Subramanian, S. P. Kumaraguru and B. N. Popov, *J. Phys. Chem. B*, 2006, **110**, 1787-1793.
163. E. Chamorro, A. Toro-Labbe and P. Fuentealba, *J. Phys. Chem. A*, 2002, **106**, 3891-3898.
164. S. Scheiner and L. D. Bigham, *J. Chem. Phys.*, 1985, **82**, 3316-3321.
165. P. R. Tremaine, in *Proceedings of the 13th International Conference on the Properties of Water and Steam*, ed. N. R. Council, 2000, ch. 954.
166. T. Stahlberg, S. Rodriguez-Rodriguez, P. Fristrup and A. Riisager, *Chem.-Eur. J.*, 2011, **17**, 1456-1464.
167. C. Vix-Guterl, E. Frackowiak, K. Jurewicz, M. Friebe, J. Parmentier and F. Beguin, *Carbon*, 2005, **43**, 1293-1302.
168. T. Fujino, J. M. Calderon-Moreno, S. Swamy, T. Hirose and M. Yoshimura, *Solid State Ion.*, 2002, **151**, 197-203.
169. J. M. Calderon Moreno and M. Yoshimura, *J. Am. Chem. Soc.*, 2001, **123**, 741-742.
170. Y. G. Gogotsi and M. Yoshimura, *Nature*, 1994, **367**, 628-630.
171. A. Kruse and E. Dinjus, *The Journal of Supercritical Fluids*, 2007, **39**, 362-380.
172. D. Broll, C. Kaul, A. Kramer, P. Krammer, T. Richter, M. Jung, H. Vogel and P. Zehner, *Angew. Chem.-Int. Edit.*, 1999, **38**, 2999-3014.
173. F. Salvador, M. J. Sánchez-Montero and C. Izquierdo, *The Journal of Physical Chemistry C*, 2007, **111**, 14011-14020.
174. E. Dinjus and A. Kruse, *J. Phys.-Condes. Matter*, 2004, **16**, S1161-S1169.
175. C. Falco, F. Perez Caballero, F. Babonneau, C. Gervais, G. Laurent, M.-M. Titirici and N. Baccile, *Langmuir*, 2011, **27**, 14460-14471.
176. C. Falco, N. Baccile and M.-M. Titirici, *Green Chem.*, 2011.
177. L. A. Dombrovsky, J. H. Randrianalisoa and D. Baillis, *Int. J. Heat Mass Transf.*, 2007, **50**, 1516-1527.
178. L. A. Dombrovsky, *High Temp.*, 2005, **43**, 247-258.
179. E. M. Sparrow and N. Cur, *Trans. ASME, C, J. Heat Transf.*, 1976, **98**, 232-239239.
180. Y. Wang, D. C. Alsmeyer and R. L. McCreery, *Chem. Mat.*, 1990, **2**, 557-563.